High Pressure Hugoniot Measurements in Solids Using Mach Reflections

Thesis by

Justin Lee Brown

In Partial Fulfillment of the Requirements

for the Degree of

Doctor of Philosophy

California Institute of Technology

Pasadena, California

2011

(Defended May 18, 2011)

Acknowledgments

I would first like to acknowledge my family for the ridiculous amount of support and encouragement they have always provided. To my mom, dad, and sister I give a heartfelt thank you. Mom and dad, thanks for making me bus tables and roll burritos when by all rights I should have been playing video games like the rest of my friends, and, Elise, thanks for always conspiring with me in our ill-conceived plans for revenge. As it were, I'm not sure I could have received much better motivation for staying in school. Nearly ten years removed from high school and I'm still afraid of the real world, so, well done. I would like to thank all of my grandparents, aunts, uncles, cousins, and the rest of my family of whom there are too many to name for all of your support and for ensuring there is never a dull moment. Additionally, to Vianca, thank you for your unyielding support.

A special thanks to my advisor, Professor Guruswami Ravichandran, for your encouragement and guidance these last four years. You are truly fearless in your willingness to attempt new and seemingly crazy things, and I cannot tell you how much I appreciate the opportunity you gave me to work on this project. It has felt like more fun than work (and not just because I got to blow stuff up), and having you as an advisor has made my time at Caltech a truly great experience. I would also like to acknowledge the rest of my committee, Professors Kaushik Bhattacharya, Chiara Daraio, Hans Hornung, and Dan Meiron. Professor Bhattacharya, whether you know it or not, you constantly inspire me to improve my understanding of mechanics. Professor Hornung, I have enjoyed our discussions on shock reflections, and I hate to think where this work may have ended up without your suggestions on viewing the problem from a gas dynamics perspective. I would also like to acknowledge Dr. Dennis Grady for your helpful discussions and suggestion to examine a composite cylinder approach to generate converging shocks.

A huge thanks to all of the people at the Sandia National Laboratories who helped me find my way as an intern. First and foremost, I would like to thank Bill Reinhart and Lalit Chhabildas for first giving me the opportunity to work at Sandia. This was an eye-opening experience and was the first time I felt truly excited and inspired to learn about something new. I would also like to thank Tracy Vogler for your additional advice and mentoring. Between you three, you always came up with exciting and impactful projects for me to work on, which I realize now was no easy task given my lack of practical experience at the time. I would also like to thank Tom Thornhill, John

Martinez, Dan Dow, and Heidi Anderson for keeping things light and teaching me the finer details of experimental work. I still don't know how you made things look so easy. I have little doubt that without the experience and support you all provided, I would not be in the position I am today. A second thanks goes to Bill for allowing me to come back to the STAR facility after spending a few years at Caltech and perform some of the experiments which play a key role in this thesis. I would like to thank Scott Alexander and Jim Asay for your words of wisdom and technical advice, Wayne Trott for taking the time to teach me the ORVIS diagnostic, and Daniel Dolan for your suggestions and ideas on further instrumentation.

I would like to thank all of my friends and colleagues at Caltech who made my time here so much more enjoyable. To everyone in Ravi's and Kaushik's group, thank you for broadening my horizons. In particular, I would like to thank Andy Richards for all of the discussions we have had over the years, both technical and not. One of these days, I'll come up with a question you can't answer. To Mike Mello, your unparalleled enthusiasm for all things is infectious; thank you for not only our discussions on interferometry but also for inspiring pure awesomeness. A special thanks to Petros Arakelian for all of your technical support which kept the lab up and running, as well as to Linda Miranda and Cheryl Gause for all of their administrative support. Thanks to Joe, Ali, and Brad in the GALCIT machine shop for making all of the parts which I would later destroy. To the original hipsters, Jacob and Chris, thanks for making Ravi's group great and, particularly, for getting me out of the lab and onto my snowboard. To Mumu, Jon, Nick B., Nick P., Vicki, Scott, Jason, Joe, Andrea, Dan, Pablo, and everyone else I have had the pleasure of getting to know, thank you for the memories and I wish you the best in your future endeavors.

Finally, I gratefully acknowledge the research support provided by the Caltech Center for the Predictive Modeling and Simulation of High-Energy Density Dynamic Response of Materials through the U.S. Department of Energy contract DE-FC52-08NA28613 and Professor Michael Ortiz for giving me the chance to work under the PSAAP project.

Abstract

Shock compression experiments provide access to extreme pressures in a laboratory setting. Matter at these pressures is often studied by utilizing a well controlled planar impact between two flat plates to generate a one dimensional shock wave. While these experiments are a powerful tool in equation of state (EOS) development, they are inherently limited by the velocity of the impacting plate. In an effort to dramatically increase the range of pressures that can be studied with available impact velocities, a new experimental technique is examined. The target plate is replaced by a composite assembly consisting of two concentric cylinders and is designed such that the initial shock velocity in a well characterized outer cylinder is higher than in the inner cylinder material of interest. After impact, conically converging shocks are generated at the interface due to the impedance mismatch between the two materials and the axisymmetric geometry. Upon convergence, an irregular reflection occurs and the conical analog of a Mach reflection develops. The Mach reflection grows until it reaches a steady state, for which an extremely high-pressure state is concentrated behind the Mach stem.

The Mach lens composite target comprising of the concentric cylinders is studied using a combination of analytical, numerical, and experimental techniques. A simple analytical method for calculating the form of the Mach reflection is determined through classic concepts in gas dynamics. Traditionally, oblique shock reflection phenomena in gases can be treated through a shock polar analysis, which provides an intuitive graphical method for solving such problems. By translating the classic Lagrangian treatment of a 1-D plane shock wave in a solid to the Eulerian oblique shock framework for gases, a similar methodology is developed to treat shock reflections in solids. Numerical simulations using a hydrocode are also conducted to gain further insight into the problem. These simulations reveal quantitative details about the shock propagation and interaction in the Mach lens and are used to both validate the shock polar analysis and design the experiments.

The Mach lens concept is validated experimentally by examining a copper inner cylinder in conjunction with outer materials of either 6061-T6 aluminum or molybdenum. Since, in the steady state, the axial velocity of the Mach reflection is equal to the far field shock velocity in the outer cylinder, the shock velocity can be calculated through impedance matching between the well characterized impactor and outer cylinder materials from a measurement of the projectile velocity. A

second measurement of the Mach reflection is made through velocity interferometry at the rear surface of the target using either VISAR, which provides a point measurement of the velocity, or ORVIS, which provides the velocity spatially resolved along a line. The VISAR experiments provide a time resolved free surface velocity measurement at the center of the target which allows for an inference of the in situ particle velocity, and, in conjunction with the calculated shock velocity, provides the necessary information to calculate the shocked state behind the Mach stem. Measurements of this shocked state have been found to be in excellent agreement with Hugoniot measurements in copper using traditional plane shock techniques. These Hugoniot states illustrate multiplications in the pressure between 1.7 and 4.4 over the equivalent plate impact experiments. These types of high pressures traditionally require impact velocities between 2 and 5 km/s, which can only be obtained with two-stage launcher technology. The spatial properties of the Mach reflection are investigated using either multiple VISAR point measurements or the ORVIS diagnostic. The measurements are found to be in good agreement with both the shock polar analysis, and numerical simulations. The possibilities of using this type of full field information to extract an entire Hugoniot curve in a single experiment are also discussed. The effects of phase transitions on the Mach lens target are also examined through the use of an iron inner cylinder. Iron undergoes a well known α (bcc) - ϵ (hcp) polymorphic transition along the Hugoniot, and the effects of this response are examined through the use of numerical simulations and VISAR measurements.

Contents

List of Figures

List of Tables

Chapter 1

Introduction

1.1 Background

At the most fundamental level, the philosophy in experimental solid mechanics is rather simple: apply a load to the material and measure a response of deformation and/or force. In studying the dynamic behavior of materials, the experimentalist may choose, for example, an impactor to apply the load on a long slender bar or plate. In the case of low velocity impact, the stress induced in the solid is below the material's yield strength and the behavior is governed by elastic wave propagation. For a wide range of materials, particularly metals, the elastic response is linear and Hooke's law may be applied to model the response of the system. When the impact is at high velocities, the material can be driven to the point of plastic deformation and the description of the response becomes much more difficult. This regime involves the propagation of elastic-plastic waves, and nonlinearities can arise from both the material response and geometric considerations of finite deformations [31]. On the most extreme end of this example, impact at very high velocities can result in extreme pressures that can exceed the strength of the material by an order of magnitude or more, particularly if the target is in a state of uni-axial strain. Under these conditions, the solid behaves in a fluid-like manner and a hydrodynamic description of the response is appropriate. These three regimes exemplify the important aspects of the physics in various dynamic impact experiments and related applications [65]. Typically, the rate of loading is quantified by strain rate. Low strain rates, on the order of $10/s$, result in elastic wave propagation so acoustics is the primary consideration. Intermediate strain rates, between 10^2 and $10^4/s$, generally explore elastic-plastic wave propagation where the rate-dependent constitutive response of the material can be characterized. Extreme strain rates, above $10^5/s$, result in highly nonlinear wave propagation and are the primary focus of this thesis.

The nonlinear response of matter when subjected to high pressures plays a key role in the description of wave propagation in this regime. In general, the wave speed of a gas, fluid, or solid increases monotonically with pressure. As a result, the highest pressure portion of the wave will propagate the fastest and the wave will steepen into a shock. This makes the study of shock waves

vital to a complete description of wave propagation, evidenced by the fact that this has been an active area of research for well over a century. Early work focused on shock propagation in gases since the high temperatures and pressures associated with shock waves provide suitable conditions for application of the ideal gas law. The use of this equation of state allows for the study of more complex shock phenomena such as shock wave interaction, reflection, and non-equilibrium thermodynamics.

Of course, there is nothing that limits the propagation of shocks to gases, and an interest in the shock compression of condensed matter developed during the 1940s. During this time, the technology was developed to explosively load materials in a well controlled and repeatable experiment. Observations in these experiments led a group of scientists to shift their fundamental view of shock waves. In 1958, Melvin Rice, John Walsh, and Robert McQueen published their groundbreaking work on the subject [72]. In this article, the shock wave is viewed as a tool to study matter in an entirely new regime of pressures. They realized that the propagation of simple plane shock waves could be used to infer information about the behavior of the material. Typically, a shock front is on the order of a few tenths of a millimeter in thickness while the velocity of the wave is on the order of a few km/s [72]. This means equilibrium over the shock front is typically achieved within 10^{-7} s. As a result, two thermodynamic properties of the shocked state can be measured, and the use of mass, momentum, and energy conservation laws allow for the complete characterization the shocked state. Thus, these experiments provide the means to access the state of matter at extreme pressures.

A visualization of the value of using shock waves as an avenue for the experimental testing of materials is given in Figure 1.1. This illustration shows a phase diagram for a typical material and considers the various experiments that are currently used to examine high pressure behavior. Quasistatic compression experiments, using a diamond anvil cell, are generally limited to pressures on the order of 300 GPa and relatively low temperatures. Additionally, rate effects cannot be examined so these experiments are generally ill-suited to characterize dynamic behavior. On the other end of the temperature spectrum, the high energy-density states associated with plasmas can be generated using lasers. As shown, there are only two experimental paths that cut through the phase space between these regimes, both of which utilize nonlinear wave propagation. The first method is to introduce a high amplitude ramp wave through techniques such as the impact of a graded density flyer [26] or magnetic loading [44]. The properties of these nonlinear waves are measured before they steepen into a shock and, hence, the measured material response is assumed to lie along the material's isentrope. The second method utilizes shock waves, which are fundamentally easier to generate and are generally produced using mechanical impact or explosives [38]. The entropy generated in a shock results in much high temperatures in the shocked states. A locus of shocked states for a given material is referred to as the Hugoniot curve and, as shown in Figure 1.1, can be used to provide valuable thermodynamic information at high temperatures and pressures.

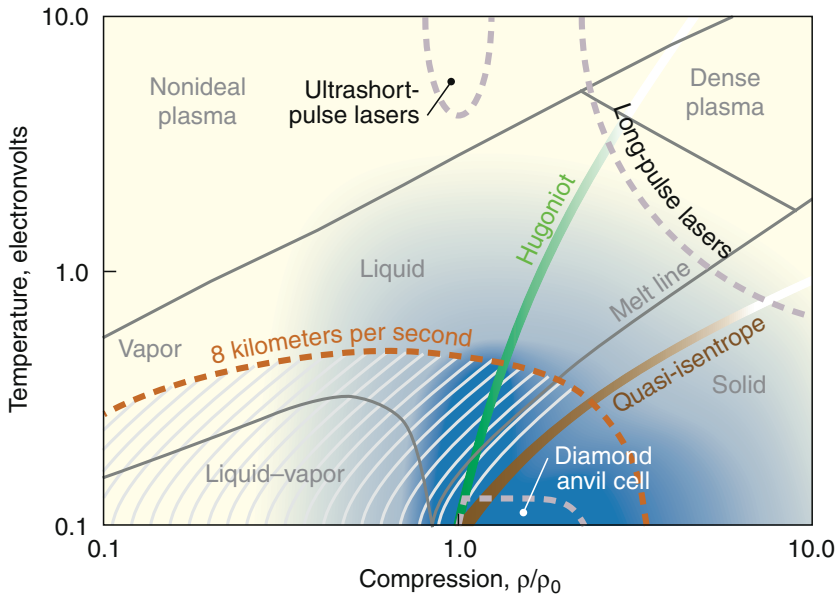

Figure 1.1: Current experimental techniques used to probe the high pressure response of materials, taken from [70]. Pressures between compression by diamond anvil cell and laser driven plasmas can be accessed by nonlinear wave propagation. Shock compression results in the Hugoniot while ramp compression loads along the isentrope.

1.2 Motivation

Most scientific endeavors involve experimentally observing a physical phenomenon, developing a theory to describe the observations, and applying the theory to gain further insights or solve a practical problem. The phenomena of interest here are dynamic events such as high velocity impacts and material interactions with explosives. These types of events inherently lend themselves to military applications [65], so it is not a coincidence that significant developments in the field of shock compression were made during the height of World War II. In fact, shock compression research today still has strong ties to these same applications. A few of the primary examples include ballistic impact, shaped charges, and, ultimately, nuclear weapons. Ballistic impact, for example, may involve the design of an armor or, on the other side of the problem, an armor defeating projectile. Shaped charges are another area of interest. Upon detonation, an explosive in contact with a hollow metal cone deforms the cone into a rod that is accelerated to velocities of up to 10 km/s, which provides tremendous penetration capabilities. Of particular importance is the detonation of nuclear weapons. The implosion triggering system requires a deep understanding of shock wave physics to precisely control and direct the compression of the core. Similar understanding is at the core of achieving ignition in inertial confinement fusion.

While shock compression has its roots in weapons development, many important civilian applications have also been developed [65]. One example is the shock synthesis and consolidation of

materials. The application of a shock wave to carbon (graphite) has been shown to synthesize diamond powder. Similarly, passing a shock through a fine metal powder can cause melting and bonding between the particles, consolidating the powder and producing materials with unique mechanical properties. A second example is characterizing the shielding on space structures for micrometeorite impacts. Micrometeorites often travel at velocities well in excess of material wave speeds, on the order of 10-20 km/s. Such collisions are referred to as hypervelocity impacts and can result in complex physical processes such as melting, vaporization, and fragmentation. High pressure shock waves can provide access to these extreme processes and aid in the development of material models.

1.3 Outline

The structure of the thesis is as follows. A modern theory of the description of shock propagation in both gases and solids is presented in Chapter 2. As with most problems in fluid mechanics, an Eulerian description of the flow provides a useful framework in which to work. The focus in this section is on how oblique shock equations are used to solve shock reflection problems. Particular emphasis is placed on the well established method of using shock polars to solve such problems. Next, the theory moves to the analysis of wave propagation in solids. The classic theory of shock behavior in solids is restricted to 1-D plane shock waves and a Lagrangian description of the motion. Generally, oblique shocks are not considered for material characterization because the analysis is complicated. As seen in gas dynamics, however, the nonlinear nature of interacting shocks can produce extremely high pressures. Similarly, converging shock waves can be used to create high pressure states in solids. This motivates the study of an experimental design that can be used to extend classic shock compression loading techniques to higher pressures through the use of converging shocks. The design presented in this dissertation is the so-called Mach lens and is an extension of a similar explosive configuration [41]. The Mach lens, illustrated in 2.18, consists of two concentric cylinders such that the axial direction of the lens corresponds to the direction of shock loading. The materials for the cylinders are chosen such that, on loading, the shock speed of the outer cylinder is higher than that of the inner cylinder. The ensuing impedance mismatch results in reflected converging waves at the interface. Upon convergence on the axis of the target, the axisymmetric nature of the assembly results in an irregular wave reflection in the form of a Mach wave. This Mach reflection results in a nearly planar high pressure state at the center of the target for which Hugoniot measurements can be made. A simple solution for the configuration of the Mach reflection is found by examining a connection between the classic Lagrangian and Eulerian descriptions of shock motion in solids and gases, respectively. The extension of the well known shock polar techniques developed in gas dynamics to the equation of state for solids [64] results in an analogous framework to describe oblique shock waves in solids.

Chapter 3 describes the experimental methods used to validate the Mach lens technique and make high pressure Hugoniot measurements. Powder gun systems are used to explosively launch projectiles to velocities of up to 2 km/s . The projectile impacts the Mach lens target and several diagnostics are used to monitor the response of the resulting shock waves. Electric shorting pins on the impact surface provide a time of impact and can be used to estimate any tilt between the impactor and target. Velocity interferometry (VISAR) is the primary means of quantifying the Mach reflection and provides a measurement of the time resolved rear free surface velocity at a point. The setup of a second interferometer system (ORVIS), which provides free surface velocity along a line, is also described. The chapter concludes with a description of the materials chosen for use in the experiments along with the increase in pressure expected over traditional shock experiments. Copper and iron targets were chosen as the inner materials to validate the technique. Copper serves as an ideal material, while iron contains the complication of a polymorphic phase transition. Outer materials of either aluminum or molybdenum were chosen to study the effect of the confining material. With the aluminum confinement, a magnification in pressure of over 4 times can be achieved.

Chapter 4 contains the numerical simulations used to gain further insight into the problem. The simulations are performed with the CTH hydrocode and confirm the expected behavior of the wave propagation in the Mach lens target. A representative simulation is presented which provides further details on both the qualitative and quantitative response of the system. More specific examples are also presented which illustrate the subtle details of the effect of the Mach reflection structure in copper when using either the aluminum or molybdenum confinement. The simulations are compared to the shock polar solutions, where the behavior of the differing outer materials is captured well. The use of an iron target greatly complicates the response of the system because the Mach reflection shocks through the phase transition. Simulations detailing the behavior of the reflection under these conditions are also presented.

Chapter 5 contains the experimental results and discussion that validates the Mach lens technique. The results on the copper target are examined first. Two experiments utilizing VISAR measurements at several points along the rear free surface are presented which illustrate the behavior of the Mach reflection. The rest of the experiments contain a single VISAR measurement and the waveforms that are obtained are shown to be consistent and repeatable. A simple analysis is presented through which the impact conditions along with the VISAR measurement can be used to calculate the high pressure Hugoniot state obtained at the center of the target. These measurements are shown to be in good agreement with data obtained in classic planar shock experiments. Further experiments on copper using the ORVIS diagnostic are also presented. These experiments were unable to maintain contrast in the interferometer after shock arrival and as a result only the structure of the Mach reflection is captured. The original intent of the experiments was to capture

both the structure of the wave and also the free surface particle velocity. With this information, it is possible to make multiple Hugoniot measurements in a single experiment. To demonstrate the idea, the analysis is applied to a synthetic numerically simulated data set that idealizes what would be obtained using ORVIS. The chapter is concluded with the results for the iron experiments. These experiments are monitored with single-point VISAR from which the properties of the phase transition can be measured.

Chapter 6 summarizes the key points in this thesis and presents several ideas for possible future work. The original contributions presented are the numerical simulations of the Mach lens target, application of the shock polar method to solve for the Mach wave configuration, and the use of classic interferometric techniques to measure the shocked states associated with the reflection. The primary advantages of the Mach lens technique over traditional 1-D shock experiments is the ability to measure not only much higher shock pressures but also multiple Hugoniot states. Since the technique is not specific to how the load is generated, it is not difficult to translate the Mach lens target to other shock loading systems. An example Mach lens configuration for use with a two-stage gun projectile velocity (6 km/s) is presented. Selecting beryllium as an outer material for use with a copper inner material suggests a feasible two-stage gun experiment results in pressures of over 650 GPa. Current experimental capabilities limit Hugoniot measurements to under 350 GPa. Thus, it is possible to greatly extend the pressures that can be accessed in most of the experimental systems which generate shock loading. An equally valuable use of the configuration would be the measurement of an entire Hugoniot curve in a single experiment. As such, suggestions are made to improve the ORVIS implementation in these experiments, which may allow the interferometer to maintain contrast after the arrival of the wave. As an example, a numerical simulation is presented in which the Hugoniot for copper between 10 and 60 GPa can be estimated with a single experiment. For comparison, there are over 70 Hugoniot data points in the literature from plane shock experiments over this range. As a final consideration for future work, the feasibility of generating combined pressure-shear waves using oblique shock wave interactions is examined. A possible experimental configuration is presented and a numerical simulation is conducted to illustrate the concept.

Chapter 2

Shock Waves

This chapter presents the background and concepts in shock waves that are needed to understand the shock focusing and high pressure Mach reflections which are the subject of this dissertation. The first section relates the classic shock wave theories developed in gas dynamics for a perfect gas. An emphasis is placed on the concepts involved with the development of the oblique shock equations and the use of these equations in the solution of shock reflection problems, including Mach reflections. The second section begins with a solid mechanics perspective on the propagation of plane shock waves in a solid medium, and a general treatment of the Mie-Grüneisen equation of state. This equation of state is applied, using ideas from gas dynamics, to the treatment of 2-D supersonic flow in solids. This framework is then used to construct the solution of oblique shock reflection problems in a solid. At this point, the Mach lens configuration will be introduced which utilizes converging shock waves and the subsequent Mach reflection to create a useful high pressure region for which Hugoniot information can be extracted. The chapter concludes with a brief discussion on the effect of phase transitions on this configuration.

2.1 Gas Dynamics

In the most simple of terms, gas dynamics is the study of compressible fluid mechanics. Of primary concern here is the propagation of finite amplitude waves within the fluid medium, where for most normal fluids the nonlinear nature of the wave speed will result in a propagating discontinuity or shock. Ernst Mach, for whom many of the phenomena in gas dynamics are named, was the first to note that the nonlinear nature of shock waves in air can result in irregular reflections. In 1943, Von Neumann quantified the effect by examining the reflection of an incident plane shock wave off of an inclined planar surface [82]. He notes that the purpose of the resulting reflected shock in this type of configuration is to turn the flow behind the incident shock such that it is parallel to the wedge. However, he also observes that the reflected shock has a maximum turning angle, which he defines as the extreme condition, and introduces the notion of a triple shock solution, later termed a Mach

reflection.

A comprehensive review of the theory of shock wave interaction in gases was first given by Bleakney and Taub [19] , and a modern theory, focused on more intuitive graphical methods, can be found in Hornung's review of the material [50]. The results of the latter review will be briefly summarized in the following sections in an effort to present a classical framework for shock reflection theory, which will later be used to solve reflection problems in solids.

2.1.1 Perfect Gas Equation of State

A perfect gas is the simplest idealization of a compressible fluid in thermodynamics and will be used to provide detailed analytic solutions in shock reflection problems. To begin, it will be useful to define a few quantities often used in gas dynamics:

$$\begin{aligned}
&\textit{specific heat at constant volume} && c_V = T\left(\frac{\partial S}{\partial T}\right)_V = \left(\frac{\partial E}{\partial T}\right)_V \\
&\textit{specific heat at constant pressure} && c_P = T\left(\frac{\partial S}{\partial T}\right)_P = \left(\frac{\partial H}{\partial T}\right)_P \\
&\textit{ratio of specific heats} && \gamma = \frac{c_P}{c_V} \\
&\textit{gas constant} && R = c_P - c_V \\
&\textit{sound speed} && c = \sqrt{\left(\frac{\partial P}{\partial \rho}\right)_S},
\end{aligned}$$

where T is the absolute temperature, S is the entropy, E is the internal energy, V is the specific volume, P is the pressure, and H is the enthalpy. Measurements of the thermal properties of gases show that for low densities the thermal equation of state of all gases approaches the form

$$PV = RT, \tag{2.1}$$

where R is a characteristic constant for a particular gas. For the region over which Eqn. 2.1 is valid, the gas is said to be *ideal.* A further approximation can be made to an ideal gas by assuming the specific heats, c_V and c_P , are constant, in which case the fluid is a so-called *perfect gas.* Beginning

with fundamental thermodynamics, changes in the energy, E , and enthalpy, H , may be written as

$$dE = TdS - PdV, \tag{2.2}$$

$$dH = TdS + VdP. \tag{2.3}$$

Solving for dS , substituting for the specific heats and ideal gas law, and integrating gives

$$S - S_0 = c_V ln\frac{T}{T_0} + Rln\frac{V}{V_0}, \tag{2.4}$$

$$S - S_0 = c_P ln\frac{T}{T_0} - Rln\frac{P}{P_0}. \tag{2.5}$$

Rearranging Eqns. 2.4 and 2.5 with the caloric forms of the equation of state, $H = c_P T$ and $E = c_v T$, gives the canonical forms of the perfect gas equation of state [59]

$$H\left(S, P\right) = k_1 c_P e^{\frac{S}{c_P}} P^{\frac{R}{c_P}}, \tag{2.6}$$

$$E\left(S, V\right) = k_2 c_V e^{\frac{S}{c_V}} V^{-\frac{R}{c_V}}, \tag{2.7}$$

where k_1 and k_2 are constants. Further, for isentropic processes, $dS = 0$, hence Eqns. 2.4 and 2.5 reduce to

$$ln\frac{T}{T_0} = -\frac{R}{c_V} ln\frac{V}{V_0} = \frac{R}{c_P} ln\frac{P}{P_0}, \tag{2.8}$$

which can be rewritten as a useful form for perfect gas isentropes

$$\frac{P}{P_0} = \left(\frac{\rho}{\rho_0}\right)^{\gamma} = \left(\frac{T}{T_0}\right)^{\frac{\gamma}{\gamma-1}}. \tag{2.9}$$

Differentiating this expression for the isentrope gives the sound speed of a perfect gas, c , as

$$c = \sqrt{\gamma RT}. \tag{2.10}$$

A propagating ramp wave of finite amplitude in thermodynamic equilibrium will contain states lying on the isentrope defined by Eqn. 2.9 . Since the temperature is proportional to the magnitude (pressure) of the wave, Eqn. 2.10 immediately shows that the highest pressure portion of the wave will be propagating the fastest. As such, the peak will eventually overdrive the rest of the wave and the wave will steepen into a shock wave. Of course, this is a very simplistic view of the

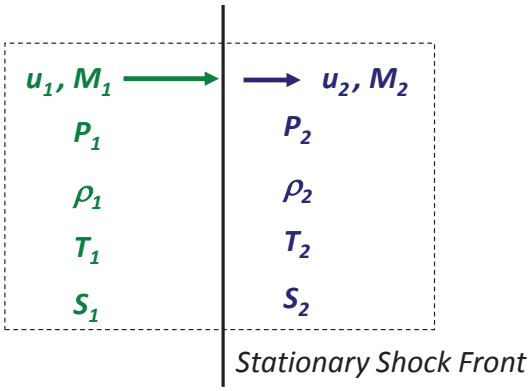

Figure 2.1: Passage of fluid through a normal shock wave.

phenomenon and is generally treated in detail by considering one dimensional wave motion [59], where the governing equations form a partial differential equation known as the wave equation. The solution of the wave equation shows that the initial disturbance propagates along characteristic lines dependent on the wave speed, and the breakdown of the solution occurs at the unique point where equation's characteristics intersect in space and time. An admissible solution after this breakdown takes the form of a shock wave. This type of solution is typical of any nonlinear wave propagation problem, and is presented in more detail for wave propagation in a solid in Section 2.2.

2.1.2 Normal Shock Jump Equations

The problem of a propagating steady normal shock wave is generally examined in the Eulerian reference frame such that the shock appears stationary, as shown in Fig. 2.1. This results in a known upstream state with an initial velocity normal to the shock wave, u_1, density, ρ_1, and temperature, T_1. The downstream state (2) can be determined by examining a control volume around the shock wave, resulting in the following conservation equations of mass, momentum, and energy[33], respectively,

$$\rho_1 u_1 = \rho_2 u_2, \tag{2.11}$$

$$P_1 + \rho_1 u_1^2 = P_2 + \rho_2 u_2^2, \tag{2.12}$$

$$H_1 + \frac{1}{2}u_1^2 = H_2 + \frac{1}{2}u_2^2. \tag{2.13}$$

In deriving relationships between the upstream and downstream states, it is convenient to use a dimensionless parameter, the Mach number, as the primary variable describing the flow. The Mach

number is the ratio of the flow velocity to sound speed,

$$M = \frac{u}{c}, \tag{2.14}$$

and manipulation of Eqns. 2.11-2.13 and the thermodynamic relations governing a perfect gas allow for the derivation of the relationships between the jump in a flow parameter as a function of the upstream Mach number and ratio of specific heats. These normal jump conditions may be written as [59]

$$\frac{P_2}{P_1} = 1 + \frac{2\gamma}{\gamma+1}\left(M_1^2 - 1\right), \tag{2.15}$$

$$\frac{\rho_2}{\rho_1} = \frac{u_1}{u_2} = \frac{(\gamma+1)\,M_1^2}{(\gamma-1)\,M_1^2 + 2}, \tag{2.16}$$

$$\frac{c_2^2}{c_1^2} = \frac{T_2}{T_1} = 1 + \frac{2\,(\gamma-1)}{(\gamma+1)^2}\frac{\gamma M_1^2 + 1}{M_1^2}\left(M_1^2 - 1\right), \tag{2.17}$$

$$M_2^2 = \frac{1 + \frac{\gamma-1}{2}M_1^2}{\gamma M_1^2 - \frac{\gamma-1}{2}}, \tag{2.18}$$

$$\frac{S_2 - S_1}{R} = ln\left[\left(\frac{P_2}{P_1}\right)^{\frac{1}{\gamma-1}}\left(\frac{\rho_2}{\rho_1}\right)^{\frac{-\gamma}{\gamma-1}}\right]. \tag{2.19}$$

The change in entropy, Eqn. 2.19, provides some final insights into flows involving shock waves. Expanding the expression in a series about $M_1 = 1$ results in

$$\frac{S_2 - S_1}{R} = \frac{2\gamma}{(\gamma+1)^2}\frac{\left(M_1^2 - 1\right)^3}{3} + O\left\{\left(M_1^2 - 1\right)^4\right\}. \tag{2.20}$$

Applying the second law of thermodynamics, the entropy cannot decrease in adiabatic flow, hence $M_1 \geq 1$. This means that the flow must be supersonic in order to support a shock wave, and as seen in Eqns. 2.15, 2.16, and 2.17, the jumps in pressure, density, and temperature are from lower to higher values. Further, the flow velocity must decrease across the shock wave, and some manipulation of Eqn. 2.18 will show that $M_2 \leq 1$. Thus, the velocity change across a normal shock must be from supersonic to subsonic. Finally, substituting Eqn. 2.15 into 2.20 shows the change in entropy is third order in the shock strength

$$\frac{S_2 - S_1}{R} = \frac{\gamma+1}{12\gamma^2}\left(\frac{\triangle P_1}{P_1}\right)^3 + O\left\{\left(\frac{\triangle P_1}{P_1}\right)^4\right\}. \tag{2.21}$$

Thus, for small finite shock waves there is a first-order correspondence between the change in pressure, velocity, density, and temperature, but only a third-order change in the entropy. This is

the reason an isentropic expansion wave can be treated as a series of weak shocks, as will be done in Section 2.2.

2.1.3 Oblique Shock Jump Equations

For cases in which the flow is not normal to the shock wave, the configuration shown in Figure 2.2 provides useful insights into the geometry of the problem. To avoid confusion with the previous results, the notation of Courant and Friedrichs [33] is adopted, in which β is the angle of obliquity (defined to be the angle between the shock wave and the upstream flow), q is the flow velocity, N is the component of velocity normal to the shock wave, L is the component of velocity tangent to the shock wave, and θ is the angle the flow is deflected in the downstream state. Since there is no pressure change tangent to the shock wave, the conservation equations can be used to show that the tangential velocity is not altered, hence $L_1 = L_2$. Further, the normal components of velocity must follow the normal shock jump conditions, and Eqns. 2.15-2.18 are valid for N_1 and N_2. Since $M_1 = \frac{q_1}{c_1}$, and $N_1 = q_1 sin\beta$,

$$\frac{N_1}{c_1} = M_1 sin\beta. \tag{2.22}$$

Thus, a factor of $sin\beta$ should be appended to M_1 whenever it occurs in Eqns. 2.15-2.18 . Eqn. 2.15, for example, becomes

$$\frac{P_2}{P_1} = 1 + \frac{2\gamma}{\gamma + 1}\left(M_1^2 sin^2\beta - 1\right). \tag{2.23}$$

The relationship between β and θ can be determined once again through the geometry, by noting

$$tan\beta = \frac{N_1}{L}, \tag{2.24}$$

$$tan\left(\beta - \theta\right) = \frac{N_2}{L}. \tag{2.25}$$

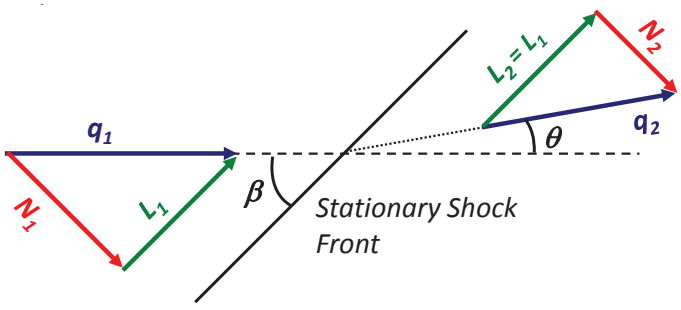

Figure 2.2: Passage of fluid through an oblique shock wave.

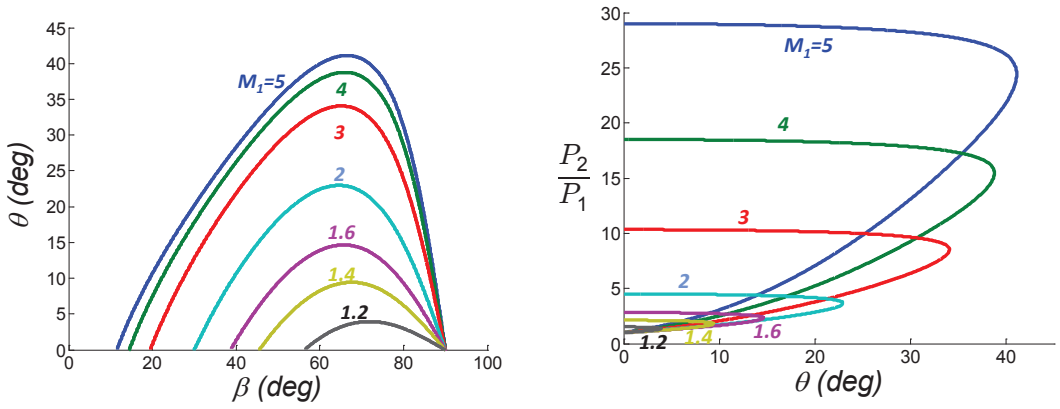

(a) (b)

Figure 2.3: Oblique shock solutions for various shock strengths for $\gamma = 1.4$.

Dividing Eqns. 2.24 and 2.25 and using conservation of mass, Eqn. 2.11, results in

$$\frac{tan\left(\beta-\theta\right)}{tan\beta} = \frac{N_2}{N_1} = \frac{\rho_1}{\rho_2} = \frac{\left(\gamma-1\right)M_1^2 sin^2\beta + 2}{\left(\gamma+1\right)M_1^2 sin^2\beta}. \tag{2.26}$$

Some trigonometric manipulation gives the explicit dependence on the angles as

$$tan\theta = 2cot\beta \frac{M_1^2 sin^2\beta - 1}{M_1^2\left(\gamma + cos2\beta\right) + 2}. \tag{2.27}$$

Equations 2.23 and 2.27 form a set of nonlinear equations for which the pressure, angle of obliquity, and angle of flow deflection form a unique set of curves for a given upstream Mach number. This is typically referred to as the $P-\theta-\beta$ relationship for oblique shocks. For reference, examples of these curves, referred to as shock polars, are plotted in Fig. 2.3.

A few of the key features of the shock polars should be noted. First, there is a minimum shock angle for which solutions exist. Examining Eqn. 2.23, as the shock strength goes to zero, $P_2 \rightarrow P_1$, and the so-called Mach angle, μ , is obtained as

$$\mu = sin^{-1}\left(\frac{1}{M_1}\right). \tag{2.28}$$

The Mach angle represents the weak limit of the oblique shock wave, essentially resulting in an infinitely small disturbance. The other limit, of course, is at $\beta = 90°$, which yields the normal shock solution. The form of the shock polar also results in a maximum deflection angle, θ_{max}, as seen in Figure 2.3 . The inability of an oblique shock to turn the flow past θ_{max} plays a key role the reflection phenomena discussed later. The final feature of the shock polar solution is the non-uniqueness of the wave angle. For a given Mach number and flow deflection, two unique solutions exist. The first is the lower pressure solution in which the downstream flow is supersonic, and is called the weak

solution. The second is the higher pressure solution, which results in subsonic downstream flow and is called the strong solution. The appropriate selection of the solution often depends directly on the downstream conditions as will be shown in the following sections.

2.1.4 Shock Polar Analysis of Reflection Phenomena

2.1.4.1 Regular Reflection

The simplest reflection to characterize is that of the a regular reflection such as the one shown in Figure 2.4. In the steady configuration, the gas at its initial state, characterized by M_1 and moving in a direction parallel to the wedge, encounters the incident shock at the wedge angle, β . Equations 2.23 and 2.27 are now sufficient to solve for the resulting downstream state. This is represented graphically in Figure 2.4(c) as point (2) , where P_2 and θ_2 correspond to the correct angle of obliquity. Since the angle of the wedge is constant, the downstream conditions require another shock wave to turn the flow to back to its original orientation. In this case, the Mach number and flow deflection are specified, and Eqns. 2.23 and 2.28 can be used to solve for the shock angle. Again, the graphical solution provides an intuitive solution, and the polar for this second shock wave, known as the reflected shock, is shown in Figure 2.4(c). The intersection of the reflected shock polar with $\theta = 0$ gives the reflected shock solution, state (3), where the correct choice of β is immediately obvious.

2.1.4.2 Mach Reflection

The Mach reflection is an irregular reflection phenomenon that results from the limitations on how much an oblique shock can alter the flow angle. In the example shown in Figure 2.5, a solution similar to that of a regular reflection is attempted. As demonstrated in Figure 2.5 (c), however, the reflected shock is no longer strong enough to turn the flow the back to its original orientation. Thus, instead of a simple reflected solution, a 3 shock solution develops where a so-called Mach stem branches off from the wedge and forms a triple point with the incident and reflected waves. Since the flow behind the reflected shock and the Mach stem must still satisfy mass and momentum conservation laws, the pressure and flow deflection in both states must be the same. This makes the $P - \theta$ shock polar a very useful tool in solving the problem graphically. As shown in Figure 2.5 (c), the point at which both the reflected wave and Mach stem polar (which is identical to the incident shock polar under a plane wave approximation) meet in $P - \theta$ space is the solution of the wave configuration and is labeled as states (3) and (4). While, by construction, $P_3 = P_4$ and $\theta_3 = \theta_4$, there are still discontinuities in the velocity, density, and entropy between the two states. As such, a vortex sheet, or slipstream, is generated to account for these discontinuities and separate the two states.

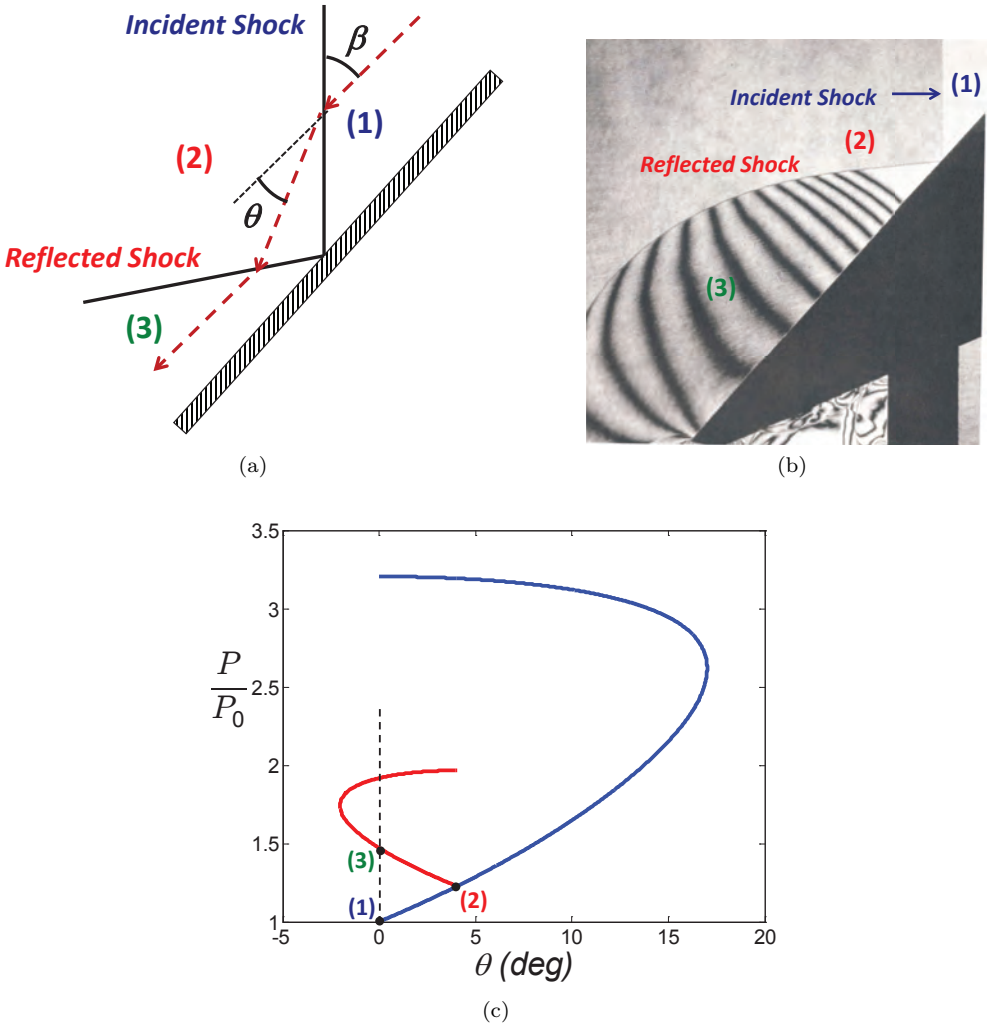

(a) (b)

(c)

Figure 2.4: Regular shock wave reflection with $M_1 = 1.7$ and $\beta = 40°$. The wave configuration is shown in (a), where the dotted line is a typical streamline of the flow. A holographic interferogram from [16] is shown in (b), and the corresponding shock polar diagram is shown in (c).

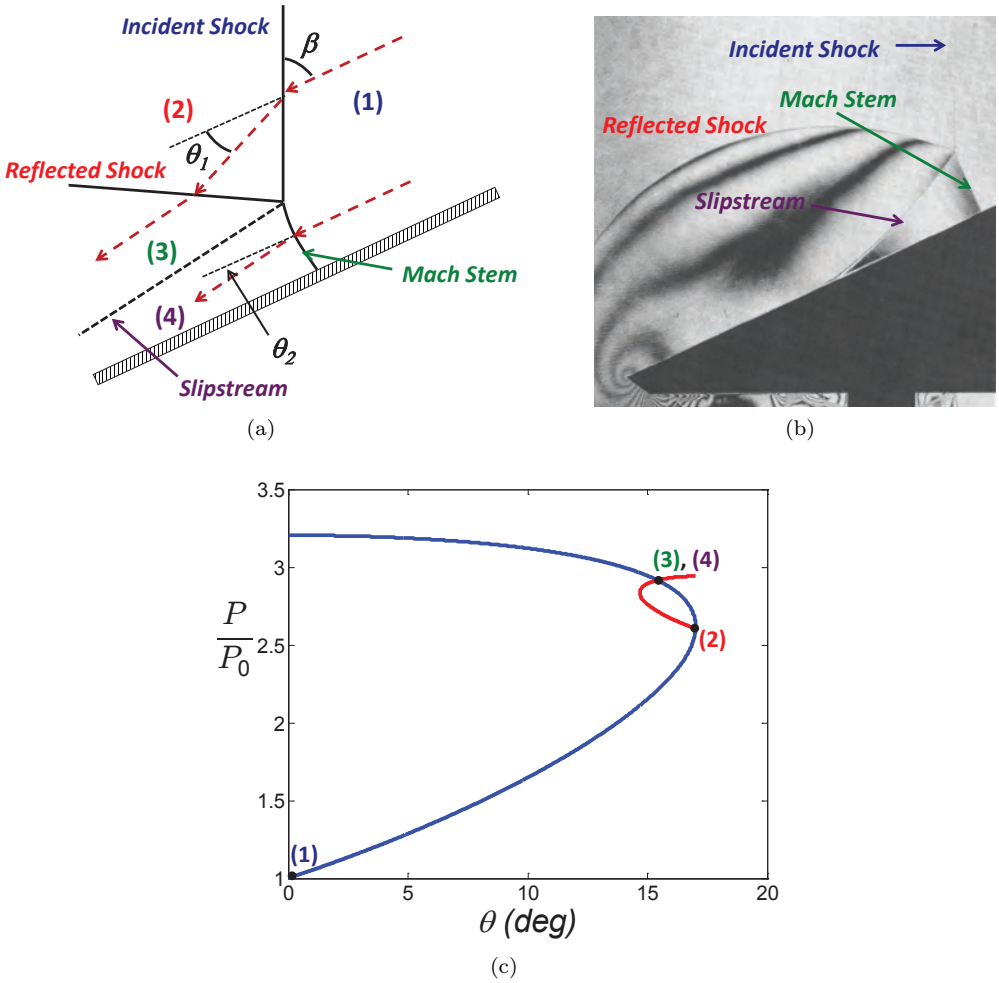

Figure 2.5: Regular shock wave reflection with $M_1 = 1.7$ and $\beta = 65°$. The wave configuration is shown in (a), where the dotted lines are typical streamlines of the flow. A holographic interferogram from [16] is shown in (b), and the corresponding shock polar diagram is shown in (c).

2.2 Solids

The theory of normal shock waves in solids is discussed briefly. The Lagrangian equations of motion are used to derive both the shock jump conditions and the differential forms governing simple wave motion. After introducing the Mie-Grüneisen EOS, the shock polar analysis from gas dynamics presented in the earlier section is developed for analyzing oblique shocks in solids. An application of the polar analysis in oblique shock reflection is given and then the Mach lens configuration is introduced and discussed. This configuration forms the basis of the work presented in this dissertation. A simple impedance matching solution to the configuration is given before the shock polar analysis of the steady state Mach wave configuration is presented.

2.2.1 Normal Shock Waves

Experiments involving the normal impact of plane parallel surfaces result in plane longitudinal waves. At times before the arrival of release waves from the lateral boundaries, the loading conditions produce a condition of uniaxial strain [31, 35, 42, 63, 65, 86]. The properties of the propagating wave are governed by the Lagrangian conservation equations of mass, momentum, and energy in the direction of the uniaxial motion given, respectively, by [35]:

$$\frac{\partial u}{\partial X} = \rho_0 \frac{\partial V}{\partial t}, \tag{2.29}$$

$$\frac{\partial \sigma_{11}}{\partial X} = -\rho_0 \frac{\partial u}{\partial t}, \tag{2.30}$$

$$\rho_0 \frac{\partial E}{\partial t} + \sigma_{11} \frac{\partial u}{\partial X} = -\frac{\partial Q}{\partial X}, \tag{2.31}$$

where X denotes the Lagrangian position of a particle, t is time, u is the particle velocity, ρ_0 is the initial density, V is the specific volume of a material element, σ_{11} is the Cauchy stress taken to be positive in compression, E is the specific internal energy, and Q is the heat flux vector. The jump between two states for a steady wave such as the one shown in Figure 2.6 can be examined by introducing a similarity variable,

$$\xi = X - Ct, \tag{2.32}$$

where C is the speed of the wave. The initial and final states of the wave are taken to be

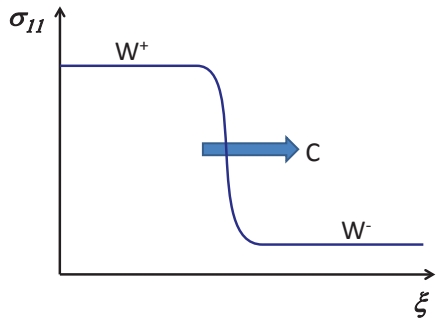

Figure 2.6: Steady plane wave propagating at velocity C, with clearly defined starting and ending states.

$$\begin{aligned} W^- : u &\rightarrow u^-, \sigma_{11} \rightarrow \sigma_{11}^-, V \rightarrow V^-, as\, \xi \rightarrow \infty, \\ W^+ : u &\rightarrow u^+, \sigma_{11} \rightarrow \sigma_{11}^+, V \rightarrow V^+, as\, \xi \rightarrow -\infty. \end{aligned} \tag{2.33}$$

Equations 2.29-2.31 can be rewritten under this transformation as

$$\frac{d}{d\xi}\left(u + \rho_0 C V\right), \tag{2.34}$$

$$\frac{d}{d\xi}\left(\sigma_{11} - \rho_0 C u\right), \tag{2.35}$$

$$\frac{d}{d\xi}\left(\rho_0 C E + Q\right) = \sigma_{11}\left(\xi\right)\frac{du}{d\xi}, \tag{2.36}$$

which are immediately integrable since ρ_0 and C are constant. Using the limits of integration given by Eqn. 2.33, the jump conditions can be written as

$$u^+ - u^- = -\rho_0 C\left(V^+ - V^-\right), \tag{2.37}$$

$$\sigma_{11}^+ - \sigma_{11}^- = -\rho_0 C\left(u^+ - u^-\right). \tag{2.38}$$

The energy equation, Eqn. 2.36, can be solved using integration by parts and yields

$$\sigma_{11}^+ u^+ - \sigma_{11}^- u^- + Q^+ - Q^- = \rho_0 C\left(E^+ - E^- + \frac{1}{2}\left(u^{+^2} - u^{-^2}\right)\right). \tag{2.39}$$

It should be noted that the derivation of these jump conditions describes the jump from an

initial to a final state at any point in the waveform. Therefore, another useful result can be seen in the limit of $W^- \to W^+$, where a differential form of the Lagrangian conservation equations under self-similar motion is obtained. These equations can be used to describe simple isentropic processes such as release waves and isentropic loading [5].

$$dV = -V_0 \frac{du}{C}, \tag{2.40}$$

$$d\sigma_{11} = \rho_0 C du. \tag{2.41}$$

In general, however, the structure of the wave is usually ignored, and the jump between the shocked and unshocked state is idealized as a discontinuous transition. Additionally, the transition is assumed to be adiabatic, hence $Q = 0$, and Eqns. 2.37-2.39, with the wave speed being the shock velocity, form the standard shock jump equations. The most commonly used form of these equations in the shock literature is for a shock propagating into a quiescent material [36], in which case conservation of mass and momentum are given by

$$\rho_0 U_s = \rho \left(U_s - u_p \right), \tag{2.42}$$

$$\sigma - \sigma_0 = \rho_0 U_s u_p, \tag{2.43}$$

where U_s is the shock velocity, u_p is the downstream particle velocity, and for simplicity, σ is understood to be the σ_{11} component of stress. Equation 2.39 can be manipulated using Eqns. 2.42 and 2.43 to eliminate the velocities and write conservation of energy as

$$E - E_0 = \frac{1}{2} \left(\sigma + \sigma_0 \right) \left(V_0 - V \right). \tag{2.44}$$

It can be seen in Eqns. 2.42, 2.43, and 2.44 that there are five unknown properties of the shock wave: U_s , u_p , σ , V , and E . If any two of these five parameters are known, then, the jump conditions allow for the complete characterization of the shocked state. If a series of these shocked states are measured for a given material, the resulting locus of points is called the Hugoniot. If the initial state is the undeformed material at standard temperature and pressure, the locus of points is referred to as the principal Hugoniot. Since, experimentally, it is easiest to measure velocities, most material Hugoniots are characterized by measuring the shock and particle velocities, although it is possible to measure stress using various gauges [17, 53]. As a result, a common expression for the

Hugoniot is to express the shock velocity as an expansion of the particle velocity such that

$$U_s = C_0 + s u_p + O\left(u_p^2\right). \tag{2.45}$$

For most materials, the linear form of Eqn. 2.45 is sufficient to describe a single-phase Hugoniot [72, 63, 36]. Thus, the empirical coefficients C_0 and s, which have been determined experimentally for a wide range of materials [62], can be used to write any shock parameter in terms of another. In other words, once the Hugoniot is known, a specification of one of the shock parameters completely determines the entire shocked state.

2.2.1.1 Plate Impact Experiment and Impedance Matching

An immediate use of the Hugoniot may be seen in the concept of impedance matching [72, 60]. As an example, consider a simple plate impact thought experiment where material A impacts material B at an initial velocity u_I as shown in Fig. 2.7(a). Upon impact, a right moving shock propagates into material B, which is at rest, and a left moving shock propagates into material A, which already has a particle velocity equal to the impact velocity. Each shock, then, may be represented by the respective material Hugoniots, where B is simply the standard principal Hugoniot, and A is given an initial particle velocity of u_I and negative motion since it is moving in the opposite direction. The strength of each shock wave can be determined uniquely by solving each set of jump conditions with the constraint that the shocked stress and particle velocity behind the two waves are equal. The first condition is simply a traction balance at the boundary because the unit normal is in the direction of motion. Since the materials are only in compression at this point, there can be no generation of gaps or voids, hence the particle velocities must also be equal, giving the second condition. Relating the equilibrium stresses through Eqns. 2.43 and 2.42 gives an implicit equation for the equilibrium particle velocity, u_p^+,

$$\rho_0^B \left[C_0^B + s^B u_p^+\right] u_p^+ = \rho_0^A \left[C_0^A + s^A \left(u_I - u_p^+\right)\right] \left(u_I - u_p^+\right). \tag{2.46}$$

This solution is illustrated graphically in Fig. 2.7(b), where the intersection of the Hugoniot curves in $\sigma - u_p$ gives the shocked state, W^+. For a more complete picture of the problem, the wave interactions can be examined through the use of the $X - t$ diagram shown in Fig. 2.7(c). As shown, the shocks will reflect off their respective free surfaces as release waves, and the interaction of these release waves can result in tension in the material, a concept used in designing spall experiments. An illustration of the wave profile at the tracer position is shown in Fig. 2.7(d). The shock arrives at the tracer at time t_1, which shocks the material to the state given by W^+. The material will remain at this constant Hugoniot state until time t_2 when the expansion wave from the free surface arrives. At time t_3 the end of the rarefaction arrives, which completes the release of the material

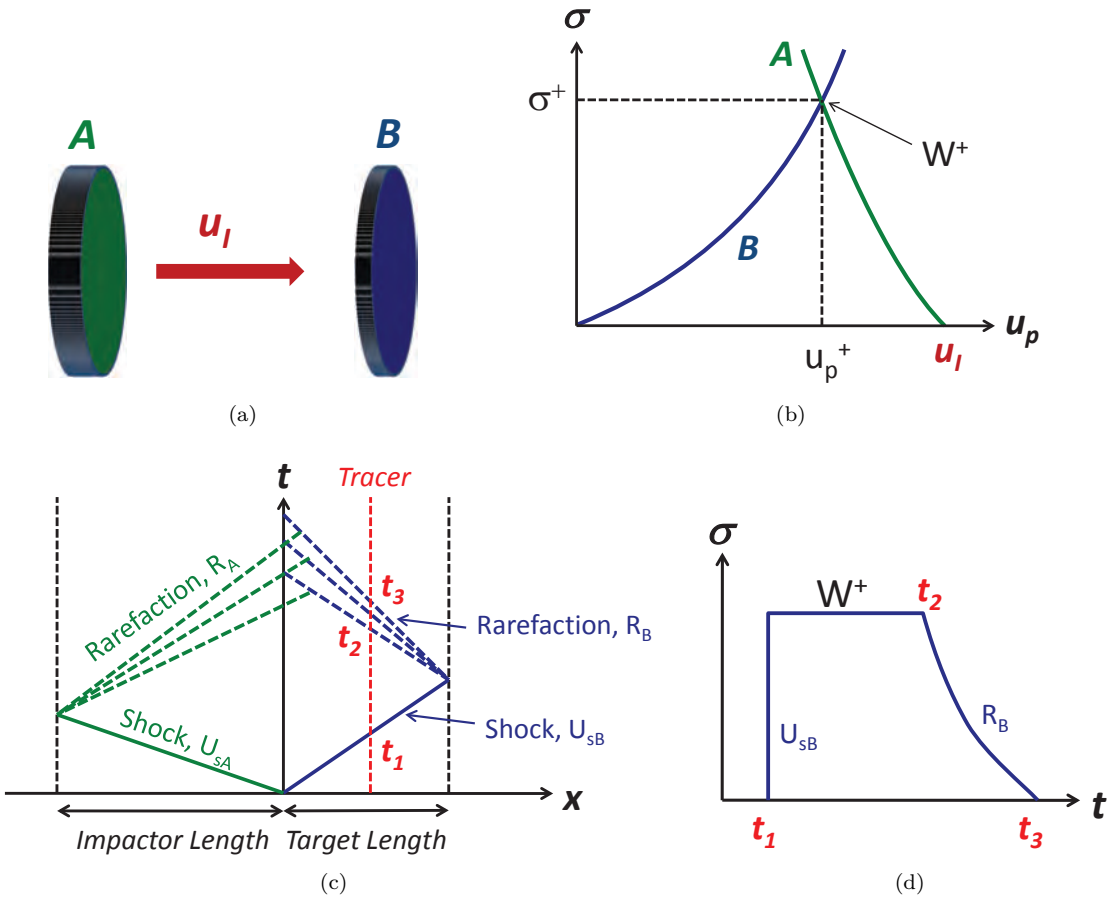

Figure 2.7: Standard plate impact experiment (a) utilizes thin flat plates as impactors and targets. Impedance matching (b) gives the shocked state in each material after impact. An X-t diagram (c) illustrates the wave interactions. The waveform generated at the tracer location in (c) is shown in (d).

from the Hugoniot state to the zero stress boundary condition.

2.2.2 Mie-Grüneisen Equation of State

Up to this point, the Hugoniot has been sufficient to describe and relate the mechanical properties of shock waves. However, a complete description of the thermodynamic equation of state is required to solve for processes taking place off the Hugoniot. The Mie-Grüneisen EOS is often selected as the most appropriate form, and a complete description of its origins, validity, and derivation can be found in the literature [74, 73, 72, 35]. Therefore, only a general summary of the EOS will be discussed here. The Grüneisen coefficient is a fundamental thermodynamic derivative that can be

expressed as

$$\gamma = V\frac{\partial P}{\partial E}\bigg|_V = -\frac{V}{T}\frac{\partial T}{\partial V}\bigg|_S = -V\frac{\partial\left[ln\left(T/T_R\right)\right]}{\partial V}\bigg|_S, \tag{2.47}$$

where T is the temperature, S is the entropy, and the subscript R refers to a reference state. The Mie-Grüneisen class of materials are those with the restriction that γ is a function of only V. It can be shown using various means [72, 35] that under this assumption, the pressure and specific internal energy at a given volume, can be related to the Hugoniot curve by

$$P\left(V\right) - P^H(V) = \frac{\gamma\left(V\right)}{V}\left[E\left(V\right) - E^H(V)\right], \tag{2.48}$$

where the superscript H refers to the Hugoniot. Equation 2.48 is generally referred to as the *Mie-Grüneisen P-V-E equation of state* and is widely used in shock compression analysis to determine the hydrodynamic response of many common materials in the range of pressures to a few hundred GPa [35]. Using this EOS, the Hugoniot can now be used to construct relationships to other thermodynamic response curves such as isotherms, isentropes, and recentered Hugoniots. Of particular interest in this work is the ability to estimate the material response from a shocked state where, in general, the material is idealized to either expand isentropically or reshock.

2.2.2.1 Isentrope

In general, a material will release from a shocked state with an expansion wave. Since an expansion is idealized as an infinite number of weak shocks, the process is assumed to be isentropic and, hence, the unloading path follows the isentrope. Since the isentrope is passing through the shocked state, which is a point on the Hugoniot, as shown in Fig. 2.8, the principal Hugoniot can be used in conjunction with Mie-Grüneisen EOS to calculate the unloading path. Evaluating a point along the isentrope from Eqn. 2.48 yields

$$P^S\left(V\right) - P^H(V) = \frac{\gamma\left(V\right)}{V}\left[E^S\left(V\right) - E^H(V)\right]. \tag{2.49}$$

The internal energy along an isentrope can be determined by integrating the thermodynamic derivative

$$\left(\frac{\partial E}{\partial V}\right)_S = -P, \tag{2.50}$$

along a path of constant entropy through the point of interest on the Hugoniot, W^+, giving

$$E^S\left(V, W^+\right) = E^+ - \int_{V^+}^{V} P^S\left(V', W^+\right) dV'. \tag{2.51}$$

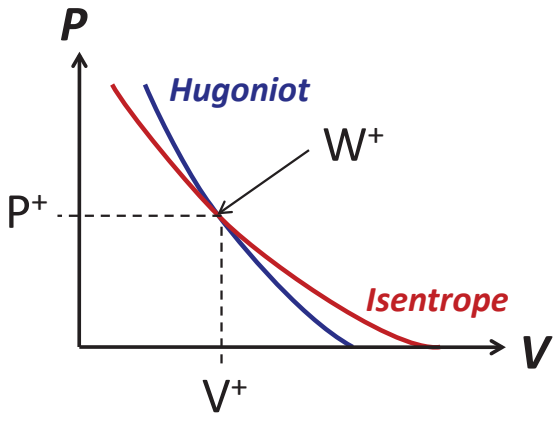

Figure 2.8: Construction of an isentrope through a point on the Hugoniot.

Substituting the Rankine-Hugoniot relation, Eqn. 2.44 , for E^+ and E^H yields the pressure offset of the isentrope from the Hugoniot as

$$P^S\left(V;W^+\right)=\frac{\gamma\left(V\right)}{V}\left[-\int_{V^+}^{V}P^S\left(V^{'};W^+\right)dV^{'}+\frac{1}{2}P^+\left(V_0-V^+\right)\right]+\left[1-\frac{1}{2}\frac{\gamma\left(V\right)}{V}\left(V_0-V\right)\right]P^H\left(V\right). \tag{2.52}$$

This integral equation can be solved by differentiating it to convert it to a linear first-order ordinary differential equation. A common assumption that makes the calculation much simpler is to assume the Grüneisen coefficient has a linear dependence on the volume [35] such that

$$\frac{\gamma}{V}=\frac{\gamma_0}{V_0}, \tag{2.53}$$

where Slater's relation [74] for an isotropic elastic body and constant Poisson's ratio makes it possible to estimate the initial Grüneisen coefficient as [72]

$$\gamma_0=2s-1. \tag{2.54}$$

Under these assumptions, the differential equation of interest becomes

$$\frac{dP^S\left(V;W^+\right)}{dV}+\frac{\gamma_0}{V_0}P^S\left(V;W^+\right)=\kappa\left(V\right), \tag{2.55}$$

where

$$\kappa\left(V\right)=\frac{1}{2}\frac{\gamma_0}{V_0}P^H\left(V\right)+\left[1-\frac{1}{2}\frac{\gamma_0}{V_0}\left(V_0-V\right)\right]\frac{dP^H\left(V\right)}{dV}. \tag{2.56}$$

The solution to Eqn. 2.55 may be written as

$$P^S\left(V;W^+\right)=\chi\left(V\right)\left[P^+ + \int_{V^+}^{V}\frac{\kappa\left(V'\right)}{\chi\left(V'\right)}dV'\right], \tag{2.57}$$

where

$$\chi\left(V\right)=exp\left[\frac{\gamma_0}{V_0}\left(V^+ - V\right)\right]. \tag{2.58}$$

The description of the wave propagation idealized in Figure 2.7, can now be completed since the reflection of the shock at the free boundary produces isentropic release waves that then follow the thermodynamic path governed by Eqn. 2.57. Additionally, Eqns. 2.40 and 2.41 can be used to solve for the evolution of the isentropic wave in space and time.

2.2.2.2 Second Shock Hugoniot

For calculations which involve the propagation of shocks into a material that has already been compressed by a shock, such as reflected shock waves, the Mie-Grüneisen EOS can be used to calculate a recentered Hugoniot. The scenario is illustrated in Figure 2.9. Once again, the Rankine-Hugoniot equation, Eqn. 2.44, can be used to define the transition from the shocked state, W^+, to the second-shock Hugoniot, designated by the superscript H_2 , as

$$E^{(H_2)}\left(V\right)=E^+ + \frac{1}{2}\left[P^{(H_2)}\left(V\right)+P^+\right]\left(V^+ - V\right), \tag{2.59}$$

where the energy states can be related to a reference state as

$$E^{(H_2)}\left(V\right)=E_0 + \frac{1}{2}P^{(H_2)}\left(V\right)\left(V_0 - V\right), \tag{2.60}$$

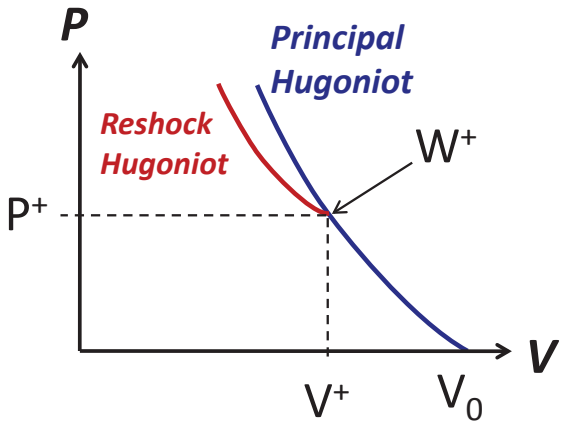

Figure 2.9: Construction of a second-shock Hugoniot through a point on the principal Hugoniot.

and

$$E^{+} = E_0 + \frac{1}{2}P^{+}\left(V_0 - V^{+}\right). \tag{2.61}$$

Substituting Eqns.2.59-2.61 into the general form of the EOS, Eqn. 2.48, gives the re-shock Hugoniot as [35]

$$P^{(H_2)}(V) = \frac{P^{(H)}(V)\left[1 - \frac{\gamma(V)}{2V}(V_0 - V)\right] + \frac{\gamma(V)}{2V}P^{+}(V_0 - V)}{1 - \frac{\gamma(V)}{2V}(V^{+} - V)}. \tag{2.62}$$

2.2.3 Steady 2-D Supersonic Flow

2.2.3.1 Oblique Shock Waves

In this section an analogous form of the oblique shock equations given in Section 2.1.3 is derived for the shock compression of solids. A complete description of the Riemann problem for hydrodynamic flow in a solid is thoroughly reviewed by Menikoff and Plohr [64], and, as such, only the results relevant to the shock polar analysis are derived. Here, it is sufficient to only use the mechanical properties given by a material Hugoniot: the shock and particle velocities, pressure, and density. It should be noted that this is a hydrodynamic approximation so any aspects of a deviatoric response are ignored and the stress tensor is characterized only by the pressure, $P = \frac{1}{3}\sigma_{xx}$. It will once again be useful to work in the Eulerian frame shown in Figure 2.10. As discussed previously, the tangential components of velocity are conserved across the oblique shock, while the normal components must follow the normal shock jump conditions. In the solids community, the normal jump conditions have been conveniently defined in terms of U_s and u_p, which are shifted to the stationary shock frame in Figure 2.10a. Thus, $N_1 = U_s$ while $N_2 = U_s - u_p$, and the geometry immediately yields a trio of

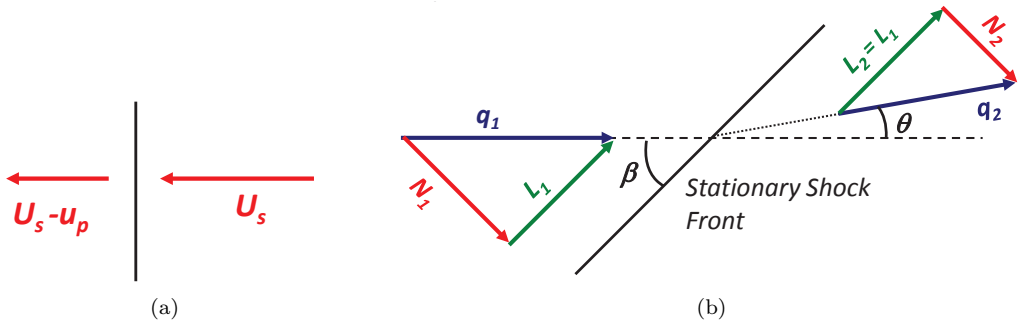

Figure 2.10: Flow of a solid through an oblique shock wave.

useful relations:

$$sin\beta = \frac{U_s}{q_1}, \tag{2.63}$$

$$tan\beta = \frac{U_s}{L_1}, \tag{2.64}$$

$$tan\left(\beta - \theta\right) = \frac{U_s - u_p}{L_1}. \tag{2.65}$$

Noting the trigonometric identity

$$tan\left(\beta - \theta\right) = \frac{tan\beta - tan\theta}{1 + tan\beta tan\theta}, \tag{2.66}$$

Eqns. 2.64 and 2.65 can now be combined to show

$$\frac{U_s - L_1 tan\theta}{L_1 + U_s tan\theta} = \frac{U_s - u_p}{L_1}. \tag{2.67}$$

Solving for $tan\theta$ yields

$$tan\theta = \frac{L_1 u_p}{L_1^2 + U_s^2 - U_s u_p}, \tag{2.68}$$

and using the Pythagorean theorem,

$$L_1^2 = q_1^2 - U_s^2, \tag{2.69}$$

gives an implicit relation for θ in terms of the upstream flow velocity, q_1 , and the Hugoniot represented by U_s and u_p

$$tan\theta = \frac{\left(q_1^2 - U_s^2\right)^{\frac{1}{2}} u_p}{q_1^2 - U_s u_p}. \tag{2.70}$$

Since the Hugoniot variables can be parametrized by the pressure through the conservation of momentum, Eqns. 2.63 and 2.70 represent the $P - \theta - \beta$ relationship for a general form of the Hugoniot for a solid [64]. For example, in the case of a linear form of the Hugoniot (Eqn. 2.45) and using $P = \rho_0 U_s u_p$ (Eqn. 2.43), the shock and particle velocities can be rewritten only as functions of pressure, initial density, and the empirical coefficients

$$U_s = \frac{C_0}{2}\left(1 + \sqrt{1 + \frac{4s}{\rho_0 C_0^2}P}\right), \tag{2.71}$$

$$u_p = \frac{C_0}{2s}\left(\sqrt{1+\frac{4s}{\rho_0 C_0^2}P}-1\right). \tag{2.72}$$

Substituting Eqns. 2.71 and 2.72 into 2.70 and 2.63 yields an analytic form of the shock polars for a linear Hugoniot

$$sin\beta = \frac{C_0}{2q_1}\left(1+\sqrt{1+\frac{4s}{\rho_0 C_0^2}P}\right), \tag{2.73}$$

$$tan\theta = \frac{\rho_0 C_0}{2s\left(\rho_0 q_1^2 - P\right)}\left(\sqrt{1+\frac{4s}{\rho_0 C_0^2}P}-1\right)\left[\rho_0 q_1^2 - \frac{sP}{\rho_0} - \frac{C_0^2}{2}\left(1+\sqrt{1+\frac{4s}{\rho_0 C_0^2}P}\right)\right]^{\frac{1}{2}}. \tag{2.74}$$

As will be shown later, the polars derived here for a solid share the same qualitative features of the polars calculated for a perfect gas in Section 2.1.3.

2.2.3.2 Expansion Waves

While shock waves generally compress the fluid, increasing the pressure and density, the flow also has the ability to expand. As was shown previously, expansion shocks for the materials of interest here violate the second law of thermodynamics, hence the expansion must occur through an isentropic process. One view of an isentropic expansion is that the flow turns by means of an infinite number of weak shocks. The analogous form of the Mach angle in a solid can be calculated the same way as in fluids and is determined by the instantaneous Eulerian wave speed, C_E and flow velocity, u.

$$\mu = sin^{-1}\left(\frac{C_E}{u}\right). \tag{2.75}$$

Thus, an infinite number of weak shocks at varying Mach angles provides the means for the material to expand. The turning of such a flow is shown in Figure 2.11, where the change in the deflection angle from the initial Mach angle results in an increase in flow velocity.

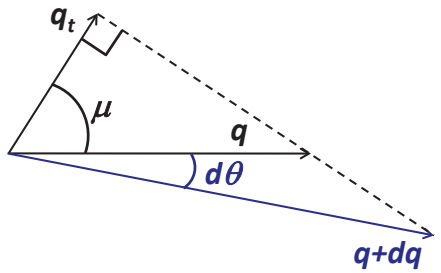

Figure 2.11: Velocity change in an infinitesimal expansion for a solid.

The tangential component of the velocity is once again conserved, and may be written as

$$u_t = ucos\mu = (u + du)\, cos\,(\mu + d\theta)\,. \tag{2.76}$$

Expanding the cosine term, and using the small angle approximation for $d\theta$ ($cosd\theta \approx 1$, $sind\theta \approx d\theta$) results in

$$ucos\mu = (u + du)\,(cos\mu - d\theta sin\mu)\,, \tag{2.77}$$

for which the higher-order term, $dud\theta sin\mu$, can be eliminated giving

$$d\theta = cot\mu \frac{du}{u}. \tag{2.78}$$

‘

Using the geometry of Mach angle, Eqn. 2.75 can be rewritten as

$$cot\mu = \sqrt{\left[\frac{u}{C_E\,(u)}\right]^2 - 1}, \tag{2.79}$$

which results in a differential relation between θ and u,

$$d\theta = \sqrt{\left[\frac{u}{C_E\,(u)}\right]^2 - 1}\frac{du}{u}. \tag{2.80}$$

The Eulerian wave speed can be calculated from Eqns. 2.40 and 2.41 and scaling by the Jacobian to convert from the Lagrangian to Eulerian frames as

$$C_E = \frac{\rho_0}{\rho}C = \sqrt{\left(\frac{\partial P}{\partial \rho}\right)_s}, \tag{2.81}$$

which is consistent with the previous definition given in Section 2.1.1. Since the isentrope can be calculated numerically from any state on the Hugoniot through Eqn. 2.8, the derivative can also be calculated, allowing $C_E\,(u)$ to be determined. Equation 2.80 can now be integrated to relate the change in flow angle to the flow velocity:

$$\theta = \int_{u_0}^{u} \sqrt{\left[\frac{u'}{C_E\,(u')}\right]^2 - 1}\frac{du'}{u'} + \theta_0. \tag{2.82}$$

The corresponding pressure can be determined assuming simple wave propagation and integrating Eqn. 2.41 as

$$P = \int_{u_0}^{u} \rho_0 C_E\,(u')\, du' + P_0. \tag{2.83}$$

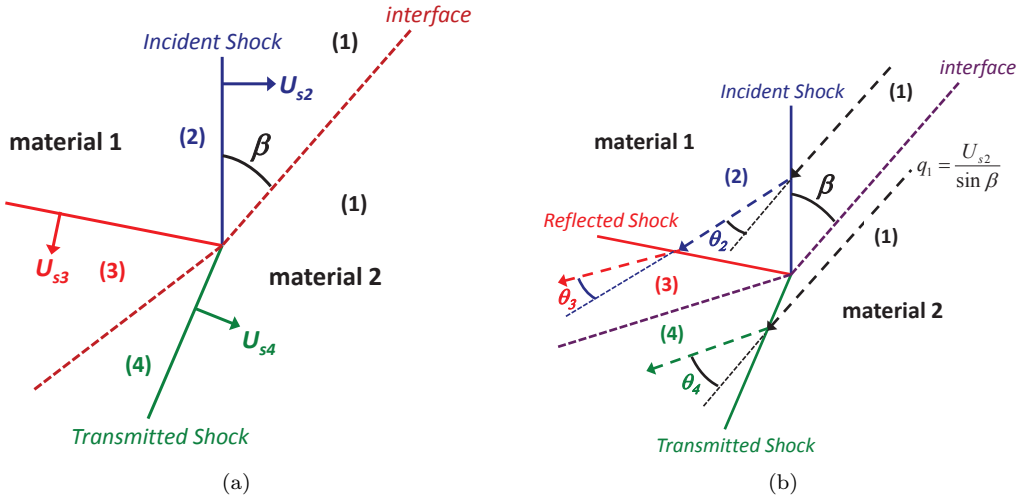

Figure 2.12: Steady state oblique shock reflection at oblique interface in a solid. The reference frame of the moving shock front (a) presents a very different problem from that of the stationary frame (b).

2.2.4 Shock Polar Analysis of Oblique Shock Reflections in Solids

A direct application for the use of these shock polars is in the interaction of an oblique shock with a material interface. This situation is analogous to what was discussed previously for reflections in gases in Section 2.1.4. The analysis, however, is slightly more complicated since a rigid body approximation for the wedge cannot be made under these circumstances, which results in a transmitted shock into the second material. The problem is illustrated in Figure 2.12(a), where a shock traveling at velocity U_{s2} in material 1 reflects off of material 2, which is at an angle β relative to the shock. The interaction results in a reflected oblique shock propagating back into the already shocked material 1, and a transmitted oblique shock into material 2. While it is possible to solve the problem in this moving shock frame, as was done recently by Loomis and Swift [61], a more elegant solution can be obtained by examining the stationary shock frame. In the stationary frame (Figure 2.12(a)), the upstream velocity becomes

$$q_1 = \frac{U_{s2}}{sin\beta}. \tag{2.84}$$

Since both the shock velocity and the oblique shock angle are already specified in the problem, the shocked state (2) is already known. To solve for the reflected (state 3) and transmitted shocks (state 4), the usual assumption of a slipstream between the two materials will be used, in which case the pressure and flow deflection angles are required to be the same. This solution is illustrated graphically using shock polars in Figure 2.13, where the reflected shock polar Hugoniot is generated using Eqn. 2.62. The incident and transmitted shocks are propagating into quiescent materials,

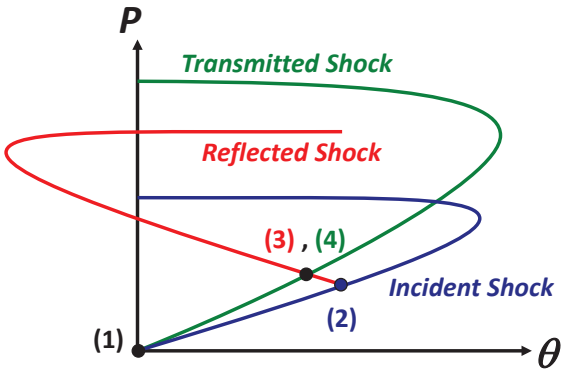

Figure 2.13: Shock polar solution for the configuration in Figure 2.12(b).

Table 2.1: EOS parameters used by Loomis and Swift [61].

Material	$\rho_0\ (g/cm^3)$	$C_0\ (km/s)$	s	γ_0
Copper	8.930	3.940	1.49	2.02
Beryllium	1.850	8.000	1.124	1.11

hence the polars begin at the origin. The reflected shock polar is traveling in the opposite direction beginning from shocked state (2), and as shown, the intersection with the transmitted polar in $P-\theta$ space closes the solution.

This type of graphical solution provides a very intuitive view of how the reflections are required to behave. For example, the solution proposed in Figure 2.13 illustrates the need for the reflected shock since the incident shock polar lies below the transmitted shock polar for the prescribed angle. This matches the type of oblique shock solution expected based on the desired wave configuration shown in Figure 2.12. Further examination of Figure 2.13, however, brings about the question of what happens when the incident shock polar lies above the reflected polar as is illustrated in Figure 2.14(a). In this case, the shock pressure of the incident shock is higher for all possible configurations. Physically, this means that a reflected shock cannot possibly be used to bring the flow to the same pressure as any transmitted shock. Thus, a pressure relieving feature is required, in which case an expansion can be used to decrease the pressure and turn the flow to the appropriate state as illustrated in Figure 2.14(b). Again, the nature of the shock polars in Figure 2.14(a), makes this solution obvious, and an expansion wave described by Eqns. 2.82 and 2.83 can be used to complete the solution.

Validation of these types of solutions was performed by comparison with the previous analytic and computational results obtained by Loomis and Swift [61]. In this study, copper/beryllium systems, with the material properties shown in Table 2.1, were studied for varying interface angles.

Two different systems were examined: one in which the lower impedance material (beryllium)

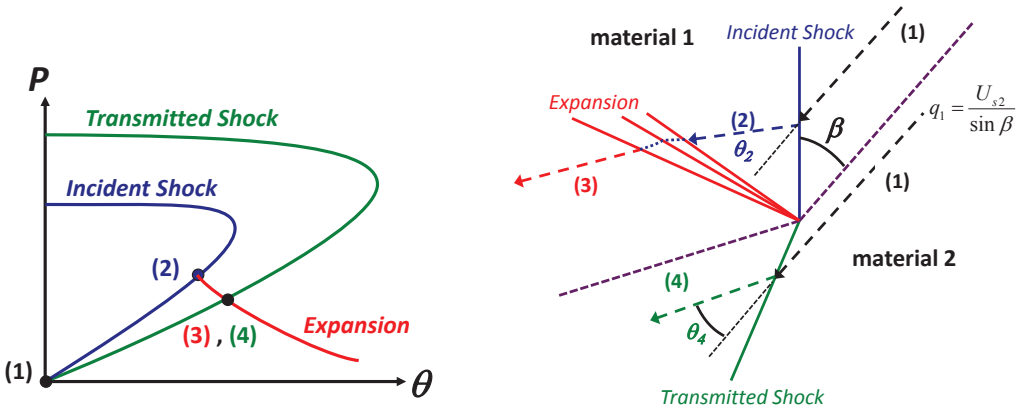

(a) (b)

Figure 2.14: Steady state oblique shock reflection in a solid requiring an expansion wave at oblique interface. The shock polar solution (a) illustrates the need for the rarefaction in the wave configuration (b).

Table 2.2: Shock angles given in degrees for copper impacting a beryllium / copper target at 500 m/s.

Incident	Reflected[a]	Transmitted[a]
10	15 / 9.9 / 9.74	5 / 5.0 / 5.04
30	34 / 29.2 / 29.36	14 / 14.5 / 14.61
50	53 / - / 49.28	23 / - / 22.60
70	65 / No Solution / 68.39	27 / No Solution / 27.71

[a] numerical simulation [61] / Lagrangian analysis[61] / shock polar analysis

Table 2.3: Shock angles given in degrees for copper impacting a copper / beryllium target at 400 m/s.

Incident	Reflected[a]	Transmitted[a]
10	8 / 9.4 / 9.30	20 / 19.8 / 19.96
20	18 / 19.0 / 18.64	42 / 42.1 / 42.53
30	30 / singularity / irregular	74 / singularity / irregular

[a] numerical simulation [61] / Lagrangian analysis[61] / shock polar analysis

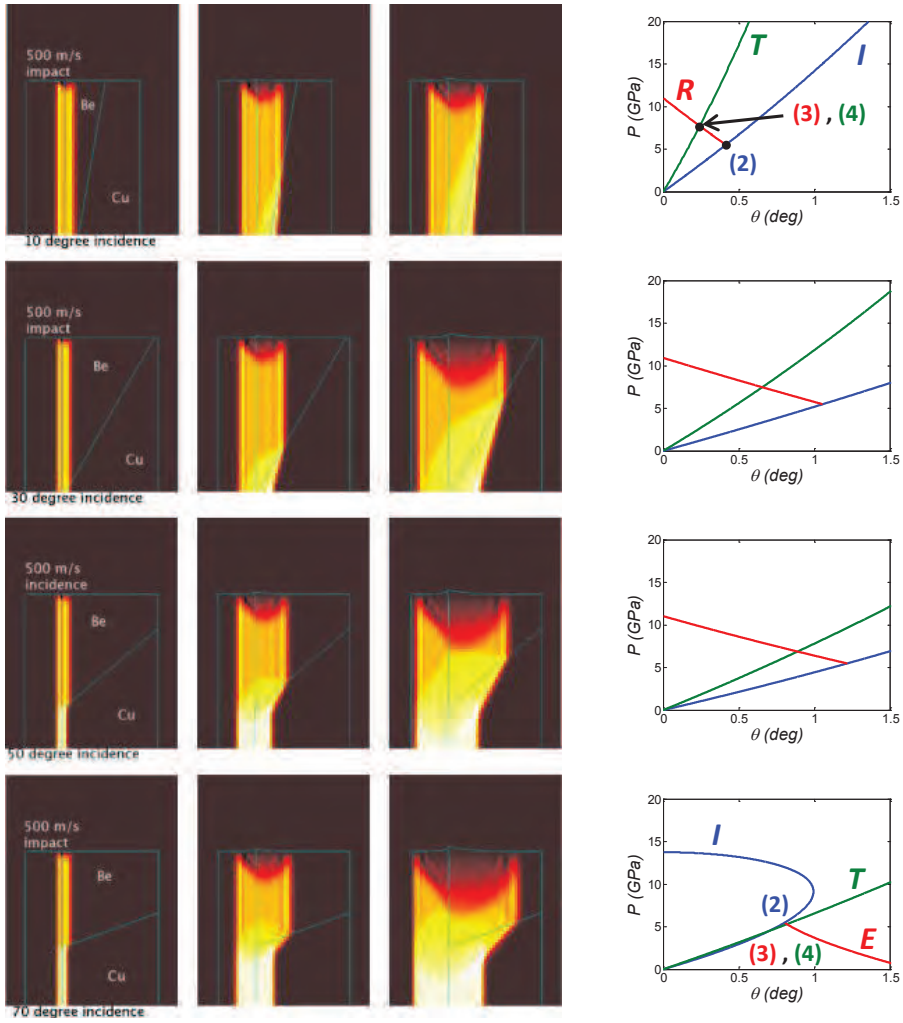

Figure 2.15: Pressure contours of the numerical simulations from [61] along with the present shock polar solution for a shock from beryllium transmitting into copper. Scale of the thermal map color is -1 GPa (black) to 10 GPa (white).

transmits into the higher impedance material (copper), and the other with the materials reversed. Numerical simulations of the first system in which a copper plate impacts a beryllium with varying copper interface angles at 500 m/s are shown along with the shock polar solution of the impact in Figure 2.15. The simulations shown are pressure contours showing the evolution of the shock reflection in the physical configuration with time.

A quantitative comparison of the shock reflection angles obtained for these configurations is shown in Table 2.2. The table gives a comparison of the angles obtained by Loomis and Swift [61] from their numerical simulations and analytic solutions along with the angles obtained under the same loading conditions from the current shock polar analysis. The results from all of the methods are in reasonable agreement, and the agreement between the two analytic solutions, in particular, is extremely good. This should not be unexpected as the same problem is being solved in two different

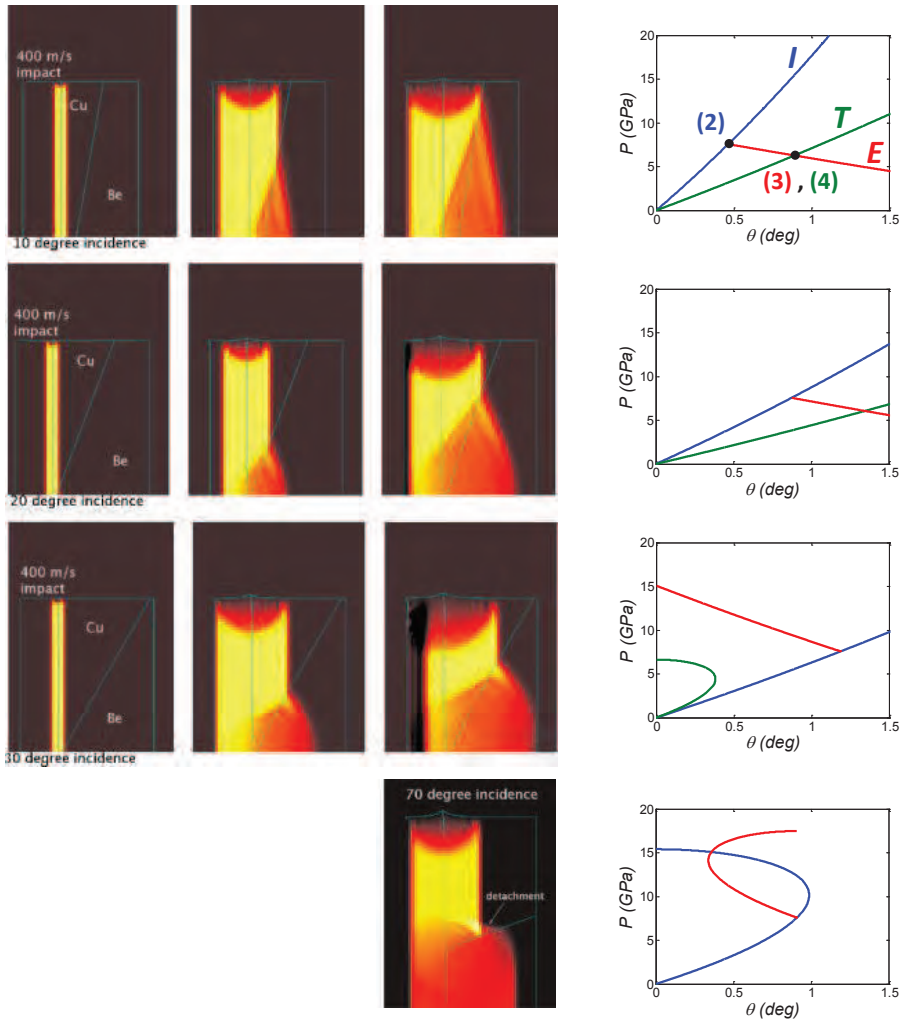

Figure 2.16: Pressure contours of the numerical simulations from [61] along with the present shock polar solution for a shock from copper transmitting into beryllium. Scale of the thermal map color is -1 GPa (black) to 10 GPa (white).

ways, and only serves to illustrate the validity and usefulness of the polar method. It is interesting to see that no solution is reported for the 70° angle of incidence. This is most likely due to the fact that the solution they were looking for only included reflected shock waves. However, as shown in Figure 2.15, and as was discussed previously, the proper solution requires the use of an expansion wave. In this case, the polar solution is once again in good agreement with the simulation.

The same set of analytical tools can be applied to the second case, where copper transmits into beryllium. Pressure contours from the simulation along with the shock polars can once again be seen in Figure 2.16, along with a summary of the angles in Table 2.3.As shown Figure 2.16, solutions involving an expansion wave can be found for the 10° and 20° angles of incidence and are in good agreement with previous results. However, at the higher angles of incidence ($\gtrsim 30°$) , a standard reflection solution cannot possibly be constructed since the incident and transmitted waves cannot

be connected with either a reflected shock or a rarefaction wave. This is analogous to what is seen in the irregular reflection domain discussed in Section 2.1.4. Therefore, an irregular reflection in the form of a detached wave is expected. This is clearly observed in the 70° simulation shown in Figure 2.16.

2.2.5 Mach Lens Configuration

2.2.5.1 Background and Motivation

As described previously, the plate impact experiment provides a well controlled environment for which a repeatable one dimensional plane shock wave is generated on impact. While this type of configuration provides an excellent technique for studying the shock behavior of materials, the shock stresses that can be accessed are limited by the velocity of the impactor. As such, there has been considerable interest in finding new experimental methods to increase the range of impact velocities. Gun systems, for example, were traditionally limited to projectile velocities of $\sim 1.2\ km/s$ and 2.3 km/s for gas and powder guns, respectively, until the advent of the two-stage light-gas gun in 1957 [34]. The two-stage gun makes use of an explosively driven piston to compress a light gas such as hydrogen which then produces impact velocities of up to 8 km/s. Another dramatic increase in impact capabilities came with the development of the three-stage or hypervelocity launcher. In this system, a third stage launch package is mounted on to the muzzle of a two-stage light-gas gun. The two-stage gun is used to launch a graded density impactor, which then creates a quasi-isentropic load on the launch package. Upon loading, the launch package remains at a relatively low temperature, but accelerates to velocities approaching 16 km/s [27, 28]. More recently, magnetic loading using Sandia National Laboratories' Z machine has been examined as a possible means to load a material isentropically [45]. This loading is similar in nature to the three-stage launch, and incredible flyer velocities, on the order of 25 km/s, have been achieved [57].

A summary of the current flyer plate launch capabilities is given in Figure 2.17, where a symmetric impedance matching diagram for titanium is shown for the each technique's maximum launch velocity. Titanium was selected here because it is commonly used as a three-stage or Z machine flyer plate since it is relatively lightweight but has a strength high enough to avoid fragmentation and spall. Of course, impacts involving higher impedance materials will produce higher stresses, but this impedance matching diagram still gives a rough estimate of the types of stresses expected at these impact velocities. As shown, gas guns produce impact stresses on the order of 15 GPa while powder guns roughly double this range to 30 GPa . The higher velocity techniques extend the impact stresses to approximately 150 GPa, 500 GPa , and 1 TPa for the two-stage, three-stage, and Z accelerator techniques, respectively. As illustrated, these higher velocity techniques, particularly the three-stage and Z accelerator methods, are capable of achieving tremendous pressures. These

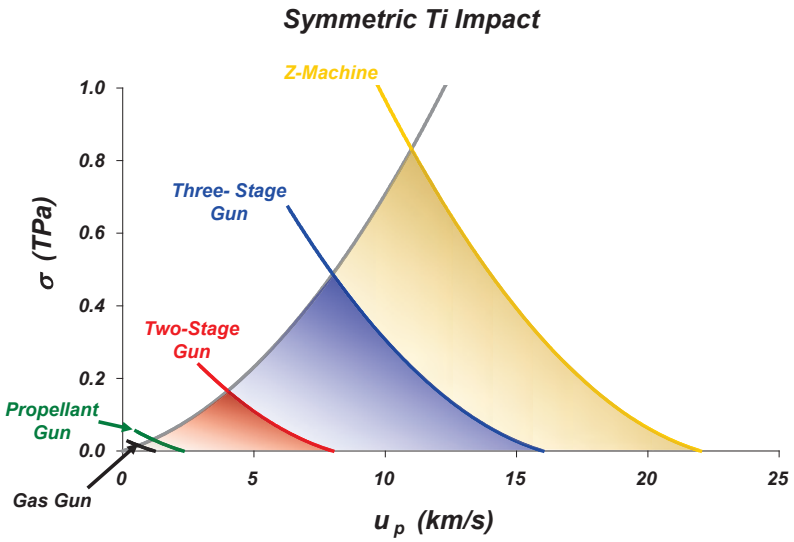

Figure 2.17: Mach lens target configuration. A plane shock is generated with a standard normal plate impact on the left.

facilities, however, are extremely specialized and are generally not very accessible, particular in a university setting.

As shown in Section 2.1.4, significant pressure increases can also be achieved through the interaction of shock waves. Thus, in an attempt to increase the pressures accessible in more conventional impact experiments, converging shocks waves are examined. A Mach reflection, in particular, is desired since it provides larger pressure gains than a regular reflection. As shown in Figure 2.5, the Mach stem is approximately normal to the flow, and thus, will have a higher pressure jump than an oblique shock. As it turns out, Mach reflections in solids are, at least theoretically, relatively easy to generate experimentally. The first experimental observations of such reflections were made by Al'tshuler et al. by using a plane wave generators to explosively load an aluminum wedge [7]. Shortly after, Fowles and Isbell adapted the use of axially symmetric copper targets with a confining high explosive to generate steady state Mach waves, for which elevated pressure states were estimated behind the Mach stem [41]. More measurements of Mach reflections using a similar experimental setup were made in plexiglas cylinders using a flash gap technique by Adadurov et al. [3, 2]. This method was later extended to mechanical impact testing [78], where composite cylinders were used to generate the converging shocks and subsequent Mach reflection, creating extreme compaction in recovery experiments. The composite method forms the basis of the Mach lens technique presented in the following section.

2.2.5.2 Mach Lens

A simple way to produce a useful Mach reflection is through the so-called Mach lens configuration shown in Figure 2.18. The composite Mach lens target assembly consists of an inner cylinder surrounded by a concentric outer cylinder. Upon impact, a plane shock is generated at the front of the target. The difference in material properties immediately results in a mismatch of wave speeds, and the materials are selected such that the shock speed in the outer cylinder is higher than in the inner material of interest. The impedance mismatch at the cylinder's interface produces conical shock waves which converge on the axis of the inner cylinder. It has been shown [18] that irregular reflection must always occur in conically convergent flow for a material with a normal equation of state. This has been observed in experiments where the conical analog of a Mach reflection has been observed using various loading techniques and diagnostics [41, 2, 78, 67, 68]. As shown, the Mach wave, which is analogous to that seen in gas dynamics, consists of the incident shock joining with the reflected shock and Mach stem. After forming, the length of the Mach stem wave will grow in size until it reaches a limiting diameter where the incident shock, which functions as a carrier of the pressure gradient between the interface and the Mach stem, reaches a minimum energy configuration. Once the Mach reflection reaches a steady state, the axial component of the velocity for every point of the Mach wave must have a velocity equal to the shock speed in the outer cylinder. Thus, at the center of the inner cylinder, where symmetry forces the Mach stem to be normal to the flow, the resulting Mach disk can be approximated as a plane wave traveling at a velocity equal to the shock speed in the outer cylinder. If the outer cylinder and the impactor materials are well characterized, a measurement of the projectile velocity and impedance matching can be used to calculate the shock velocity in the outer cylinder, and thus, the speed of the Mach wave. Further, if the Mach stem is assumed to act as a plane wave, a single measurement of the particle velocity is sufficient to calculate a Hugoniot state.

A final noteworthy feature of the Mach lens configuration is the pressure gradient associated with the Mach reflection. As will be shown in later sections, the magnitude of the shocked state in the inner cylinder varies radially. Further, the pressure must increase continuously and monotonically from the interface with the outer cylinder to the center of the inner cylinder. Since the axial velocity of the wave must be constant, a measurement of the reflection angles and a component of the particle velocity should result in a continuous measurement of the material Hugoniot between these two states [22].

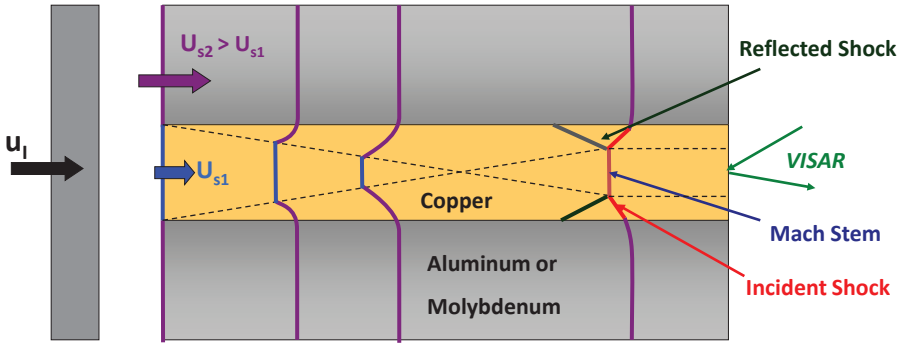

Figure 2.18: Mach lens target configuration. A plane shock is generated with a standard normal plate impact on the left.

2.2.5.3 Impedance Matching Solution

A rough estimate to the Mach reflection problem in the Mach lens configuration can be obtained through idealizing the problem as having the three distinct regimes shown in Figure 2.19(a). The first region is the far field shocked state 1 in the outer cylinder, and is simply determined by impedance matching (Figure 2.19(b)) between the impactor and the outer cylinder. The second region, state 2, is directly behind the Mach stem. Since the Mach reflection is assumed to be in a steady state, the velocity of the Mach stem is the same as the shock velocity calculated in state 1. Thus, as shown in Figure 2.19(c), the inner and outer material Hugoniots in $U_s - u_p$ space can be used by examining the line of constant shock velocity to solve for the particle velocity and completely characterize state 2. The third region of interest is the steady state reached between the two materials, well behind the Mach stem. The boundary between the two states can be characterized as a slip stream, or vorticity sheet, in the sense that mechanical equilibrium forces the traction forces to be equal, while allowing for discontinuities in the flow velocities and densities. Following a material point along the center of the inner cylinder, the material is expected to shock up to state 2 with the arrival of the Mach stem, then release down to the stress at the interface given by state 1. As the release is expected to occur via an expansion wave, the process can be assumed to be isentropic, meaning the solution is given by the intersection of the inner material release isentrope centered on shocked state 2 (Eqn. 2.8) with the isobar from state 1, as shown in Figure 2.19(c). As shown in the next section, this is a crude approximation that does not properly account for what happens at the interface, and should be limited in use to back-of-the-envelope type calculations.

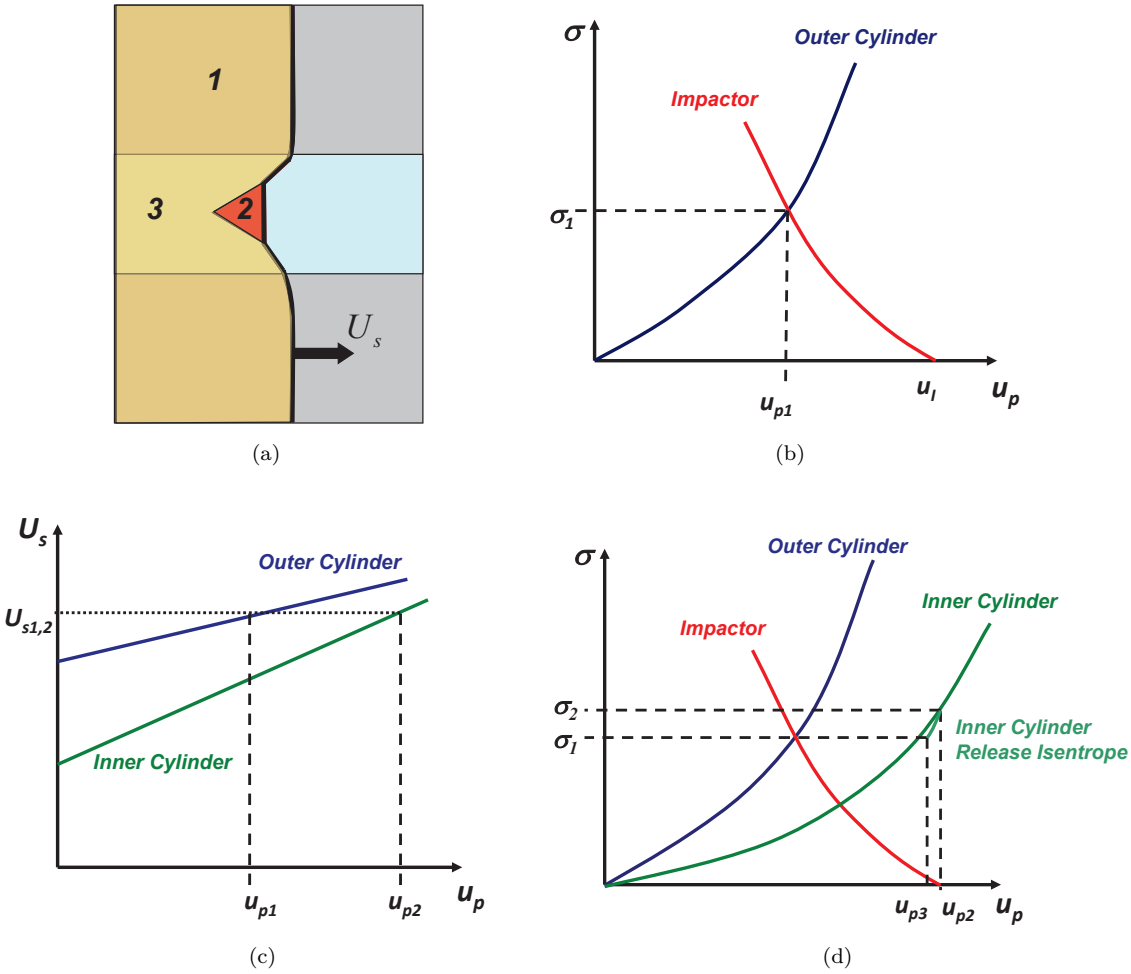

Figure 2.19: The three primary regions of interest in the Mach reflection in the composite cylinder configuration are shown in (a). The solutions for regions 1, 2, and 3 are shown in (b), (c), and (d), respectively.

2.2.5.4 Shock Polar Solution

The problem of a detonation wave interacting with a solid interface has been an area of recent interest, and the shock polar methodology has proven to be a useful tool in describing such interactions [9, 10]. The Mach lens results in a similar configuration between solid interfaces, and, as such, the same methodology can be applied here. The parameters of the Mach reflection shown in Figure 2.18 are shown in the steady reference frame of the Mach wave in Figure 2.21(a). Since the Mach wave is assumed to be steady, the axial velocity of the entire configuration is known from impedance matching as discussed in the previous section and is designated U_{s1}. In the Eulerian frame, this velocity becomes the upstream velocity, which is labeled q_1 in the oblique shock configuration (Figure 2.10). Neglecting any edge effects, the shock in the far field outer cylinder is simply a normal shock governed by typical normal plate impact conditions. Approaching the interface between the

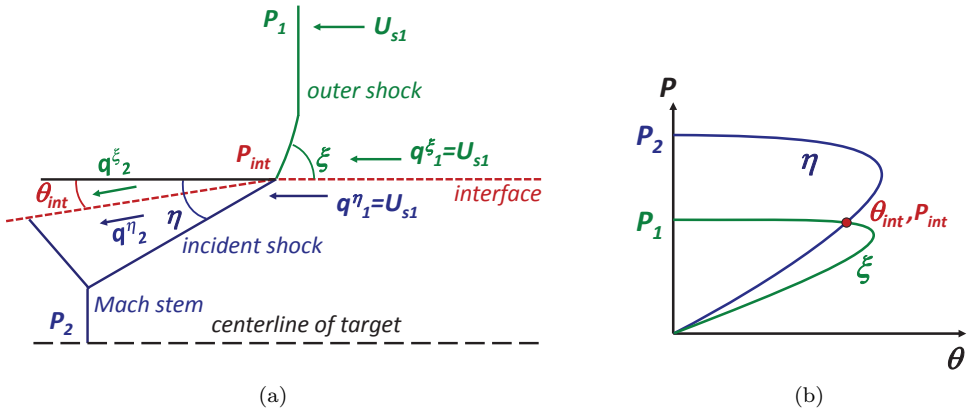

(a) (b)

Figure 2.20: Illustration of the strong shock polar analysis solution. The wave configuration and flow parameters (a) are shown along with an example of the intersecting shock polars (b).

inner and outer materials, however, the wave must diffract at the interface, as shown, to allow for a feasible solution. The angle this diffracted wave makes with the upstream flow is the oblique shock angle and is designated ξ . Thus, at the interface and in the outer material, the downstream state will have the flow properties P^{ξ}, θ^{ξ}, and q_2^{ξ} . The inner material is assumed to contain an ideal Mach reflection in which the incident reflection has a constant angle of obliquity, η, and connects to the Mach stem, which is normal to the upstream flow. The flow downstream of the incident shock contains the interface properties P^{η}, θ^{η}, and q_2^{η} . Once again, conservation of mass and momentum in this frame requires the pressure and the flow deflection on either side of the interface to be the same, and hence, $P^{\xi} = P^{\eta} = P_{int}$ and $\theta^{\xi} = \theta^{\eta} = \theta_{int}$. This solution is shown graphically in Figure 2.21(b) where the shock polar for the inner and outer materials are calculated through the material properties and upstream flow velocity with Eqn. 2.74. In this case the polars intersect and, borrowing from the detonation community [10], will be called a strong confinement solution.

A second solution type, deemed the weak solution, exists when the shock polars do not intersect. In this case, oblique shocks alone are not enough to turn the flow to an appropriate equilibrium. Additional turning of the flow can be accomplished through an expansion wave. It is assumed that the oblique shock will turn the flow as far as possible while remaining supersonic since an expansion cannot exist in the subsonic domain. Thus, an expansion wave can be constructed with Eqns. 2.82 and 2.83 from the sonic point of the shock polar. The intersection of this expansion with the inner shock polar, as illustrated in Figure 2.21, provides the necessary interface pressure and flow deflection for equilibrium.

Since the general behavior of the inner cylinder (Mach reflection) is independent of the confinement type, the properties of the reflected shock can be found once the interface state is known. As shown in Figure 2.4, the general role of a reflected shock is to rotate the deflected flow back to its original orientation. If this is assumed here, a reflected shock polar can be generated using the

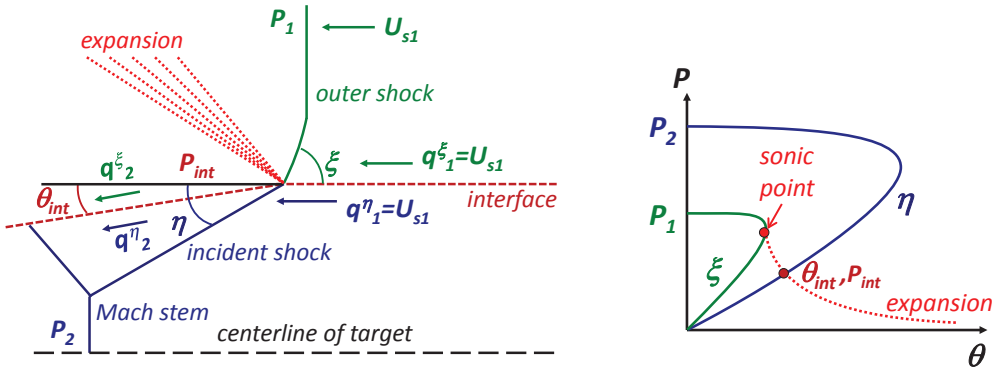

(a) (b)

Figure 2.21: Illustration of the strong shock polar analysis solution. The wave configuration and flow parameters (a) are shown along with an example of the non-intersecting shock polars requiring a polar for the expansion (b).

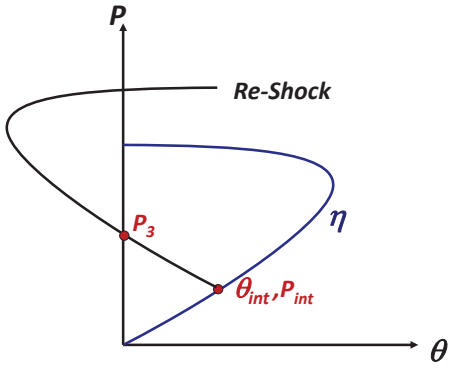

(a)

Figure 2.22: Illustration of the reflected shock solution. The reflected shock is assumed to bring the flow deflection back to $\theta = 0$.

re-shock Hugoniot generated with Eqn. 2.62, and, as shown in Figure 2.22, the intersection of this polar with $\theta = 0$ gives the reflected shock solution, P_3.

2.2.6 Phase Transitions

2.2.6.1 Background

Phase transitions are a critical feature in any complete description of the material behavior. Shock waves, in particular, provide a valuable tool for accessing the intricacies of high pressure, high temperature phase transitions. Theories on the mechanics, thermodynamics, and kinetics of these transitions have been the focus of a great deal of research [39]. In the simplistic summary presented here, the focus will be on first-order polymorphic or melting transitions. In general, the Hugoniot curve is not as simple as what has been idealized previously, such as that shown in Figure 2.8.

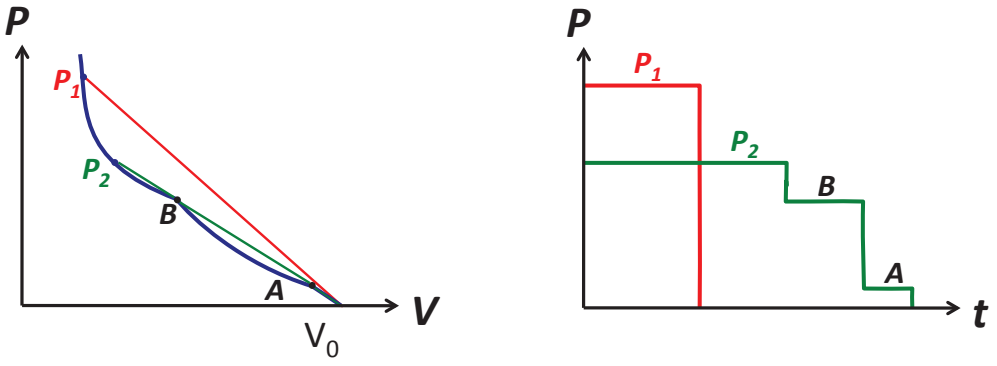

(a) (b)

Figure 2.23: Hugoniot curve in which the Hugoniot elastic limit is shown at point A, and a new phase forms at point B.

Instead, a real material will generally exhibit a Hugoniot such as the one represented in Figure 2.23(a), where the material reaches the Hugoniot elastic limit (HEL) at point A and begins to transition to a new phase starting at point B.

Properly measuring this type of Hugoniot, however, is complicated by the stability of the shock wave, where stability is defined by whether or not the shock wave will divide into multiple waves. Combining Eqns. 2.37 and 2.38, it is possible to relate the Rayleigh line, which is the chord connecting the initial and final states, to the shock speed.

$$\frac{U_s^2}{V_0^2} = \frac{P^+ - P^-}{V^- - V^+}, \tag{2.85}$$

Thus, shock stability can be determined by examining the slopes of the chords connecting the states of interest. Consider the possibility of jumping from an initial state (0), to an intermediate state (1), and finally to an end state (2). Assume the slope of the chords are such that the following inequality is satisfied:

$$\frac{P_2 - P_1}{V_1 - V_2} < \frac{P_1 - P_0}{V_0 - V_1}. \tag{2.86}$$

In this case, the higher pressure shock continually falls further behind the first shock and a two-shock system is stable. On the other hand, if the inequality is reversed, the high pressure shock is the fastest traveling wave in the system and overdrives everything else, such that only a single shock is observed.

Examples of these situations are given in Figure 2.23, where two final shock pressures are achieved. The first, higher pressure state, P_1, is achieved through the largest sloping Rayleigh line which directly connects the initial and final states. Thus, the expected wave profile in this situation is a single shock up to P_1. In considering a second state, which is associated with P_2, the Rayleigh

line connecting the initial and final states now lies below the alternative of using multiple Rayleigh lines. The multiple Rayleigh lines, plotted in Figure 2.23(a), have monotonically decreasing slopes as the pressure is increased. As a result, the multiple shock solution becomes stable, and results in the multi-shock profile shown in Figure 2.23(b). In this case, the transition pressures along the Hugoniot are directly related to each step in the wave profile. Generally, the Hugoniot elastic limit of most metals is small compared to the shock pressure, and is neglected when calculating principal Hugoniot points. This assumption, however, cannot be made for higher pressure transitions. This can make the behavior of the principal Hugoniot between phase transition states of this nature extremely difficult to determine.

2.2.6.2 Effect on Mach Lens Configuration

The types of phase transitions discussed above involve discontinuities in the shock speed of the material. This brings to light the question of how converging shocks, and, specifically, the waves in the Mach lens configuration are affected by a discontinuity of this nature. As discussed in the previous section, the Mach wave produces a continuous regime of shocked states between the interface and normal Mach stem pressures. As such, the configuration provides a sensitivity to phase transitions over a large range of pressures, which is lost with one dimensional plane shock waves. While the resulting reflections appear to be very complex and depend on the nature of the phase transition, numerical simulations suggest a steady state is reached and it may be possible to detect phase transitions that conventional methods currently struggle to measure. As will be shown in Chapter 4, a complicated wave structure can arise in which a phase transition wave precedes the Mach reflection. In this case, proper interpretation of the properties of the reflections can be used to gain insights into the nature of the transition. Further discussion of the exact nature of the reflections and behavior of a material containing a phase transition will be relegated to future chapters where specific examples are given in detail.

Chapter 3

Experimental Method

The experimental techniques used to examine the material behavior in the Mach lens configuration are presented in this chapter. The first section details the loading system used to launch projectiles to velocities on the order of 2 km/s. Two different systems were used, both of which utilize gun powder to provide the necessary force to achieve these high velocities. The systems are deemed the Caltech and Sandia powder guns. The second section provides the details on the diagnostic used to monitor the propagation of the shock waves through the target. The VISAR and ORVIS techniques utilize optical interferometry to provide high resolution velocity information and are the primary methods used to provide quantitative information. The third and final section provides details on the target configuration. The targets are designed to provide the means to study the configuration in both the strong and weak confinement regimes and are optimized to obtain a steady state Mach reflection. The logistics of how the target is used in conjunction with the loading system and the diagnostics are also presented.

3.1 High Velocity Planar Shock Loading System

3.1.1 Caltech Powder Gun

The powder gun, housed in the solid mechanics high-strain-rate laboratory of the Graduate Aerospace Laboratories (GALCIT) and shown in Figure 3.1, provides a loading system for the shock compression of solids. The gun is 3 m long, and has a bore diameter of 36 mm. When the gun is fired, a solenoid powered by a 120 V AC supply imparts linear momentum to a 4340 steel tapered trigger pin. The trigger pin is fit into a 1.8 mm diameter circular hole drilled 19 mm in depth to fit against the end of a charge assembly. The assembly consists of a rifle primer cartridge filled with 3 g of 2400 handgun powder. This cartridge slips inside a housing leading to a flame splitter surrounded by the main primary powder breech. The flame splitter is a hollow cylinder with 16 through-holes distributed in a 45° spiral. The powder breech has a 33 mm inner diameter and is generally filled

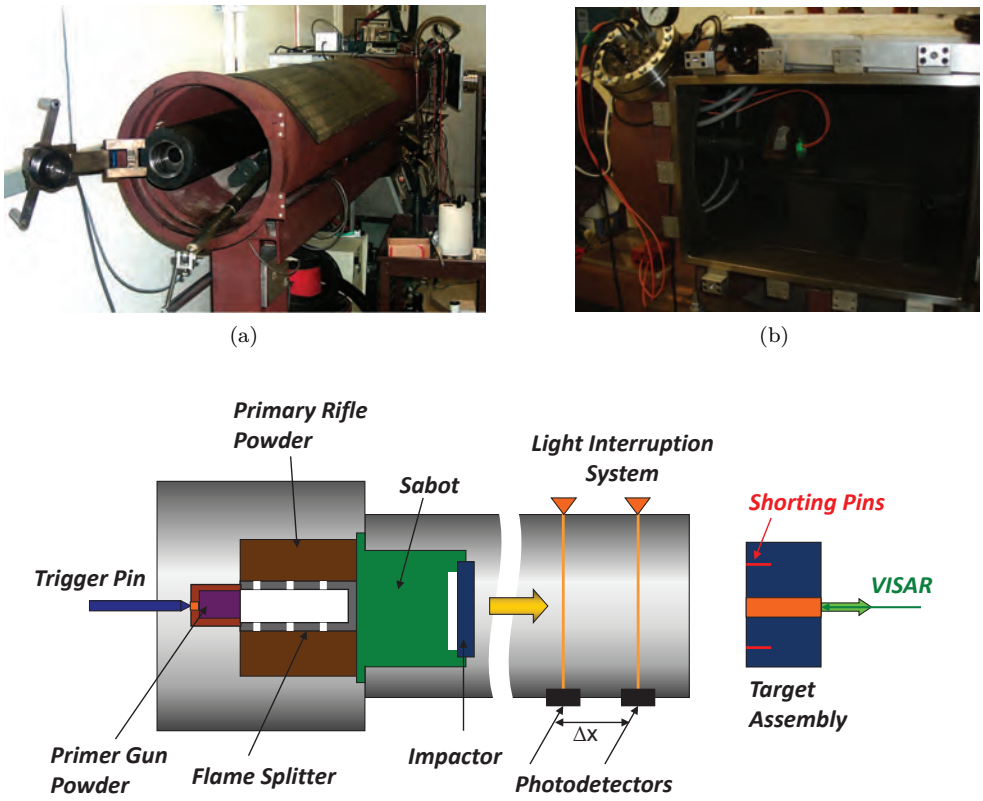

Figure 3.1: Caltech's powder gun system for shock loading of solids. The breech end of the gun barrel can be seen in (a) and a loaded target is visible in the target chamber in (b). A cartoon configuration of the system is shown in (c).

with up to 50 grams of H4198 rifle powder. The trigger pin is designed to indent the primer 0.6 to 0.8 mm, which provides enough pressure to initiate the primed cartridge which, in turn, detonates the initial powder. As the powder burns, a high temperature, high pressure flame rushes into the flame splitter, which provides an even ignition of the surrounding H4198 rifle primary powder. As the primary powder burns, a high pressure gas is formed in the breech which exerts considerable force on a polycarbonate sabot. The sabot, shown in Figure 3.2, is made of an engineering plastic, nylatron, and is designed to seal against both the launch tube and the charge assembly. As shown, there are several small steps that slowly increase the diameter of the sabot followed by a stop ring. This provides a tight fit into the launch tube while ensuring the sabot is fully seated once the stop ring is flush with the barrel. The breech end of the sabot contains an angled section followed by a planar surface, forcing the burning powder to provide a uniform load. The other (target) end is designed with multiple counterbores, which allows for an impactor of interest to be glued into the sabot while still maintaining an air gap between the impactor and the polycarbonate. This type of configuration provides a well characterized release wave to zero stress to be generated at the rear

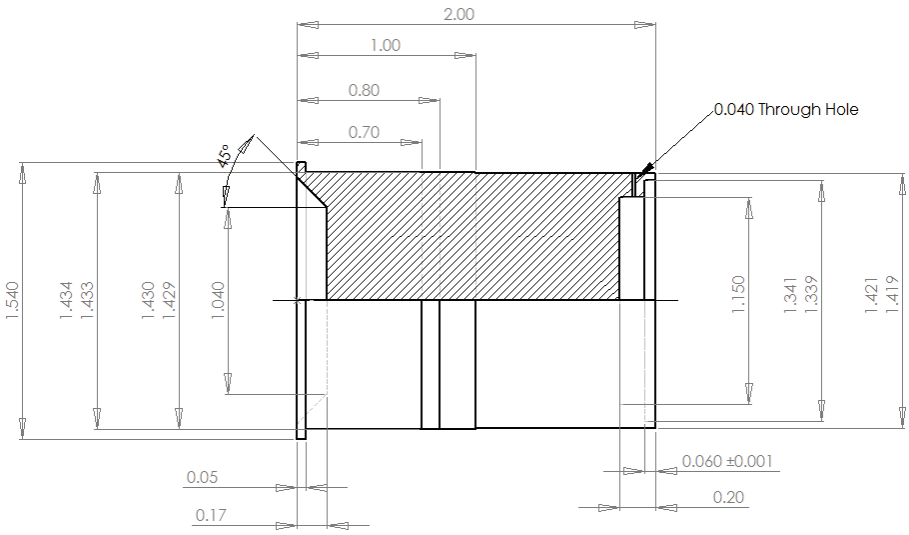

Figure 3.2: Drawing of the nylatron sabot (dimensions in inches).

surface, which can be of use in spallation experiments.

Upon firing, the sabot's stop ring breaks, and the gas accelerates the sabot down the launch tube and into a target assembly. Generally, the launch tube and vacuum chamber are brought to a medium vacuum of ~10^{-2} $torr$, though which velocities of 400-2000 m/s can be achieved. Under these conditions, the projectile velocity has been calibrated over the course of many shots, and can be predetermined by controlling the mass of the powder relative to the mass of the sabot. A plot of the recent shots performed is given in Figure 3.3, where the mass ratio of the powder used to the weight of the sabot should be linearly proportional to sabot velocity squared [28]. Since the velocity calibration only provides a rough prediction, the projectile velocity is determined experimentally by a light interruption system. This system attaches to the end of the launch tube and is called the barrel extension. As shown in Figure 3.1(b) and (c), the extension contains 2 fiber optic inputs on each side of the barrel and are separated by distance of 40.35 mm. An illuminator is used to run white light through two 3 mm fiber bundles, and after passing across the barrel, the light is collected with 2 identical bundles. The collected light is then conveyed to photodectors, which is connected to a triggering system. When the projectile blocks the first light beam, the detector senses the loss of light and a counter is started. Similarly, when the second beam is blocked, the timer is stopped. This provides the time it takes the projectile to travel the 40.35 mm gap, giving an estimate of the velocity. This system also serves as a useful fiducial for triggering the oscilloscopes that monitor other diagnostics used to characterize the propagation of the waves.

Alignment of the target is performed by using a series of adjustable mirrors to bring a low intensity laser source through the breech end of the barrel such that it is concentric with the launch tube. The laser is assumed to be concentric once the beam is adjusted to travel through two pinholes

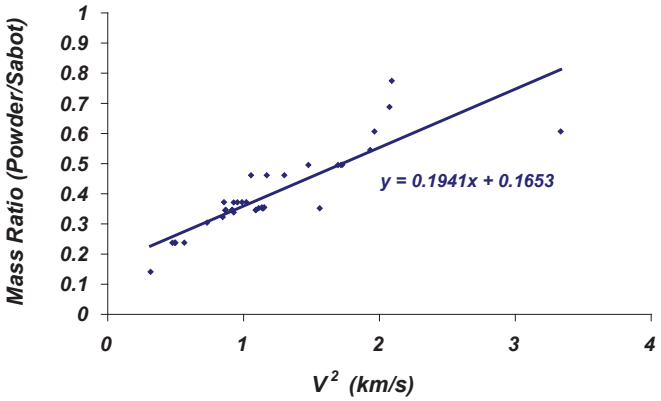

Figure 3.3: Velocity calibration relating the powder to projectile mass ratio to the square of the projectile velocity.

located between alignment rods fit into the breech and target ends of the launch tube. This laser source can now be used to not only center the target but also to adjust its angle of obliquity. Once the alignment laser is reflected from the front surface of the target back to its original source, the target is assumed to be normal to impact. In all of the experiments, the front of the target was located 32 *mm* from the end of the barrel extension, which leaves the rear quarter of the sabot in the barrel on impact. This should mitigate any effects of the projectile tilting, resulting in a normal impact if the target is aligned properly. In most of the experiments the tilt was less than 5 *mrad* (0.3°), and is assumed to be negligible.

3.1.2 Sandia Powder Gun

Several shots were conducted on the smooth bore powder gun at the Shock Thermodynamic Applied Research (STAR) facility at Sandia National Laboratories shown in Figure 3.4. The gun operates

(a) Powder gun located at the STAR facility

(b) Cartoon configuration of the impact

Figure 3.4: Sandia's powder gun system for shock loading of solids. The gun (a) is used to launch a projectile into the target assembly as shown in the cartoon configuration (b).

on the same principles as described previously, but on a much larger scale, and the details of this system are described elsewhere [8], hence, only a general overview will be discussed here. Velocities from 400 to 2200 m/s are achieved using an 89 mm bore diameter and 17 m long barrel. Phenolic projectiles carrying thick impactors were used to provide a well controlled step load without the possibility of a rear surface release wave playing a role in the experiment. The target assembly is mounted directly to the end of the barrel and, as shown in Figure 3.4(b), electric shorting pins of varying height are used to measure the projectile velocity. Alignment is performed by assuring the target assembly mount is normal to the barrel by aligning the mount with an optical flat. In these experiments, the tilt was even better, at a nominal value of ~ 3 $mrad$.

3.2 Diagnostics

A variety of techniques have been developed for measurement of plane waves of uniaxial strain. Early work was thoroughly reviewed by Graham and Asay [43], while more recent developments have been discussed by Chhabildas [25]. Early shock wave work, in the 1940s and 50s, focused on time of arrival estimates for Hugoniot measurements and used simple techniques such as electric shorting pins and flash gap measurements. In the 1960's there was a movement towards attempting to measure detailed aspects of the waveforms using in situ gauges. The electromagnetic particle velocity gauge was the first such development and is based on Faraday's law of induction in which an electromagnetic field is proportional to the motion of a conductor in a magnetic field. These types of gauges can be embedded at different thicknesses, and the use of Lagrangian wave analysis [5] allows for a determination of the stress-volume behavior. While these gauges are only suitable for materials that are not conductive at high stresses, they have been used to determine loading and release states in rocks, minerals, and window materials such as sapphire and fused silica. Perhaps the most effective use of this electromagnetic technique is in the study of the initiation and detonation of high explosives, where the run distance to detonation can be accurately measured using a series of gauges.

A short time later, piezoelectric and piezeoresistive techniques were developed to measure stress profiles. Piezoelectric gauges, such as the PVDF polymer film, still provide the best time resolution and best accuracy of the gauge techniques since the stress can be calculated directly through integration of the measured current across the gauge. Piezeoresistive gauges such as ytterbium, carbon, and manganin exhibit a change in resistance that is significantly more dependent on stress than temperature and, as such, a calibrated gauge can be used to measure a stress wave based on the measured gauge resistance. While the most obvious use of these stress gauges is to measure the longitudinal stress, a useful implementation is placing the gauge element parallel to the shock propagation direction. Such an orientation results in a measurement of the lateral stress, and given

uniaxial strain loading conditions, the strength of a material can then be determined by subtracting these components of stress. While measurements of this type are still somewhat popular, most gauges are limited to measuring stresses of up to$\sim$ 120 GPa, as most gauge insulating materials become partially conducting and result in significant inaccuracies in the gauge calibration.

While optical interferometry dates back to the late 19th century, it was the advent of the laser which allowed for the use of velocity interferometry in shock wave studies. Several velocity interferometers have been developed, but the velocity interferometer for any reflector (VISAR) is the most widely used in shock wave research. While the VISAR maintains the classic features of most interferometers in that it has extremely fast time resolution ($\sim$ 2 ns) , and no stress limitations, it has the added capability of measuring both diffuse and specular surfaces. Recent advances in oscilloscope response have also made displacement interferometry measurements at these velocities a possibility. In particular, commercial fiber optics have made all-fiber interferometers such as the photonic Doppler velocity (PDV) [77] an attractive alternative to the VISAR.

The geometry and materials chosen for current experiments makes the use of electromagnetic gauges impossible, and stress gauges very difficult. As will be shown, a single velocity measurement at the free surface is sufficient for Hugoniot measurements, hence, the primary diagnostic used will be VISAR. Additionally, shorting pins provide easy time detection capabilities and will also be used.

3.2.1 Electric Shorting Pins

The electric shorting pins are provided by Dynasen (CA-1038) and contain a 63.5 μm gap between a conductive outer casing and an insulated pin. On impact, the gap closes and the pin shorts, serving as an arrival time detector. These pins are used with a pin mixer giving a time resolution of ~ 3 ns [58], and can be used to estimate impactor velocity, shock velocity, and impactor tilt [85, 65]. The use of the pins will be limited to timing and tilt measurements in the Caltech experiments, and both impactor velocity and tilt in the Sandia shots. Tilt is estimated using four small equally spaced pins along constant radii glued such that they are flush with the front of the target. An estimate of the obliquity at impact can be obtained by [58]

$$\alpha = \frac{V_I C_I}{R}, \tag{3.1}$$

where α is a nominal scalar estimation of impactor tilt, V_I is the impactor velocity, R is the pin circle radius, and C_I is the center impact time given as the average of the pin arrival times adjusted such that the first pin hit provides the temporal fiducial. This measure of tilt is essentially the normalized average time it takes for the planar impactor to close from the first pin hit onto the center of the target. It should be noted that it is possible, with a minimum of three pins, to fit a plane surface to the arrival times using the impact velocity and obtain an accurate description of the azimuthal and

polar angles of obliquity. Most applications, however, only require an estimate of the center impact time, making Eqn. 3.1 a sufficient description of the impact tilt. Further, alignment procedures have reduced this measure of tilt to be on the order of milliradians, which is typical for this type of experimental system [65], and is generally negligible for most experimental measurements.

3.2.2 Velocity Interferometer System for Any Reflector (VISAR)

3.2.2.1 Basic Principles of Operation

The VISAR provides a point measurement of an interface velocity with high temporal resolution [13]. The basis of the velocity interferometer is the Doppler shift. If laser light is reflected off of the surface of the moving target, the reflected light will have an associated Doppler shift:

$$\lambda = \lambda_0 \left(1 - \frac{u}{c}\right), \tag{3.2}$$

where c is the speed of light, λ_0 is the incident laser wavelength, u is the velocity of the moving surface, and λ is the Doppler shifted wavelength. If a Doppler shifted beam with frequency ν_1 is combined with itself at a short time later, which now has frequency ν_2, the intensity of light can be expressed as

$$\begin{aligned} I &= |E_s|^2 = |A_1 cos\left(2\pi\nu_1 t + \phi_1\right) + A_2 cos\left(2\pi\nu_2 t + \phi_2\right)|^2 \\ &= A_1^2 cos^2\left(2\pi\nu_1 t + \phi_1\right) + A_2^2 cos^2\left(2\pi\nu_2 t + \phi_2\right) \\ &+ A_1 A_2 cos\left[2\pi\left(\nu_1 + \nu_2\right)t + \phi_1 - \phi_2\right] + A_1 A_2 cos\left[2\pi\left(\nu_1 - \nu_2\right)t + \phi_1 - \phi_2\right]. \end{aligned} \tag{3.3}$$

The first three terms oscillate at a frequency on the order of the laser light, 10^{14} to 10^{15} Hz, which is well out of the response range of oscilloscopes. The last term, however, is proportional to the so-called beat frequency, and is something that can be measured experimentally. Thus, the recorded intensity of the combined Doppler shifted light is representative of differential changes frequency, which can be related to differential changes in velocity, as seen in Equation 3.2. The VISAR, shown in Figure 3.5, is an optical system that forces this interference of the reflected light with itself after a known delay.

As shown in Figure 3.5, the reflected light is first sent into a 30/70 beam splitter where 30% of the light is sent directly to a photodetector and the rest is sent into the interferometer. This first photodetector is called the beam intensity monitor, and is used to correct for any changes in the reflected light intensity. The other 70% is sent into a 50/50 beam splitter where half is sent down a free path before being reflected back off of a mirror and combining with light from the second leg, which is sent through an 1/8 wave plate and length of etalon (a high index of refraction glass)

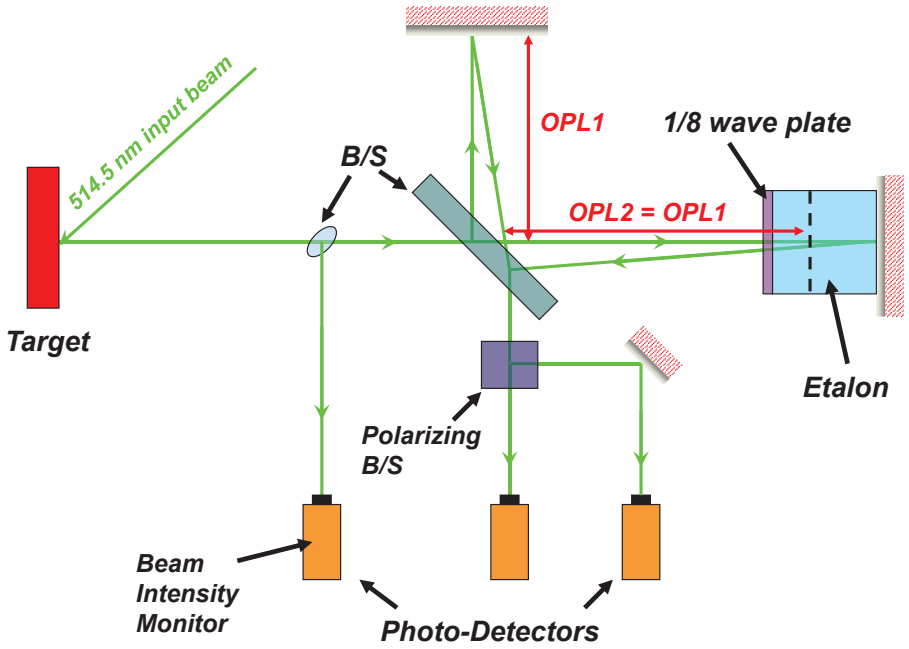

Figure 3.5: Schematic of VISAR

before being reflected by a mirror. The second leg is arranged such that its optical path length is the same as the first leg. The equivalent path lengths allow for optimal fringe contrast for any reflecting surface, since the divergence of the beams from a diffuse surface will be equal. Thus, the etalon makes it possible to maintain fringe contrast for diffuse surfaces while still providing the necessary time delay in the second leg. This clever arrangement is known as the wide-angle Michelson interferometer [49]. The second key idea of the VISAR is the utilization of Bouricius' method to produce quadrature phase components [21]. By introducing an effective 1/4 wave plate into the second leg (since the beam passes through the 1/8 wave plate twice), the P component of the laser light is retarded by 90°, changing the linearly polarized light to circular. When the combined beams are then sent into the polarizing beam splitter, the P and S components of the laser light are separated and then sent into two different photodetectors. The photodetectors, in turn, will record two sets of interferometry fringes that are 90° out of phase, and are said to be in quadrature. Quadrature is a key feature in this system because it allows for the detection of reversals, that is, acceleration to be distinguished from deceleration [13]. Hemsing's method of VISAR reduction [47] can be used to produce a continuous fringe count record. This is done by first subtracting out any fluctuations seen in the beam intensity monitor from the measured signals. Since the resulting signal takes the form of a sinusoidal function as shown in Eqn. 3.3, and one signal is exactly 90° out of phase with the other, the ratio of the two signals forms a tangent function. Thus, appropriately

unwrapping the tangent gives the fringe count

$$F(t) = tan^{-1}\left[\frac{s_2(t)}{s_1(t)}\right], \tag{3.4}$$

where

$$s_i = \frac{D_i(t)}{K_i} - \frac{B(t)}{K_0}, \tag{3.5}$$

and $D_i(t)$ is the measured light intensity of the photodetectors ($i = 1, 2$), $B(t)$ is the intensity at the beam intensity monitor, and K_i, K_0 are the appropriate normalization factors. All that remains is to relate the resulting fringe count, $F(t)$, to the interface velocity. The instantaneous number of fringes can be found be examining the difference in the total number of fringes in each leg, given by dividing the length of the etalon by the wavelength as

$$N(t)\,\lambda(t) = c\tau, \tag{3.6}$$

where τ is the known time delay due to the etalon. Differentiating Equation 3.6 with respect to time results in

$$\triangle N = -\frac{N}{\lambda}\triangle\lambda = -\frac{c\tau}{\lambda^2}\triangle\lambda. \tag{3.7}$$

Using Equation 3.2,

$$\triangle\lambda = \lambda_0\left(1 - \frac{2u}{c}\right) - \lambda_0 = \frac{-2u}{c}, \tag{3.8}$$

where the factor of 2 comes from the fact that the light traverses a round trip in the interferometer so the image velocity detected is actually twice that of the moving object [13, 30]. Substituting Eqn. 3.8 into 3.7 gives the velocity in terms of the fringe count:

$$u\left(t - \frac{\tau}{2}\right) = \frac{\lambda_0 F(t)}{2\tau}, \tag{3.9}$$

where $\triangle N$ has been replaced by F since the arrival of the shock can be chosen to correspond as the reference point for when the fringe record starts to change, and since the VISAR is only working as a displacement interferometer for an initial $\tau/2$ interval, the velocity is shifted to reflect this [30].

This type of simple VISAR setup has been constructed in the Caltech shock dynamics lab, and is shown in Figure 3.12. This VISAR was constructed in order to provide a wide range of interferometer delay times using etalon lengths of up to 350 mm, in 50 mm increments. The interferometer delay time is calculated by examining the difference in time it takes for light to travel each path of the

interferometer and results in the well known form of

$$\tau = \frac{2L}{c}\left(n - \frac{1}{n}\right), \tag{3.10}$$

where L is the length of the delaying medium, and n is its index of refraction.

3.2.2.2 VISAR Correction Factors

It has been shown that correction factors for Eqn. 3.9 are necessary to account for dispersion in the etalon [15], and dispersion in a window material if it used [12]. Dispersion in the etalon is caused by the dependency of index of refraction on the wavelength of laser light. As such, the time dependence of index of refraction must be examined. The number of fringes in each leg can be written as

$$\begin{aligned} N_1(t) &= \tfrac{2L_1}{\lambda(t)}, \\ N_2(t) &= 2\left(\tfrac{L_2 - L_E}{\lambda(t)} + n(t)\,\tfrac{L_E}{\lambda(t)}\right), \end{aligned} \tag{3.11}$$

where L_1, L_2 , L_E are the lengths of the first leg, second leg, and the etalon, respectively. Setting the initial optical path lengths to be the same

$$L_2 = L_1 + L_E\left(1 - \frac{1}{n_0}\right), \tag{3.12}$$

yields an equation for the difference in fringes

$$N(t) = N_2 - N_1 = 2\frac{L_E}{\lambda(t)}\left(n(t) - \frac{1}{n_0}\right). \tag{3.13}$$

The fringe count can now be calculated as

$$F(t) = N(t) - N_0 = 2L_E\left[\frac{1}{\lambda(t)}\left(n(t) - \frac{1}{n_0}\right) - \frac{1}{\lambda_0}\left(n_0 - \frac{1}{n_0}\right)\right]. \tag{3.14}$$

Taking the second-order expansion of the index of refraction

$$n(t) \approx n_0 + \left.\frac{dn}{d\lambda}\right|_{\lambda_0}, \tag{3.15}$$

and again substituting in the Doppler shift, Eqn. 3.2, gives

$$F(t) = \frac{2}{\lambda_0}u(t)\left\{\frac{2L_E}{c}\left(n_0 - \frac{1}{n_0}\right)\right\}\left\{1 - \left(\frac{n_0}{n_0^2 - 1}\right)\lambda_0\left.\frac{dn}{d\lambda}\right|_{\lambda_0}\right\}. \tag{3.16}$$

Noting that the first term in the brackets is simply the time delay in the etalon, τ , and writing

the second term in the brackets as a correction factor based on the initial wavelength of light, δ gives a corrected form of the velocity-fringe relationship:

$$V\left(t-\frac{\tau}{2}\right)=\frac{\lambda_0 F\left(t\right)}{2\tau\left(1+\delta\right)}. \tag{3.17}$$

For etalon, and laser light with $\lambda_0 = 514.5$ nm, δ is given in the literature as 0.0339 [15]. A similar correction can be made for dispersion in a window material, but as it is not relevant in these experiments, this will not be discussed further.

3.2.2.3 Push-Pull VISAR Modification

As discussed previously, after appropriate normalization, the two measured signals from the velocity interferometer, s_1 and s_2, can be expressed as

$$\begin{aligned} s_1 &= A_1 A_2 cos\left[2\pi\left(\triangle\nu\right)t+\nabla\phi\right], \\ s_2 &= A_1 A_2 cos\left[2\pi\left(\triangle\nu\right)t+\nabla\phi-\tfrac{\pi}{2}\right]=A_1 A_2 sin\left[2\pi\left(\triangle\nu\right)t+\nabla\phi\right]. \end{aligned} \tag{3.18}$$

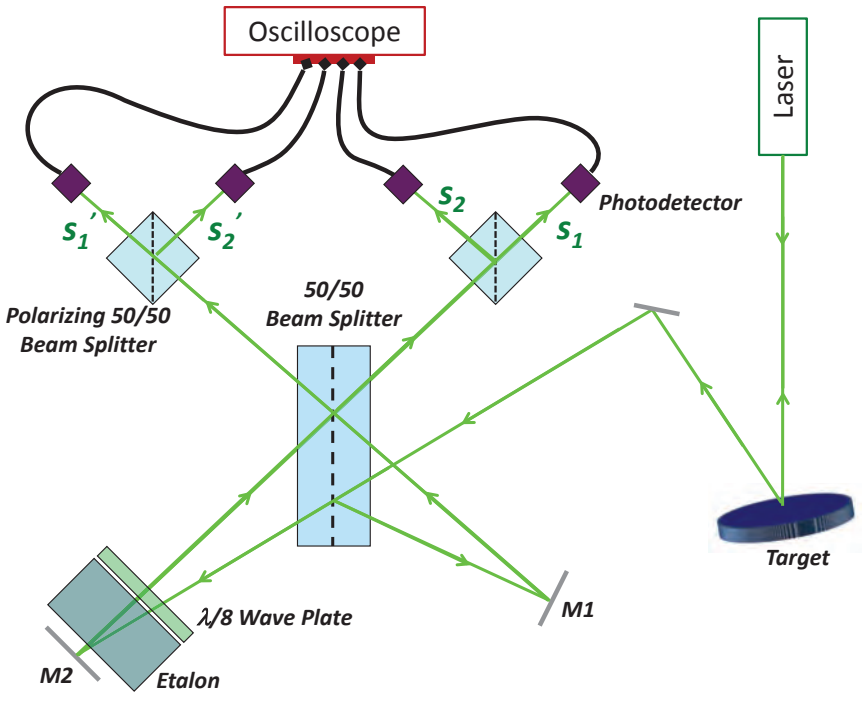

Figure 3.6: Schematic of push-pull VISAR.

Examining Figure 3.5, it can be seen that after the reflected beams from legs 1 and 2 are mixed in the beam splitter, only half of this light (that used in transmission) is actually collected and sent into the photodetectors. The other half of the light (that in reflection) is essentially thrown away. If this light is collected, and similarly sent into a polarizing beam splitter and then two photodetectors, what is measured are the complements of the signals $s_1^{'}$ and $s_2^{'}$, where

$$\begin{aligned} s_1^{'} &= A_1 A_2 cos\left[2\pi\left(\triangle\nu\right)t + \nabla\phi + \pi\right] = -s_1, \\ s_2^{'} &= A_1 A_2 sin\left[2\pi\left(\triangle\nu\right)t + \nabla\phi + \pi\right] = -s_2. \end{aligned} \tag{3.19}$$

It can be seen in Eqn. 3.19 that by subtracting the signal from the complement, the resulting signal is doubled in amplitude. Additionally, any noise from incoherent light is canceled in this subtraction [47], giving the instrument much better resolution. The subtraction is often done electronically with differential amplifiers prior to being collected by the oscilloscope but can also be done in post-processing of the data.

3.2.2.4 Dual-Delay Interferometers

There is lack of uniqueness associated with the inverse tangent function, Eqn. 3.4, since adding $n\pi$, where n is an integer, results in the same solution. For smooth solutions, such as ramp waves, this is not a problem because the velocity profile must be continuous and the tangent function can be unwrapped properly. With shock waves, however, it is not always possible to resolve the structure of the wave, and it is likely that fringe jumps must be added at the point of the discontinuity to obtain the correct solution. In practice, an educated guess can often be made as to what the correct velocity is, so this problem is often ignored. To avoid any problems with biasing the waveforms in these validation experiments, however, it is possible to use the dual-delay technique [40] to obtain a completely unique solution. The idea is simply to split the collected light into two different VISAR systems of varying fringe constants. Thus, when the reduced velocity from each system is equal, the correct number of fringes for each analysis has been accounted for. Mathematically this can be written as

$$u\left(t - \frac{\tau}{2}\right) = \frac{\lambda_0}{2\tau_1}\left[tan^{-1}\left(\frac{s_2\left(t\right)}{s_1\left(t\right)}\right) + H_1\left(t_s\right)\pi\right] = \frac{\lambda_0}{2\tau_2}\left[tan^{-1}\left(\frac{s_2\left(t\right)}{s_1\left(t\right)}\right) + H_2\left(t_s\right)\pi\right], \tag{3.20}$$

where $H_1\left(t\right)$ and $H_2\left(t\right)$ are the integer valued Heaviside step functions that account for the necessary fringe jumps in the shock, which occur at time t_s. As will be discussed in Appendix A, it is desirable

to have one interferometer set at a high sensitivity and one at a low sensitivity. Further, the sensitivities should be an irrational ratio, such that fringe additions cannot coincidentally arrive at an incorrect velocity.

3.2.3 Optically Recording Velocity Interferometer System (ORVIS)

The ORVIS [20] was originally developed as an alternative to the VISAR to measure particle velocity histories, and uses a high speed electronic streak camera rather than photodetectors and an oscilloscope to measure the interferometers fringe motion. At the time, streak cameras had much faster time resolution capabilities (20 ps), which offered an improvement of 2 orders of magnitude over other measurement techniques. This is still a common trend where the commercial detectors and oscilloscopes used typically reduce the time resolution to around 2 ns. For most applications this is sufficient, and as such, the ORVIS is not nearly as commonly used in the shock physics community. However, the other advantage of the ORVIS is that there is an inherent spatial resolution since a streak camera is used. Thus, for applications where spatial heterogeneities are important, the ORVIS becomes an attractive option to use. In particular, this diagnostic seems ideal for use with the Mach wave configuration because of the inherent velocity gradients associated with the spatial orientation of the Mach wave. A schematic of a typical ORVIS configuration is shown in Figure 3.7.

As expected, the design of the interferometer is the same as for the VISAR, but the ORVIS makes use of a different fringe counting scheme. The technique makes use of equally spaced spatial interference fringes, which are formed by the intentional misalignment (in one plane) of the two interfering beams, as shown in Figure 3.7(b). The spacing of these fringes, d , then, is related to the angle of the misalignment, α, as

$$sin\alpha = \frac{\lambda_0}{d}. \tag{3.21}$$

In creating the misalignment, however, the interferometer has moved away from the optimum fringe contrast. As such, the mirror in the second leg (M2) must be moved parallel to the beam splitter to maintain a constant angle between the beams (β) until the fringe contrast is once again optimized. Verification of the correct position is either done using white light, or more often, a diffuse reflecting surface on the target. The delay time of the second leg must now be calculated to account for this adjustment. Assuming small angle approximations on α and β, geometry will show that the new delay time can be written as the previous delay discussed in Eqn. 3.16 with a correction factor associated with the length change

$$\tau' = \tau - \tau_c = \frac{2L_E}{c}\left(n_0 - \frac{1}{n_0}\right) - \frac{2}{c}\frac{\alpha}{\beta}H, \tag{3.22}$$

where H is the projected length of the mirror to the point of interference, as shown in Figure 3.7(a).

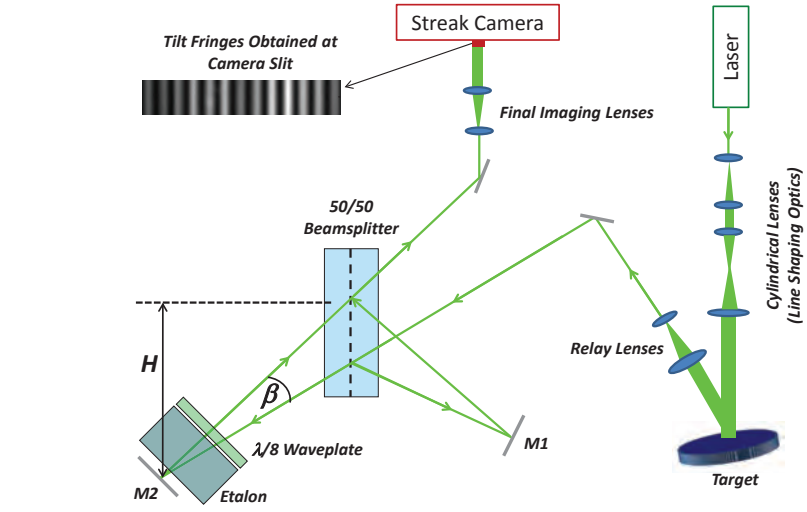

(a)

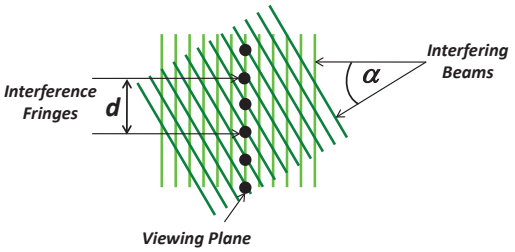

(b)

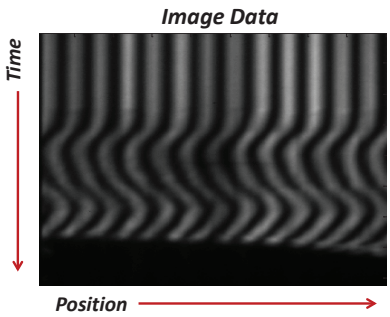

(c)

Figure 3.7: The ORVIS optical layout (a) makes use of cylindrical optics to shape a line on the target. The reflected light is collected and relayed through a standard VISAR interferometer, and the resulting interference pattern is imaged on the streak camera. The interferometer is misaligned as shown in (b) such that tilt fringes are obtained. The resulting fringe motion in an experiment (c) is proportional to the velocity of the imaged line. In this example, a planar impact of a quartz target results in a ramp wave.

It should be noted that the ORVIS fringe constant no longer only depends on the length of the etalon, but on the geometry of the mirrors and the tilt fringe misalignment. While errors are increased in measuring these values, it also allows a finer tuning of the interferometer sensitivity.

Once the time delay is known, Eqn. 3.17 can be used to calculate the velocity at each line-out in space. This is done by using the spatial interference pattern to create a pseudo-push-pull analysis. Since the spatial fringes form a so-called carrier frequency associated with d, line-outs can be taken in space at intervals of one quarter of this frequency. Since each of these four line-outs will be 90° out of phase with the next, this essentially forms the four signals associated with the push-pull method: s_1, $s_1^{'}$, s_2, and $s_2^{'}$, and the standard push-pull analysis applies.

3.3 Target Configuration

3.3.1 Materials

3.3.1.1 Single-Phase Materials

With the only requirement in the proposed Mach lens experiments (Section 2.2.5) being a higher initial shock speed in the outer material, a wide range of material combinations is available. Since the behavior of most metals can be described by classic plasticity models under shock compression [81], and to avoid any manufacturing and assembly issues with brittle materials such as ceramics, the initial validation experiments were conducted using well characterized metals. Further, for the initial validation experiments, any complications due to multiple phases were avoided. Over the range of shock stresses expected in these experiments, no materials with a known high pressure phase transition were used.

Copper was selected as the inner material of interest because its properties under shock compression are well known [62, 69, 66], the strength is low [46], the impedance can easily be bracketed by other materials, and it has been shown to produce steady Mach waves in a similar explosive configuration [41]. Outer materials can be chosen through impedance matching to determine which well characterized metals have a significant velocity increase, for which only a few realistic possibilities exist. The Hugoniots for these metals - beryllium, aluminum, titanium, molybdenum, and cobalt - are shown along with copper in Figure 3.8. While beryllium is an obvious choice for significant gains in this system, the hazards associated with it, particularly in these types of experiments, make it impractical. Aluminum has the next highest wave speed and since it is common, easy to machine, and has been thoroughly studied in the shock community, it was chosen as the ideal material for use in the validation experiments. Of course, the overall response of the system cannot be simply characterized by the $U_s - u_p$ relationship, as illustrated in the $\sigma - u_p$ diagram. Higher impedance materials such as molybdenum result in a much higher stress state in the outer cylinder, which, as illustrated in Section 2.2.5, results in a very different overall response. As such, molybdenum was selected as an ideal high impedance material to study along side the lower impedance aluminum and examine the effects of both strong and weak confinement, respectively.

A summary of the gains expected in each system is shown in Figure 3.9, in which the impactor is assumed to be copper traveling at 2 km/s. For a conventional plate impact experiment, the symmetric impact results in a particle velocity of 1 km/s, which relates to a pressure of nearly 50 GPa. The use of the Mach lens configuration with a molybdenum outer cylinder extends the Hugoniot to about 85 GPa, while an aluminum outer cylinder extends the Hugoniot to a particle velocity of 2.2 km/s and a pressure of over 140 GPa, more than doubling the range accessible to the gun.

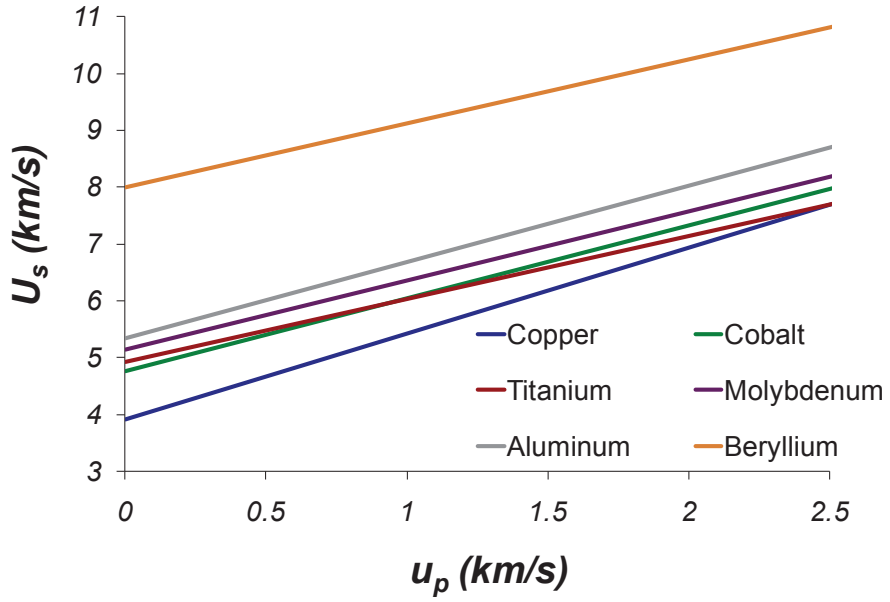

(a)

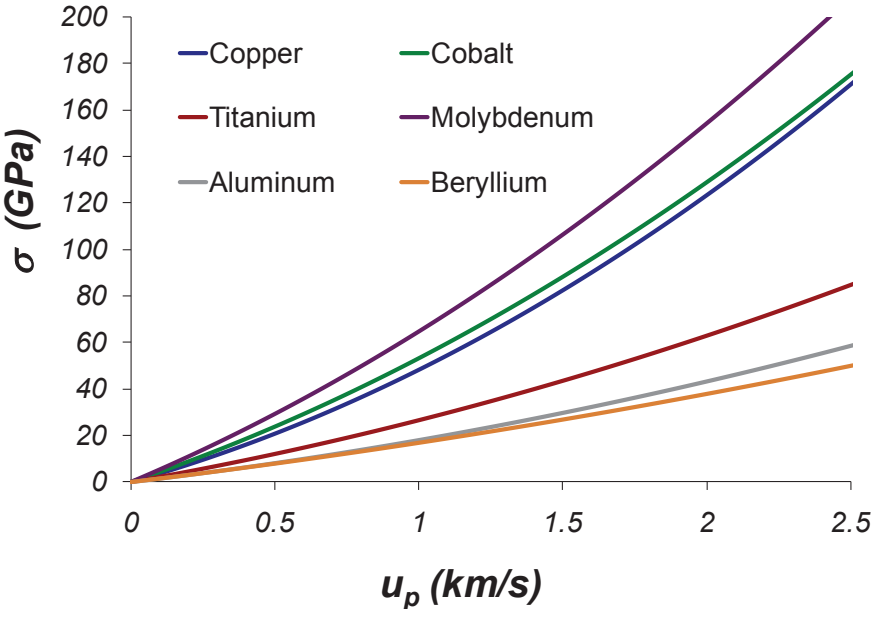

(b)

Figure 3.8: Hugoniots for metals with a higher shock velocity than copper.

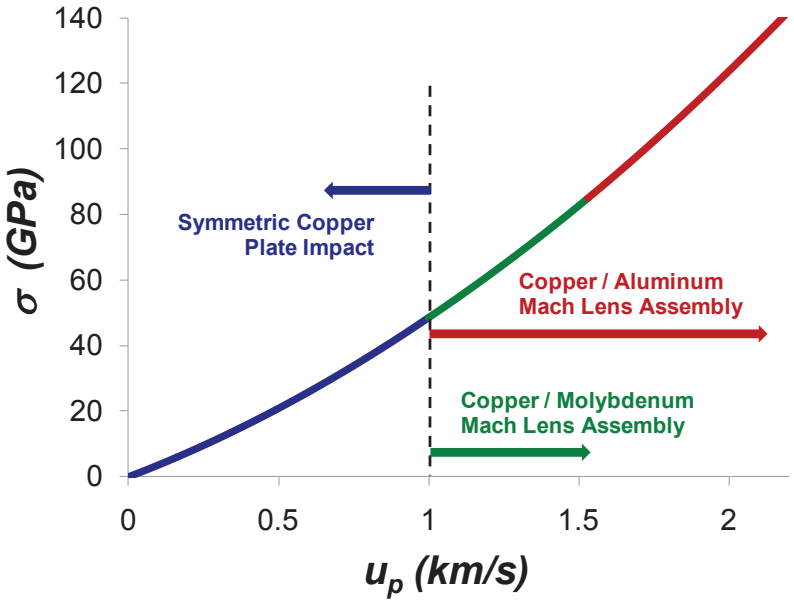

Figure 3.9: Range of the Hugoniot accessible in a copper target using a conventional plate impact technique compared with aluminum and molybdenum Mach lens configurations for a 2 km/s copper impact.

Oxygen-free high-conductivity (OFHC) copper rods with a purity of 99.99%, and the most commonly studied aluminum alloy, 6061, with nominal densities of 8.941 g/cc and 2.712 g/cc were supplied by McMaster-Carr. The molybdenum was supplied by National Electric Alloys and was rated at a purity of 99.95% resulting in a nominal density of 10.218 g/cc. The Mach lens assembly was constructed starting with the stock copper rod being cut to a length of 0.01" longer than the outer material thickness. The outer material was then cut from a stock plate and the diameter of the inner cylinder was reamed to be $\sim$ 0.002" smaller than the copper diameter. Freezing and heating the samples was not found to have a significant effect at the dimensions used, so the inner cylinder was simply press fit into the outer cylinder using a hand press with a small amount of low viscosity epoxy to minimize any gaps in the system. A symmetric length of copper was left extruding from each end of the target. This process usually resulted in a small amount of copper being shaved off of the diameter as it was fit, indicating excellent contact between the two materials. The epoxy used was a combination of EPIKURE 3140 curing agent with EPON 815C resin, which is commonly used for stress gauges and has a curing time of 24 hours. Once the epoxy cured, both sides of the target were sanded to remove the excess glue and extruding copper, then polished to achieve a flat and uniform impact and rear surfaces. Under some circumstances the target plates at this point were found to have a slightly uneven surface, in which case both sides of the target were also lapped to provide flatness and parallelism to 1/10. The impact surface was polished to a specular finish for alignment purposes, and the rear surface was typically sanded to a diffuse finish for reasons discussed

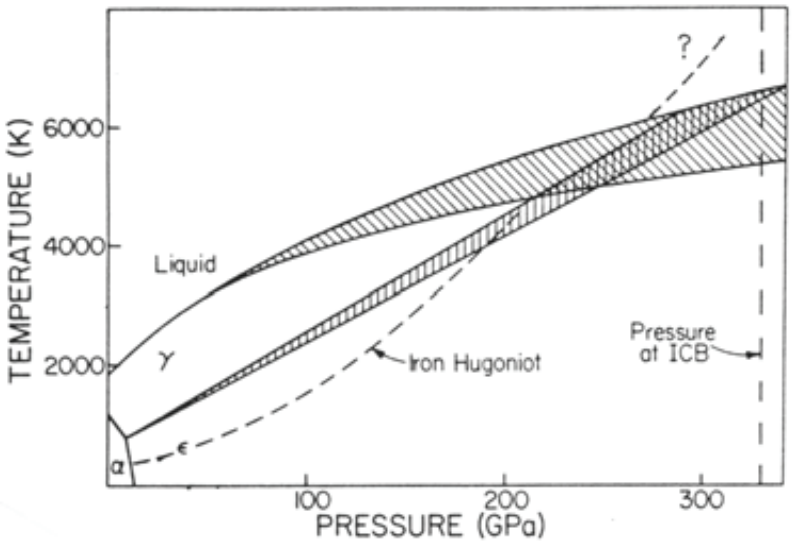

Figure 3.10: Phase diagram for pure iron [23].

in the next section.

The dimensions of the target were designed such that it would be long enough to support a steady state Mach wave while ensuring the edge release waves emanating from the outer surface do not interfere with the measurement. A back-of-the-envelope calculation can be made by taking a target length of 5 times the inner cylinder diameter and using the bulk release wave speed of the outer material in the shocked state to estimate the arrival time of the edge effects. For convenience, stock rod diameters were used, meaning the design space was limited to 1/16" increments in the diameter. Overall dimensions were refined using the numerical simulations discussed in Chapter 4 to ensure the design criteria were met. The dimensions of the experiments are given in Tables 5.1 and 5.3.

3.3.1.2 Iron

To examine the effect of a well known phase transition on the Mach lens system, iron was used as an inner cylinder in conjunction with the same aluminum and molybdenum outer cylinders. Iron rod with a purity of 99.95% was obtained from Goodfellow, and the same procedure described previously was used to assemble the targets. Its importance to industry and geology makes iron one of the most well researched materials by the shock community [24, 14, 4, 11, 83, 39]. An illustration of the phase diagram proposed by Brown and McQueen [23] is shown in Figure 3.10. At higher pressures ($\sim 200\ GPa$) the shock response of the material becomes extremely complicated as it transitions through mixed phase solid-solid and solid-liquid regions before fully melting around 250 GPa. At lower pressures, however, a well defined polymorphic phase transition also exists in which the initial bcc crystal structure, or α phase, transforms to the hcp, or ϵ phase. Precise measurements of the shock

wave profiles in plate impact experiments using VISAR [14] have been used to determine that this transition occurs under shock loading at 13 GPa. The corresponding shock and free surface particle velocities associated with this transition are 5.07 km/s and 0.64 km/s [14], respectively. Since the shock response for iron is very similar to that of copper, any changes in the system response are expected to be primarily due to this phase transition.

3.3.2 Single-Point VISAR

All of the experiments performed at Caltech utilized a single VISAR probe monitoring the rear surface of the center of the target. The target assembly used in these experiments is shown in Figure 3.11. Due to limitations in the diameter of the gun, holes for the tilt pins are drilled directly into the target, as shown in the front view of the target. The pins are located along a 25.4 mm bolt circle diameter and the hole diameter of 1 mm is expected to have a negligible effect on the overall response of the system. The target is glued into a polycarbonate support that contains three equally spaced holes along a 70 mm diameter that allows it to be attached to a steel mounting fixture. The target support is mounted to the fixture using spring loaded bolts such that the target can be aligned to be normal to the launch tube by adjusting the tension on each bolt. The target assembly is then fit into a V-block mounted in the tank with C-clamps, and can now be aligned for a normal impact. The center impact time, used in Eqn. 3.1, is taken to be time of impact to which all experimental data is correlated.

Two generations of experiments were performed that use slightly different systems. In the first generation, a basic VISAR system built for previous studies [85], and shown in Figure 3.12, was used. This VISAR system contains an adjustable length of etalon, allowing for a variety of fringe

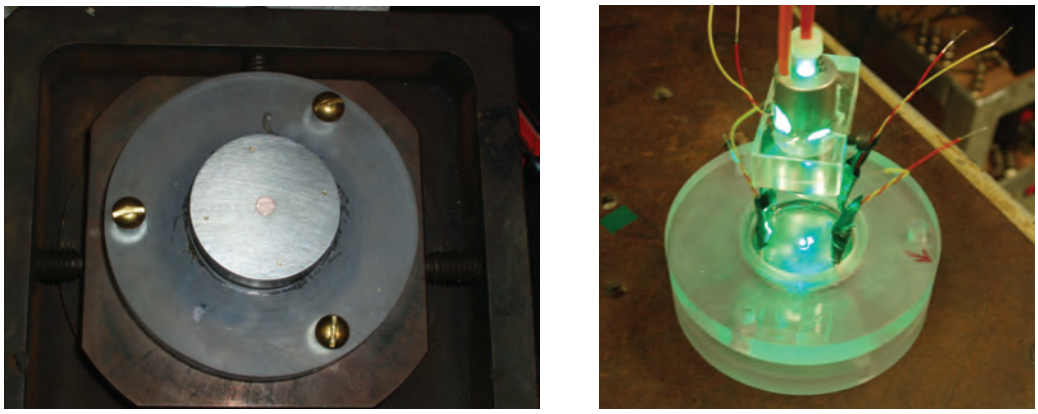

(a) (b)

Figure 3.11: Mach lens target assembly at the Caltech facility. The front of the target in the mounting fixture is shown in (a). A probe is used to focus and collect light for the VISAR system in (b).

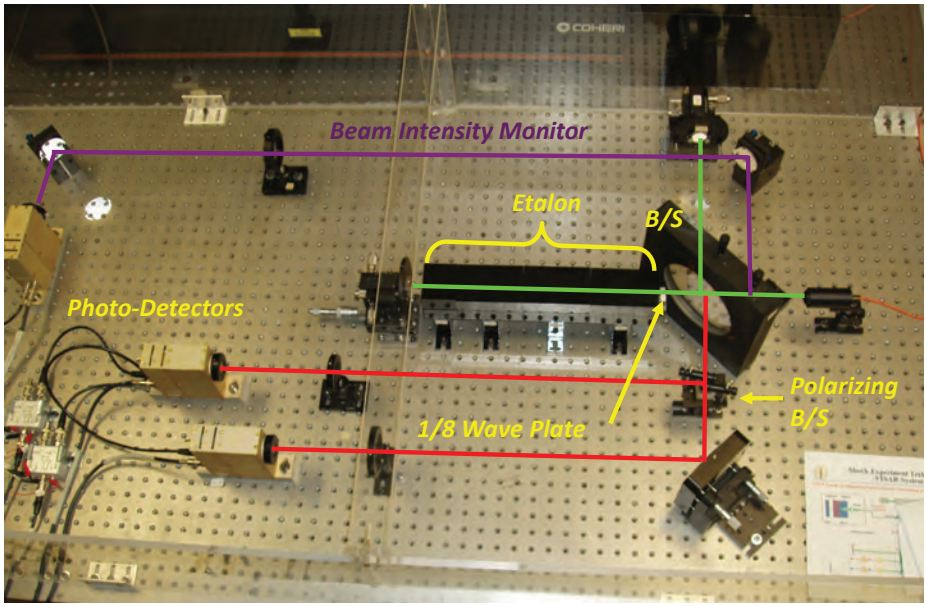

Figure 3.12: VISAR system constructed in GALCIT's shock wave laboratory.

constants to be used. Table 3.1 summarizes the parameters of this VISAR system, including the fringe constant, K, where $K = \frac{\lambda_0}{2\tau}$.

For the experiments conducted, free surface velocities from 1.5 km/s to 3.5 km/s are expected. A 50 mm etalon thickness was used, which, after calibration and application of the dispersion correction (Eqn. 3.17), resulted in a fringe constant of 580 $m/s/f$. This setup provides the necessary sensitivity ($\sim$ three fringes) at the lowest velocities while maintaining enough contrast to add fringes to the correct velocity. On the rear of the target, the probe assembly, shown in Figure 3.11(b), is used to focus and align the VISAR laser light. The probes were supplied by VAYLN V.I.P and contain a 50 μm single-mode fiber to transmit light from the laser to the target. The light source is a Coherent Innova 300C Argon ion 1 W laser operating at 514.5 nm. The probe lens has a 30 mm focal length, which focuses the beam to a spot size that is on the order of 50 μm. A collection lens then focuses the reflected light into a 300 μm multi-mode return fiber that is sent into the interferometer. As shown in Figure 3.12(b), the probe mount contains a set screw for setting the focal length, which is adjusted by returning an optimum amount of light from the center of target. Using this arrangement, about 5% of the incident light is collected from a diffuse surface which is sufficient for use with photomultiplier tubes used to detect the light. Because these experiments cannot utilize a window, an initially diffuse surface was employed since the arrival of the shock is expected to turn an initially specular polish diffuse anyway. In the few experiments conducted with a specular surface, it was extremely difficult to maintain fringe contrast.

Problems with the accuracy of the probe location and uncertainties in the fringe jumps led to a second experimental configuration. For these experiments, a so-called mini-VISAR system

Table 3.1: Delay parameters for GALCIT's open beam VISAR system.

Optical Component	Material	n	Thickness (mm)	τ (ns)	K (m/s)
1/8 wave plate	quartz	1.5525	3.81	0.0231	11495
			50	0.437	588.18
			100	0.852	302.06
			150	1.266	203.21
Etalon	SF11 glass	1.7988	200	1.680	154.10
			250	2.095	122.82
			300	2.509	102.54
			350	2.923	88.00

constructed by National Securities Laboratories was used. These systems, pictured in Figure 3.13, utilize the push-pull modification and a clever system of lenses rather than glass to produce the virtual delay. This results in an extremely compact and efficient system at the cost of a fixing the fringe constant. At 514.5 nm laser light, the fringe constant for this VISAR is 515.62 $m/s/f$. The four mixed light signals were monitored with the same photomultiplier units used in the basic VISAR. The detectors have a 1 ns rise time and a sensitivity of $\sim$ 5 A/W. The complementary push-pull signals are then combined in a 10x differential amplifier where they are subtracted and then sent to the oscilloscope.

The two interferometers allow for a dual-delay setup, addressing any problems with fringe uncertainties. To improve accuracies in the probe location and simplify the experimental setup, a bare fiber probe from RoMach, Inc. was used. These probes utilize the same input and output fibers except they are glued side by side directly into a 0.9 mm ferrule. A Plexiglas fixture with a hole diameter matching the ferrule size was then used to hold the bare fiber probe in place, as pictured in Figure 3.14. The target fixture contains small counter bores with diameters matching the target and probe holder. This allows the target and holder to be as concentric as possible and eliminates many of the errors involved in trying to center a focusing probe. Since radial adjustments are eliminated, only the stand-off distance requires tuning. The probe was glued in place such that interferometer contrast was optimized, which was typically at a standoff of $\sim$ 3 mm . Generally, in these experiments, the interferometer was found to lose contrast prior to free surface impact with the probe, hence the the short stand-off distance was not a problem.

The VISAR data was recorded on a 1 GHz Textronix TDS 7104 digital oscilloscope, which is

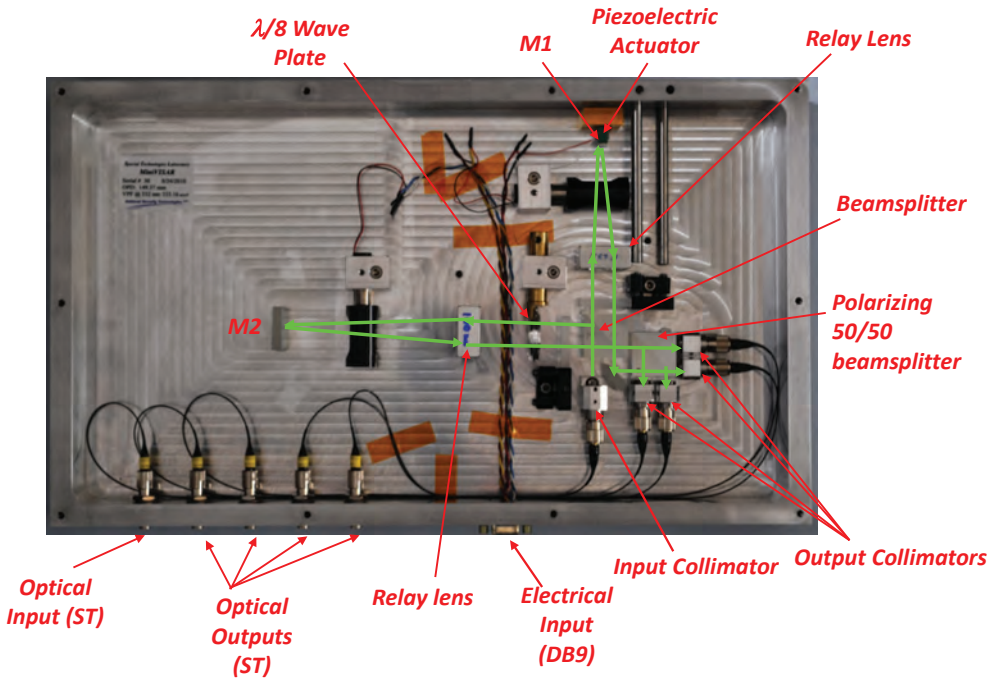

Figure 3.13: Schematic of mini-VISAR.

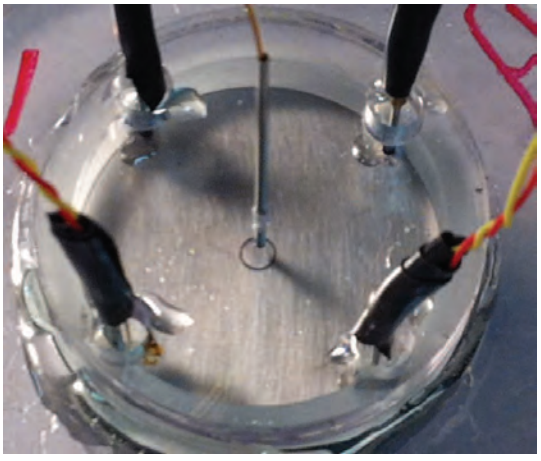

Figure 3.14: Rear surface of the Mach lens target assembly utilizing the bare fiber probe. The four tilt pins are also shown.

more than sufficient as the overall response of the interferometer is limited by the 1 ns rise time of the photodetectors. A Textronix TDS 3054 with a 500 MHz bandwidth was sufficient to measure the 3 ns rise time of each tilt pin. Both scopes were triggered by the fiducial generated with the first light interruption detector. The fiducial was used to trigger a delay generator, which then was used to simultaneously trigger both scopes such that they are on the same time base. The delay generated was adjusted based on the target offset and projectile velocity to center the oscilloscope's record on the expected shock arrival.

3.3.3 Multi-Point VISAR

Two shots were performed using multiple VISAR probes to monitor a variety of locations on the rear surface of the target. Given the complexity of the diagnostics involved and the size of the target, these shots were performed at the Sandia facility. These shots were essentially the same as the bare fiber single-point experiments except a Plexiglas fixture, shown in Figure 3.15, was used to mount several of the probes at locations very close together. The fixture was precisely machined such that the probes were located along the centerline of the target with nominal radii of 0, 1.35, 2.69, 5.21, and 7.21 mm. Laser light is supplied by a Coherent V-10 diode-pumped solid-state laser operating at 532 nm, and a variety of push-pull VISAR modules were used in conjunction with the collected light. A multi-beam VAYLN V.I.P. VISAR system with a fringe constant of 844 $m/s/f$ was used for all of the beams and mini-VISAR modules were used to provide dual-delay capabilities to three of the probes. The probes at 0, 1.35, and 5.21 mm utilized modules with fringe constants of 543, 357.7, and 107.1 $m/s/f$, respectively.

As shown in Figure 3.15, the Mach lens target is glued into a target plate assembly where there

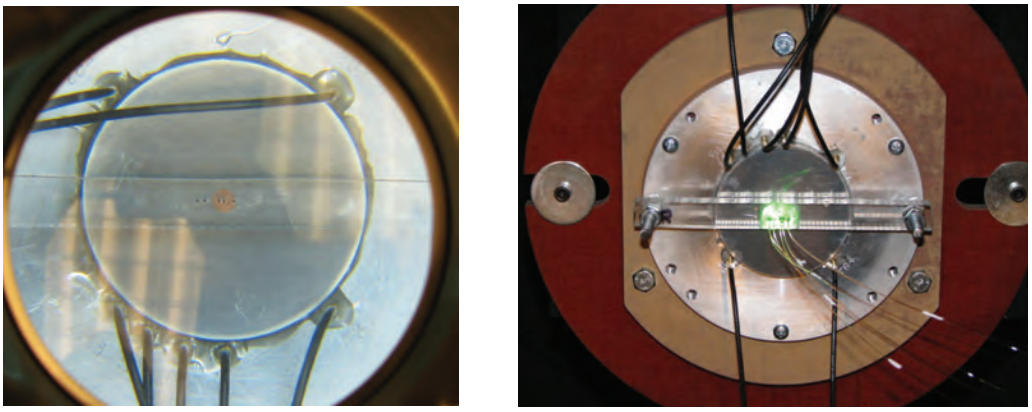

(a) (b)

Figure 3.15: Multi-point VISAR target assembly at Sandia's STAR facility. The rear surface of the target with the mounted probe holder is shown in (a). The assembly is mounted on the end of the barrel with the bare fiber probes in (b).

are seven shorting pins located along an 82.55 mm bolt circle diameter. There are four equally spaced tilt pins that are flush with the impact surface. The three other pins are lumped together and have nominal stand-offs of 0.8, 12.8, and 24.0 mm from the impact surface. These pins are used to measure the impact velocity and the middle pin is used to trigger the data collecting hardware.

3.3.4 ORVIS

The diagnostic capabilities at the Sandia STAR facility also include an ORVIS system. This system, shown in Figure 3.16, uses an adjustable optical rail running alongside the barrel to bring light into the target chamber through a lexan diagnostic port. The input rail contains the line shaping optics and is adjusted such that a line of 532 nm coherent laser light is entering the target chamber at the center of the target. As shown in Figure 3.16(b), a disposable adjustable mirror is used to align the input laser line on the center of the target and send the reflected light to the collection rail. The collection rail contains a collection lens that collimates the return light and a series of relay lenses that reduce the line length before being sent into the interferometer. The interferometer sits on a floating optical table for which the optical setup shown in Figure 3.7 is used to create interference fringes. Etalon, 76.4 mm in length, was used to provide the time delay in the system and the angle of offset was set such that 10 f/cm were seen at the viewing plane. The resulting fringe constant for this system is 670 $m/s/f$. The interference pattern is recorded using a Hamamatsu streak camera with a CCD collecting 1344 pixels in the spatial direction and 1024 pixels over the temporal sweep. In these experiments, an 8 mm line was imagined with a 5 μs sweep, giving a system resolution of approximately 24 μm and 5 ns in space and time, respectively.

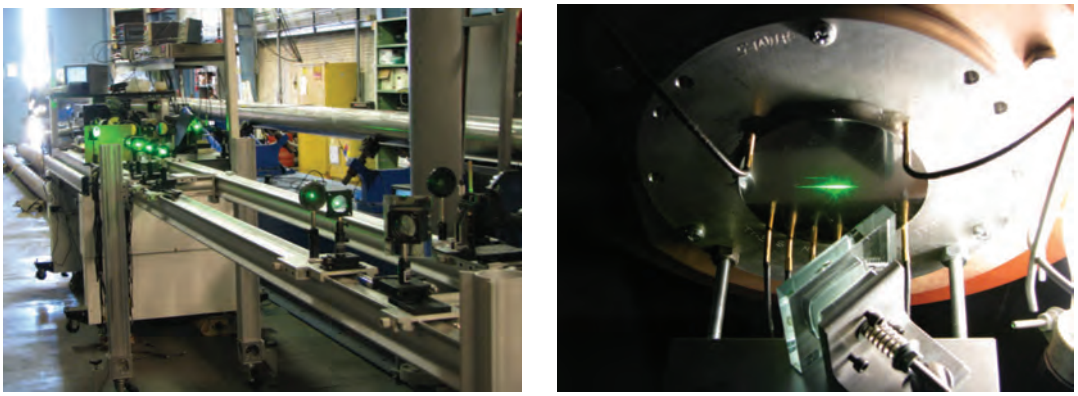

(a) (b)

Figure 3.16: ORVIS experimental setup at Sandia's STAR facility. The optical rails and interferometer are shown in (a) and the mounted rear surface of the target with the reflected laser line is given in (b).

Chapter 4

Numerical Simulations

Numerical computations can provide detailed information in complex multi-dimensional, multi-material dynamic deformation processes. A useful class of codes, deemed hydrocodes, solve the conservation equations to capture the hydrodynamic flow of the material. Often, these codes also contain the addition of constitutive equations to model the deviatoric response of the material. This chapter contains the results of the hydrocode simulations that were performed to gain greater insight into the Mach lens configuration. A brief summary of the hydrocode used throughout the rest of this dissertation, along with the material parameters required for the computations, is given in the following section. Section 4.2 provides in depth details for the response of copper under both the strong and weak confinement Mach lens regimes. The chapter concludes with an example of the $\alpha - \epsilon$ phase transition in iron on the Mach wave configuration.

4.1 The CTH Hydrocode

CTH is a hydrocode developed at the Sandia National Laboratories for the purposes of modeling problems characterized by large deformations, including the propagation of shock waves. The solution algorithm is a second-order accurate finite element Eulerian scheme, which has been shown to capture much of the key physics seen in shock physics experiments [48]. For these reasons, CTH was chosen as an ideal platform for simulating the Mach lens experiment.

The symmetry of the Mach lens configuration allows for the use of a 2-D axisymmetric simulation, and single processor calculations were found to be sufficient. The hydrodynamic response of the system is handled by the material EOS input for which a Mie-Grüneisen EOS centered on a linear shock-particle velocity was used when the materials were expected to remain in a single phase. A multi-phase material response was accounted for by using a tabular form of the EOS given by the built-in SESAME library [54]. The EOS parameters used in the simulations are shown in Table 4.1 where ρ_0 is the initial density, c_0 and s are the linear fit parameters from Eqn. 2.45, and γ_0 is the Grüneisen coefficient defined by Eqn. 2.47.

Table 4.1: EOS parameters obtained from shock data in the literature [62].

Material	$\rho_0\ (g/cm^3)$	$C_0\ (km/s)$	s	γ_0
Copper	8.924	3.914	1.508	1.99
6061-T6 Aluminum	2.703	5.332	1.344	1.97
Molybdenum	10.208	5.137	1.22	1.49
Iron (α phase)	7.856	4.63	1.33	1.65
Iron (ϵ phase)	7.856	3.745	1.676	2.40
Iron (multiphase)	SESAME EOS #2150 [55]			

The material's constitutive response was handled by classic high pressure engineering models including Johnson-Cook [52], Zerelli-Armstrong [84], and Steinburg-Guinan-Lund [75, 76]. While none of these models seemed to deviate much from perfect plasticity in the measured shock properties, the subtle effects of strength seem to play a larger role in this configuration than would otherwise be expected in the analogous one dimensional plate impact setup. As such, the Steinburg-Guinan-Lund models built-in to CTH [79] were used in all of the numerical simulations presented here. The strain-rate-dependent form of the model defines the yields stress, Y, as

$$Y = \left[Y_T\left(\dot{\epsilon}^p, T\right) + Y_A f\left(\epsilon^p\right)\right] \frac{G\left(P,T\right)}{G_0}, \tag{4.1}$$

where G is the pressure and temperature dependent bulk shear modulus, ϵ^p is the equivalent plastic strain, and Y_A is the yield strength at the Hugoniot elastic limit. The bulk modulus assumes the form

$$G\left(P,T\right) = G_0\left[1 + \frac{AP}{\eta^{1/3}} - B\left(T - 0.02585\right)\right], \tag{4.2}$$

where A and B are material constants and η is the compression ratio (ρ/ρ_0) . The work hardening function, $f\left(\epsilon^p\right)$ is given by

$$f\left(\epsilon^p\right) = \left[1 + \beta\left(\epsilon_i + \epsilon^p\right)\right]^n, \tag{4.3}$$

where β, ϵ_i , and n are fitting parameters. The plastic strain rate is modeled by

$$\dot{\epsilon}^p = \left(\frac{1}{C_1} e^{\frac{2U_K}{T}\left(1 - \frac{Y_T}{Y_P}\right)^2} + \frac{C_2}{Y_T}\right)^{-1}, \tag{4.4}$$

where Y_P is the Peierls stress, $2U_K$ is the energy necessary to form a pair of kinks in a dislocation segment, and C_1 and C_2 are material parameters. Additionally, the model also includes melting by

Table 4.2: Parameters used in the Steinburg-Guinan-Lund strength model [79].

Parameter	Units	Copper	Iron	6061-T6 Aluminum	Molybdenum
Y_0	$dynes/cm^2$	$1.2 \cdot 10^9$	$3.4 \cdot 10^9$	$2.9 \cdot 10^9$	$1.6 \cdot 10^{10}$
Y_{max}	$dynes/cm^2$	$6.4 \cdot 10^9$	$2.5 \cdot 10^{10}$	$6.8 \cdot 10^9$	$2.8 \cdot 10^{10}$
T_{mo}	eV	0.154	0.205	0.105	0.315
a	–	1.5	1.4	1.5	1.5
γ_0	–	2.02	1.93	1.97	1.59
A	$\left(dynes/cm^2\right)^{-1}$	$2.83 \cdot 10^{-12}$	$2.26 \cdot 10^{-12}$	$6.52 \cdot 10^{-12}$	$1.14 \cdot 10^{-12}$
B	eV^{-1}	4.38	5.28	7.15	1.76
n	–	0.45	0.35	0.1	0.1
C_1	sec^{-1}	0	0	0	$3.57 \cdot 10^7$
C_2	$dynes - sec/cm^2$	0	0	0	$1.24 \cdot 10^4$
G_0	$dynes/cm^2$	$4.77 \cdot 10^{11}$	$7.7 \cdot 10^{11}$	$2.7 \cdot 10^{11}$	$1.25 \cdot 10^{12}$
β	–	36	43	125	10
ϵ_i	–	0	0	0	0
Y_P	$dynes/cm^2$	0	0	0	$1.67 \cdot 10^{10}$
U_K	eV	0	0	0	0.372
Y^0_{max}	$dynes/cm^2$	0	0	0	$1.60 \cdot 10^{10}$
Y_A	$dynes/cm^2$	0	0	0	$9 \cdot 10^9$

using a modified Lindemann law defined by

$$T_m = T_{mo} e^{2a\left(1-\frac{1}{\eta}\right)\eta^{2(\gamma_0 - a - 1/3)}}. \tag{4.5}$$

A summary of the parameters used in the simulations is given in Table 4.2.

A typical simulation is shown in Figure 4.1 and illustrates the features expected in a Mach lens configuration. In this simulation, a thick aluminum disk impacts a Mach lens target with an aluminum outer cylinder and copper inner cylinder at 1.558 km/s. A very long target was simulated to evaluate the steady state evolution of the wave profile. The length to diameter ratio (L/D) of the inner cylinder is 6.3, and the arrivals of the Mach wave at various lengths along the centerline are shown in 4.2 (a). The symmetry boundary condition is used along the centerline of the target to simulate the axisymmetric nature of the problem. The rest of the mesh was given ghost cell boundary

conditions in which no mass is allowed to enter the mesh, but mass is allowed to leave. Generally, however, the mesh was constructed such that it was large enough to contain the entire problem so that only the symmetry boundary condition is important. A graded mesh, shown in Figure 4.1(c), was used to account for the multiple length scales in the problem. The mesh is constructed such that there are approximately 200 square cells across the radius of the outer cylinder. The inner cylinder is then refined such that it contains a similar amount of cells across its radius. A convergence study was conducted to verify that this type of mesh is sufficient to provide a consistent solution for all of the simulations examined. The default CTH contact algorithm is used in which two materials in contact are assumed to have the same velocity. Nothing special was used to model the interface between the inner and outer cylinders. The impactor is constructed such that it is initially in contact with the target and is given the initial condition that all of the material points have a velocity equal to the impact velocity. Thus, time 0 corresponds to impact to the target impact. The simulations were run for 1 μs past the expected free surface arrival time of the shock in the outer cylinder.

The contour plots constructed in Figure 4.1 show the entire diameter of the inner cylinder and a portion of the surrounding outer cylinder. The contours show the evolution of pressure in the spatial configuration with impact occurring on the left and propagating towards the right. The first profile, at 0.75 μs , illustrates the behavior of the specimen immediately after impact, where initially plane shocks propagate into both materials, with a conically converging shock propagating toward the centerline from the interface. Upon convergence, at ~1.25 μs , a Mach reflection develops and the overall shape and characteristics of the reflection evolve as it approaches the steady state solution. Finally, around 4.0 μs, the reflection has converged on the steady state solution and propagates unchanged through the rest of the target. The length of target required for the transition to steady state varies depending on the outer cylinder material (initial wave speed mismatch). As will be shown later, an L/D ratio of 5 is sufficient for all of the configurations examined in this work.

A more quantitative view of these simulations can be seen by examining wave profiles at various radii in the target. Figure 4.2 illustrates two such line plots: one along the centerline of the target, and the other along the interface between the inner and outer materials. The plots show the temporal evolution of 50 tracer particles evenly spaced throughout the length of the target. Thus, these line plots may be viewed as the temporal evolution of the Mach reflection at a fixed radius.

The centerline profile, Figure 4.2(a), illustrates the growth of the Mach reflection in the Mach stem regime. At very early times, the profiles show the shock up to the initial Hugoniot state as the plane wave passes. Eventually, at ~ 0.8 μs, the arrival of the converging shocks and subsequent Mach reflection from the interface reflection can be seen as the axial velocity increases. The velocity continues to grow as the Mach reflection transitions to the steady state, where at ~ 4.0 μs (L/D ~ 4) the velocity profile essentially becomes constant and self-similar for the rest of the tracers. This view of the simulation also illustrates the form of the wave expected to result behind the Mach stem. As

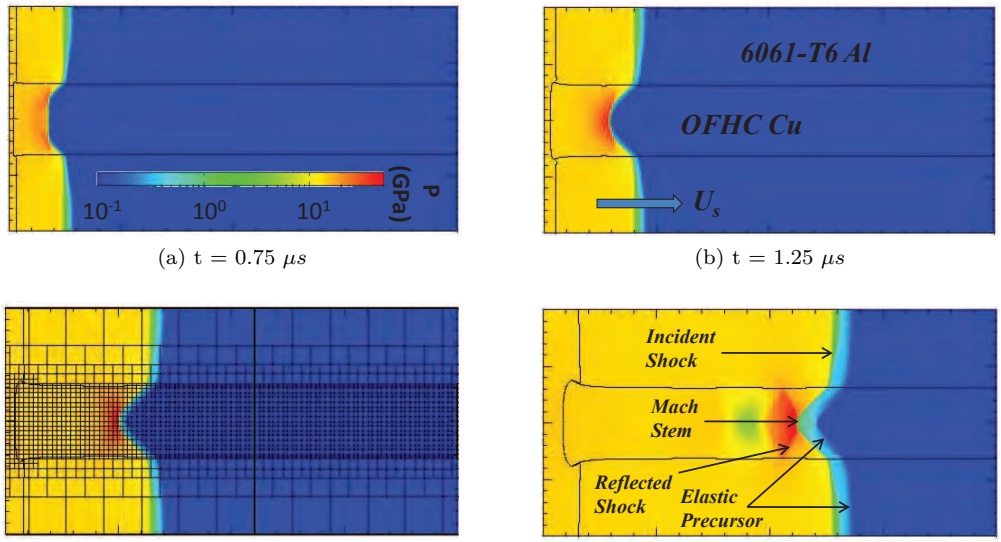

(a) t = 0.75 μs (b) t = 1.25 μs

(c) t = 2.00 μs (d) t = 4.00 μs

Figure 4.1: Simulation of an aluminum/copper composite target impacted by aluminum at 1.558 km/s. The evolution of the pressure contours at increasing time from impact illustrate the development of the steady state Mach reflection. A 24x24 square mesh is contained within each block shown in (c).

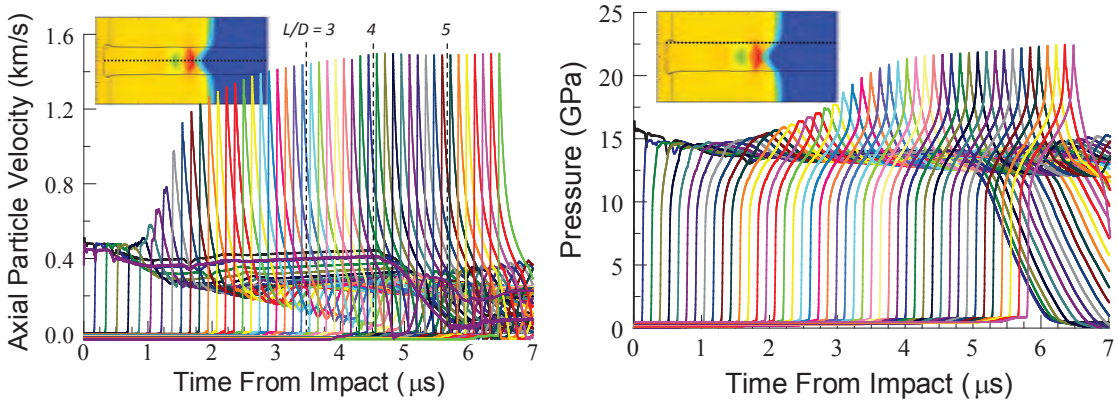

(a) (b)

Figure 4.2: Line plots for the simulation shown in Figure 4.1. The particle velocity line plots taken along the centerline of the target is shown in (a), while a pressure line plot at material interface is given in (b).

shown, the temporal wave profile is analogous to the Taylor wave commonly seen in explosives, in which the arrival of the wave will shock the material to the Hugoniot state and then is immediately followed by a release wave that drops the material down to a lower pressure state. The response is additionally complicated by the fact that, in this simulation, the longitudinal elastic wave speed is faster than the shock speed in the outer cylinder. As a result, continuity requires the propagation of precursor waves in the inner cylinder as well. This results in the small increase in particle velocity seen prior to the shock. The implications of this precursor are discussed in the analysis of the experimental data.

The two-shock regime of the Mach reflection can be seen in Figure 4.2(b), where the line plot is located along the material interface. As shown in the insert, this is far enough away from the center line of the target that the tracer particles will no longer be intersecting the Mach stem. Instead, what is seen is the initial plane shock followed once again by an increase in particle velocity as the converging shocks arrive. However, at this location, the incident/reflected shock regime is monitored. This can be seen at $\sim 1.5\ \mu s$, when this two-shock solution becomes evident as the incident shock followed by the reflected shock begins to form. Once again, at $\sim 4.0\ \mu s$, the two-shock wave profile approaches a steady state and remains constant throughout the rest of the target. It can be seen that this profile varies somewhat from the idealization presented in Section 2.2.5. As shown in Figure 4.2(b), there is a ramp in the particle velocity following the initial shock. It is expected that this ramp is due to the curvature of the incident shock. In a perfect gas, it has been shown that the curvature of a shock front results in gradients in the downstream flow properties [51]. This qualitative property is not expected to change in the translation to the shock properties in solids. Overall, however, the simulations are consistent with the idealization of the problem given in Section 2.2.5.

4.2 Copper Target

4.2.1 Strong Confinement

As illustrated in Section 2.2.5, two types of solutions are possible in the Mach lens configuration, with the distinction being the response of the outer cylinder. In the strong confinement solution, a single oblique shock in the outer material is sufficient to satisfy equilibrium at the interface with the inner material. While the previous simulation in Section 4.1 was an example of strong confinement, a more detailed look at the wave configuration, along with a comparison to the shock polar model, is given here. The simulation shown in Figure 4.3 is identical to the previous example except a copper plate with a velocity of 2 km/s is used as the impactor. The shock polar analysis for these impact conditions is shown in Figure 4.3(a), where the intersection of the inner and outer material shock polars presents an obvious solution and defines the interface state. The interface pressure is

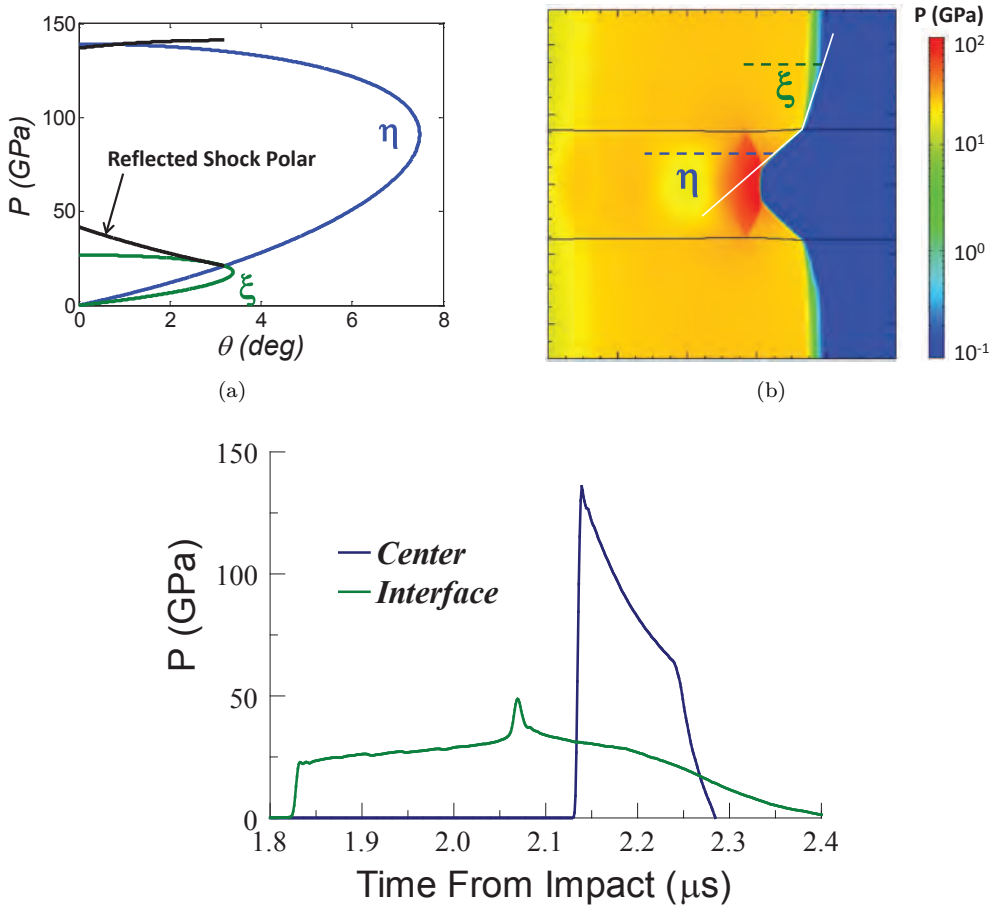

Figure 4.3: Illustration of the strong confinement solution through an aluminum/copper target with a copper impactor at 2 km/s. The shock polar solution in (a) is compared to the simulated shock angles in (b) and the simulated steady state pressure profiles at both the interface and the center of the inner cylinder in (c).

calculated to be 21 GPa with an initial flow deflection angle of 3.19°. The corresponding shock angles are 40.56° and 72.52° for the inner and outer materials, respectively. Assuming the reflected shock returns the flow to its original orientation, the reflected shock pressure is estimated to be 42 GPa . At the center of the target, in the Mach stem regime, the wave is calculated to be traveling at 7.18 km/s, which relates to a pressure of 139 GPa and is given by the maximum pressure on the inner material shock polar. Contours at a snapshot of the simulated steady state configuration along with an overlay of the polar analysis angles are given in Figure 4.3(b). As shown in this qualitative comparison, the agreement in the predicted shock angles is excellent. A plot of the steady state pressure profiles at the interface and center of the copper target, shown in Figure 4.3(c), gives a quantitative comparison of the two methods. At the center of the cylinder, the peak pressure is 137 GPa which is within 2% of the shock polar analysis. At the interface, the initial shock jump

is 21.6 GPa, which is, again, in excellent agreement with the predicted polar value. As shown in the interface pressure profile, however, there is a ramp in the pressure immediately following the incident shock before the reflected shock increases the pressure to just over 30 GPa. The reflected shock then increases the pressure to approximately 49 GPa. As mentioned previously, the ramp is an effect of the curvature of these shocks and cannot be accounted for in the simple polar analysis making the reflected shock pressure a conservative estimate. The approximate magnitude of the jump, however, seems to be modeled well using the reflected shock polar.

4.2.2 Weak Confinement

In the weak confinement solution, an oblique shock in the outer material is no longer capable of turning the flow the necessary amount to reach an equilibrium satisfying state. As discussed in Section 2.2.5, an expansion wave is required to find an admissible solution. A typical weak confinement solution is illustrated through the impact of a molybdenum and copper Mach lens configuration with a copper impactor at 1.5 km/s. The results of this simulation are given in Figure 4.4. The shock polar solution shown in Figure 4.4(a) illustrates the use of the expansion wave to calculate the interface state. The angles obtained from this solution 46.24° and 69.62° for the inner and outer cylinders, respectively. As shown in Figure 4.4(b) the overlay of these angles with the simulated pressure contours once again demonstrate excellent agreement. Additionally, the expansion wave can be seen in the pressure contours, so it is encouraging to see that the simple shock polar analysis is capturing much of the physics seen in the problem. The effect of the confinement can also be seen in the behavior of the Mach stem. In this case, the stem is much larger and also has a pronounced curvature at greater radii. A plot of the steady state pressure profiles at the center of the inner cylinder and the interface is given in Figure 4.4(c). The peak pressure at the center of the Mach stem is calculated to be 70.91 GPa and 67.18 GPa for the shock polar and numerical simulation, respectively. While this is reasonable agreement between the two, the difference is attributed to the precursors in the copper inner cylinder, clearly seen in Figure 4.4(a). The state at the interface is more difficult to quantify since the form of the wave is a ramp (due to the expansion) rather than a shock. However, the initial low pressure shock predicted by the shock polar agrees well with this profile.

In this simulation, the longitudinal wave speed in the molybdenum is greater than the shock velocity, and, as a result, the elastic precursor reflects into the inner cylinder. As illustrated, the continuity of the elastic wave from the outer cylinder forms multiple reflections in the inner cylinder since the behavior at these pressures is largely elastic-plastic rather than hydrodynamic. The higher strength of the molybdenum combined with these reflections causes plastic deformation in the copper cylinder, where, as shown in Figure 4.4(c), the peak pressure of this precursor is 2.3 GPa. Thus, to correctly calculate the shocked state behind the Mach stem, the non-quiescent state in front of

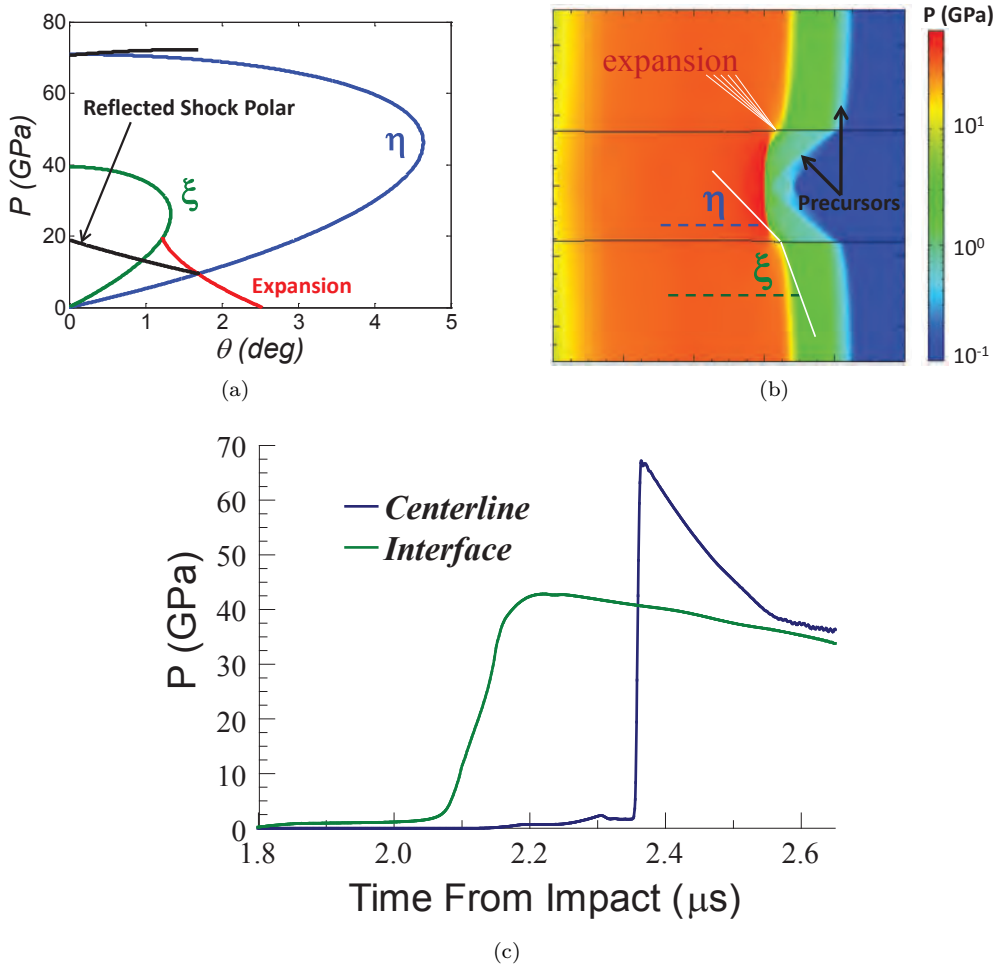

Figure 4.4: Illustration of the weak confinement solution through a molybdenum/copper target with a copper impactor at 1.5 km/s. The shock polar solution in (a) is compared to the simulated shock angles in (b) and the simulated steady state pressure profile at both the interface and the center of the inner cylinder in (c).

the shock must be accounted for. This correction is discussed in detail in Chapter 5, and in this particular example, the hydrodynamic theory is estimated to be in error by nearly 5%. Further, as shown in Figure 4.4(c), the interface profile is far from what is expected based on the shock polar analysis. The reflected shock in the simulation immediately follows the expansion wave, and the shock increases the pressure to approximately 42 GPa, well above the predicted polar value of 19.5 GPa. As shown in Figure 4.4(a), 40 GPa corresponds to shock pressure in the far field outer cylinder. Thus, it can be assumed that a lower energy configuration exists if the pressure is allowed to equilibrate across the entire target directly behind the incident shock rather than matching the flow angles with an extra reflected shock. A comparison of Figures 4.3(a) and 4.4(a) suggest this criteria is determined by whether the reflected shock polar lies above or below the normal shock pressure in the outer cylinder.

4.3 Iron Target

In the event that a phase transition occurs between the interface and Mach stem pressures, the resulting wave configuration can be significantly altered. The effect of phase transitions on the shock wave structure has been briefly discussed in Section 2.2.6. As an example, the polymorphic phase transition ($\alpha-\epsilon$) occurring in bcc iron at 13 GPa [14] is examined. Two simulations will be presented that contain evidence of this phase transition. The configurations are nearly identical; utilizing a copper impactor, a molybdenum outer cylinder, and an iron inner cylinder. The dimensions of the simulations match the corresponding experiments described in Table 5.3. The only difference in the simulations, labeled MW-I1 and MW-I2, are the impact velocities of 1.19 and 1.31 km/s, respectively. The resulting expected interface pressures generated by the shock polar analysis are 5.7 and 6.7 GPa, respectively, which is well below the phase transition pressure. The corresponding Mach stem pressures (in the event of no phase transition) are over 50 GPa. Hence, some evidence of the phase transition is expected in the simulations.

A plot of the pressure contours, shown in Figure 4.5, illustrate the complexity of the reflected waves. In both cases, the initial oblique shock in the inner material represents the phase transition. Since the phase transition is well characterized, the point on the shock polar (13 GPa) is given directly, and so the angle and velocity components associated with this wave are immediately known. Similarly, since this is a weak confinement example, the shock angle in the outer cylinder is given by the angle associated with the sonic point. These calculated angles (using the parameters in Table 4.1) are plotted as the white lines in Figure 4.5. As shown, there is reasonable agreement between the simulation and this simple methodology. The differences in the phase transition angle are attributed to the use of the tabular EOS in the simulation instead of the simple linear shock-particle velocity relationship for the calculated angles.

What is unclear without examining the simulations is whether the oblique shock associated with the phase transition will traverse the entire inner cylinder. The lack of an inherent length scale in the analytic approach of shock polars makes it very difficult to estimate the relative dimensions of the configuration. Thus, the results of the numerical simulations are used to gain insight into the nature of the solution. The lower impact velocity simulation (MW-I1) suggests the shock associated with the phase transition reflects off the axisymmetric boundary at the center of the target. This results in a gap between the phase transition shock and the trailing shock, which forms as a result of the reflected converging waves corresponding the second phase (ϵ). The shock polars reflecting this solution are given in Figure 4.6(a). As shown, the inner material forms an oblique shock (α phase) associated with the phase transformation pressure, from which a second shock (ϵ phase) is generated. A plot of the steady state pressure profiles at the center of the inner cylinder and at the interface are given in Figure 4.6(b). At the interface, the initial shock drives the pressure to the

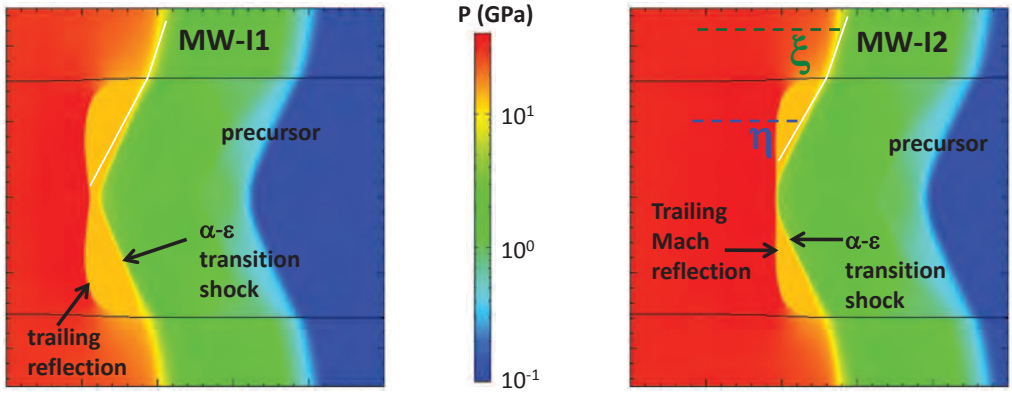

Figure 4.5: Pressure contours for the MW-I1 (impact velocity, 1.19 km/s) and MW-I2 (impact velocity, 1.31 km/s) simulations illustrating the effect of the $\alpha - \epsilon$ phase transition in iron on the wave configuration.

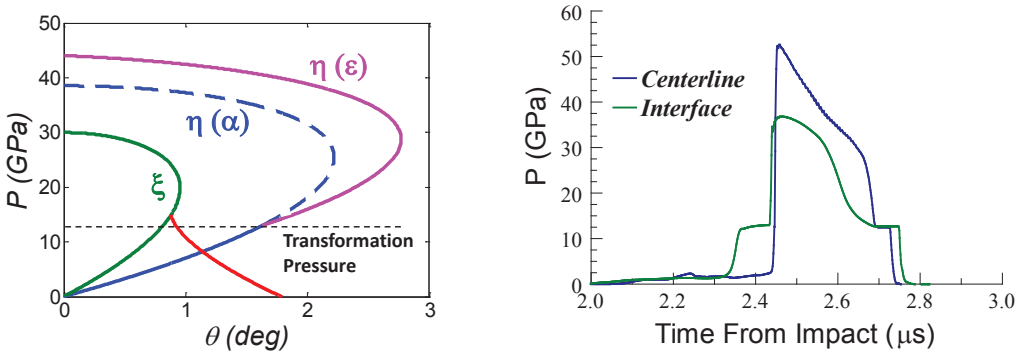

(a) (b)

Figure 4.6: The shock polar solution in (a) illustrates the key features of the simulated pressure profiles at both the interface and the center of the inner cylinder in (b) for a molybdenum/iron target with a copper impactor at 1.19 km/s (MW-I1).

transformation pressure (13 GPa) and is followed by the second shock which increases the pressure to the far field outer cylinder state given by the maximum of the outer cylinder (η) shock polar. This is consistent with what is observed in Section 4.2.2 for the weak confinement solution of a copper inner cylinder. A similar observation is made at the center of the inner cylinder. In this case, symmetry forces the trailing shock to be normal at the center of the cylinder so the resulting second shocked state can be calculated by examining the second shock Hugoniot (Eqn. 2.62) for the ϵ phase EOS. The maximum pressure on this shock polar (44 GPa) then gives the appropriate second shock pressure. As shown, the profile from the simulation agrees well with this argument as the first shock results in the phase transformation pressure while the second shock has a peak state of 43 GPa . This two shock wave profile is reminiscent of what is observed in one dimensional plate impact experiments [14] on iron.

The higher impact velocity simulation (MW-I2) results in a less intuitive solution. In this case,

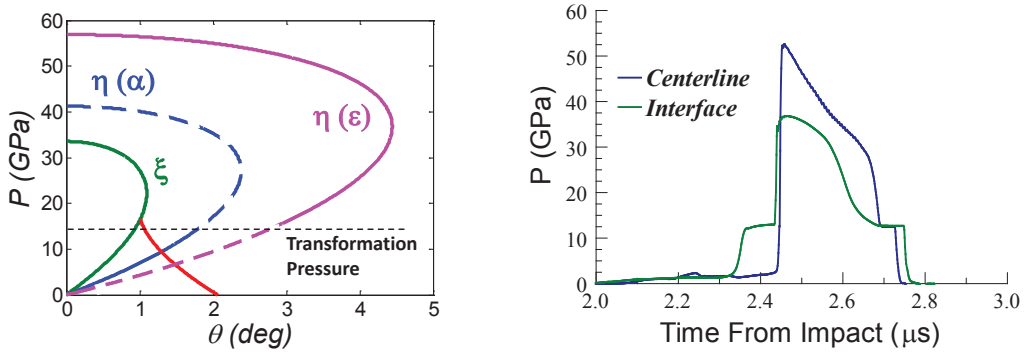

(a) (b)

Figure 4.7: The shock polar solution in (a) illustrates the key features of the simulated pressure profiles at both the interface and the center of the inner cylinder in (b) for a molybdenum/iron target with a copper impactor at 1.31 km/s (MW-I2).

the phase transition shock appears to be overtaken by a portion of the Mach reflection at the center of the cylinder. As a result the pressure profile at the center of the target is seemingly unaffected by the presence of the phase transition, while the outer portions of the inner cylinder contain clear evidence of the transition. Thus, while the interface state can be calculated using the same ideas used in the previous simulation (MW-I1), the state at the center of the inner cylinder has the form of the standard Mach lens solution. The shock polar analysis and simulated pressure profiles in Figure 4.7 reflect this. As shown in the shock polar, the state at the center of the inner cylinder is given by the standard shock polar for the ϵ phase and results in a pressure of 57 GPa. The corresponding simulated pressure profile agrees well with this methodology, resulting in a single shock to 53 GPa. Again, the differences here are attributed to the strength effects associated with the molybdenum confinement. Higher impact velocities will result in a further decreased presence of the phase transition until the interface pressure reaches the transition pressure of 13 GPa (2 km/s impact under these conditions).

Chapter 5

Experimental Results and Discussion

5.1 Copper Experiments

5.1.1 VISAR Experiments

As discussed in Chapter 3, a variety of diagnostics were used in the experiments in an attempt to validate the Mach lens technique. The primary method of characterizing the reflection is through velocity interferometry using either VISAR or ORVIS. A summary of the shots conducted on a copper inner cylinder is given in Table 5.1, where the shot number gives an indication of the type of diagnostic used in the experiment. Two multi-point VISAR experiments were conducted, which provides a wealth of information and, as such, these results will be presented first. The following section contains the results of the rest of the single-point experiments and a discussion on how Hugoniot information is extracted from the measured free surface velocity.

5.1.1.1 Multi-Point VISAR

In an attempt to fully validate the Mach lens technique, a multi-point VISAR experiment will be discussed in detail. The configuration of the experiment, numbered MW-V1, is given in Table 5.1. The numerical simulation of the experiment has been shown previously, in Figures 4.1 and 4.2. As shown in Figure 3.15, the experiment utilized four bare fiber VISAR probes positioned along the centerline of the target at radii of 0, 1.35, 2.69, and 7.21 mm. Dual-delay interferometry was used on the two inner most locations to verify the correct velocity is reduced from the fringe records. The shorting pins give an estimated tilt of 1.61 $mrad$ and the center impact time serves as the temporal fiducial for all data. The waveforms obtained in this experiment are shown in Figure 5.1 along with the results from the numerical simulation and the shock polar analysis. The insert in the figure shows the probe locations along with the upper half of the idealized Mach reflection. The experimental

Table 5.1: Summary of Mach lens experiments on copper.

Exp. No.	Materials[a]	Thickness[b] (mm)	Diameter[c] (mm)	u_I (km/s)	U_s^{outer} (km/s)	u_{peak} (km/s)	σ (GPa)	ρ (g/cc)
MW-V1	Al / Al / Cu	12.73 / 22.207	76.71 / 6.414	1.558	6.379	3.10	87.91	11.818
MW-V2	Cu / Al / Cu	6.817 / 14.069	38.354 / 3.218	1.140	6.398	3.34	95.35	12.076
MW-V3	304 SS / Al / Cu	3.08 / 15.824	37.94 / 4.831	1.401	6.546	3.44	100.63	12.112
MW-V4	304 SS / Al / Cu	3.07 / 15.926	37.92 / 4.816	1.310	6.414	3.28	94.32	12.009
MW-V5	Al / Al / Cu	12.85 / 21.933	76.45 / 6.416	0.787	5.861	Mach stem not measured		
MW-V6	304 SS / Mo / Cu	3.07 / 15.776	37.85 / 4.805	1.826	6.057	2.77	73.72	11.652
MW-V7	Al / Mo / Cu	3.16 / 15.766	37.71 / 4.803	1.446	5.568	1.84	44.63	10.757
MW-V8	304 SS / Mo / Cu	3.07 / 15.873	37.85 / 4.829	1.314	5.782	2.33	59.61	11.210
MW-V9	304 SS / Mo / Cu	3.07 / 15.840	37.95 / 4.826	1.043	5.641	2.06	50.99	10.982
MW-O1	Al / Al / Cu	12.63 / 17.418	50.8 / 4.806	1.241	6.166	-	-	-
MW-O2	Al / Mo / Cu	12.68 / 18.499	76.2 / 6.414	1.270	5.511	-	-	-

[a] Impactor / outer cylinder / inner cylinder

[b] Impactor / target

[c] Outer cylinder / inner cylinder

traces are color coded to each probe location. The gray dashed lines correspond to the results of the numerical simulation, which utilized dimensions identical to the experiment, and contained tracers at the probe locations. The colored dotted lines correspond to the shock polar analysis where the calculated free surface particle velocities, in increasing radii, correspond to the Mach stem (peak pressure on the shock polar), incident shock at the interface, reflected shock at the interface, and plane shock in the outer cylinder, respectively. In this case, the free surface approximation is used where the free surface velocity is taken to be twice the in situ particle velocity.

As expected, at the center of the target, the Mach stem arrives last in time and shocks the material to a peak state, followed by a release until a loss of contrast occurs in the interferometer. The peak free surface velocity is 3.10 km/s with the simulated value being 1.8% lower. As shown, the time of arrival of the simulated Mach stem is also in excellent agreement with the experiment suggesting the simulation is capturing the transient effects of the Mach wave transition accurately. The free surface particle velocity calculated from the shock polar analysis is 3.29 km/s, suggesting there is either a problem with the measured waveforms being in a steady state or with the hydrodynamic

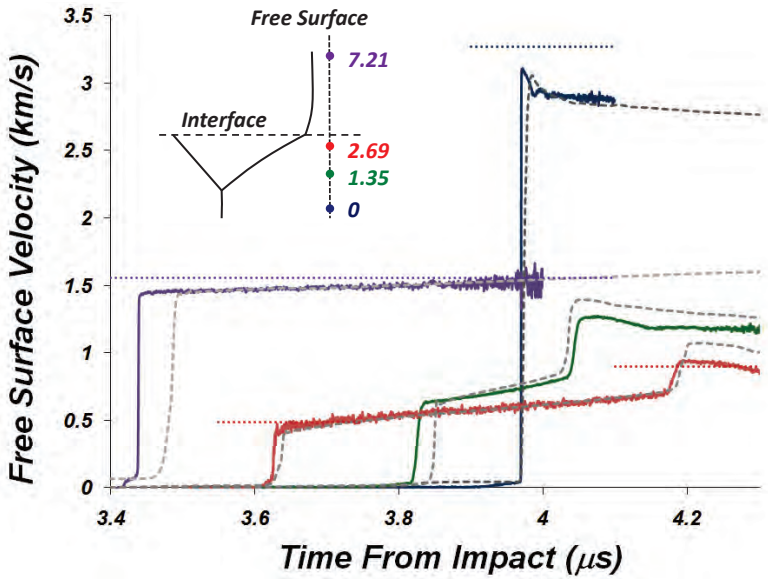

Figure 5.1: Experimental wave profiles obtained in MW-V1, aluminum/copper target impacted by copper at 1.558 km/s. The insert shows the color coded probe radii in relation to an idealized Mach wave. The simulated profiles are shown as gray dashed lines, while values obtained from the shock polar analysis are given as the dotted horizontal lines.

approximation. The magnitude of the precursor velocity, however, only represents about 1% of the peak particle velocity hence the strength effects in this experiment are expected to be negligible. Both the strength effects and the validity of the steady state approximation will be discussed in later sections.

Increasing in radius, the signal at the 1.35 mm probe arrives a couple hundred nanoseconds earlier. Here, a double shock can be seen in the waveform so it is expected this probe is monitoring the outer region of the Mach reflection where incident shock is followed by the reflected shock. The ramp in velocity after the initial shock suggests the incident shock has a non-trivial amount of curvature, which produces a pressure gradient in the downstream flow [51]. Slight uncertainties in the probe location are thought to produce the discrepancy in the arrival time. The simulation also appears to predict a reshock state that is higher than the experimental measurement. This suggests that the off-Hugoniot state calculated by the Mie-Grüneisen EOS is insufficient to accurately capture the multiple reflections in the experiment.

The earliest arrival of the Mach reflection occurs at the interface, near the probe position at a radius of 2.69 mm. The waveform looks qualitatively similar to the previous, except for a few key differences. First, the velocity is lower since the angle of obliquity changes as the wave converges on the appropriate interface pressure. This also supports the previous observation that curvature is present in the incident shock. Second, the gradient behind the incident shock is smaller, suggesting less curvature at this point. Finally, the time between the incident and reflected shock is greater.

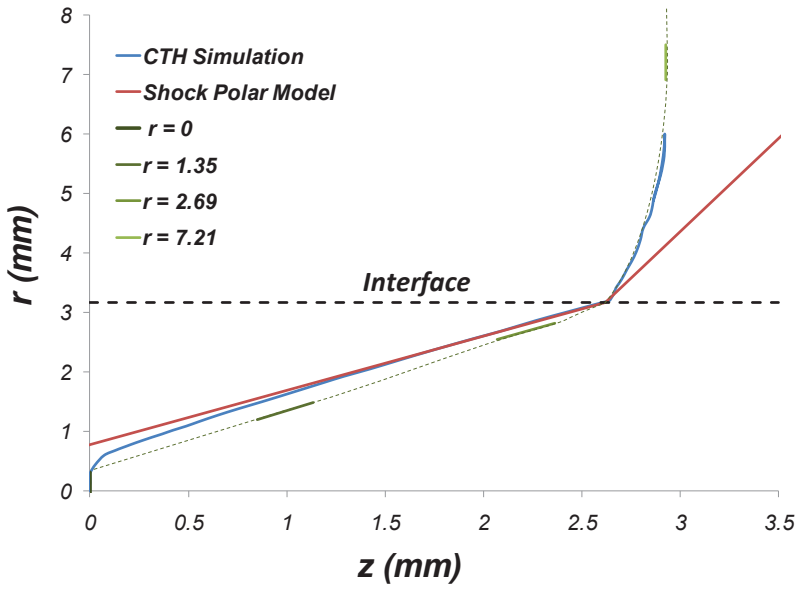

Figure 5.2: Spatial shock configuration obtained from the experimental wave profiles in Figure 5.1 along with the simulated configuration and shock polar angles.

As seen in Figure 5.1, the angle between these shocks results in a greater separation between the two measurement points, so this is simply a feature of the wave geometry. Also, shown in Figure 5.1 is a horizontal dashed line from the polar analysis predicting the reflected shocked state. This was calculated by assuming the flow returns to its original orientation ($\theta = 0$) behind the reflected shock polar. Since the measurement is taken close to the interface, another reasonable quantitative comparison can be made, in which case both the analytical model and simulation are found to be within 4% of the experimentally measured value. While the simple shock polar methodology cannot capture curvature effects, it does seem to predict the magnitude of the jump, especially when compared to the simulation. This is not surprising since both methods use the same EOS, but once again suggests a limit to the accuracy of the Mie-Grüneisen EOS in this situation.

The last probe, at a radius of 7.21 mm, is well into the outer cylinder. In this case, the slight effect of the diffraction of the outer shock is seen since the measured the velocity is slightly lower than the expected normal shock particle velocity, which is plotted as a dashed line in Figure 5.1. Once again, the ramp after the shock gives some indication as to the degree of curvature of this diffracted wave. Overall, however, the experimental waveform is captured very well by the simulation, suggesting the correct EOS for aluminum is used and giving confidence that the correct shock speed of the Mach wave can be calculated.

The analysis can be extended further by taking the experimental peak particle velocities from each probe and relating these to the appropriate pressure on the shock polar by using the known Hugoniot of copper, giving the tangent angles at each probe location as shown in Figure 5.2. As with the shocked states associated with the Mach reflection, both the simulations and the shock

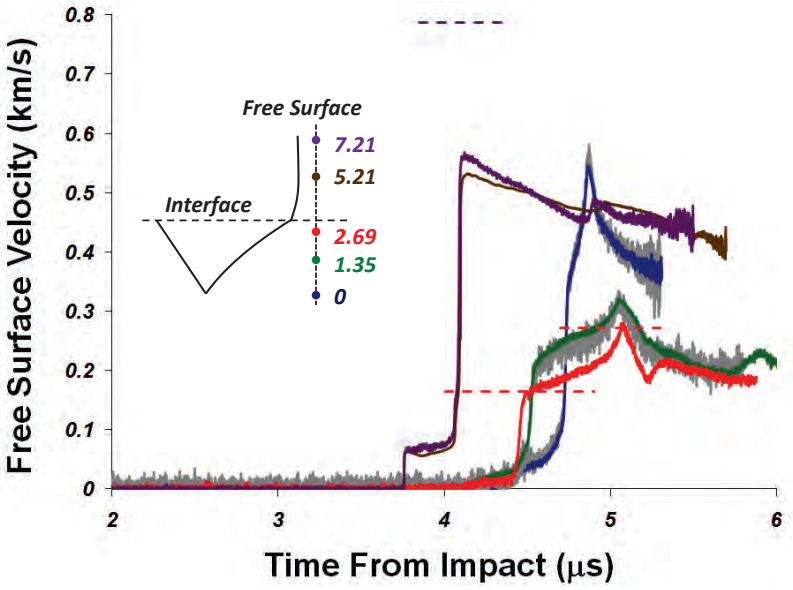

Figure 5.3: Experimental wave profiles obtained in MW-V5, aluminum/copper target impacted by copper at 0.787 km/s . The insert shows the color coded probe radii in relation to an idealized Mach wave. The dual-delay interferometers are shown in gray while values obtained from the shock polar analysis are given as the dotted horizontal lines.

polar model are in good agreement with the calculated experimental spatial configuration that is represented by the interpolation between the tangent angles.

The results from the second multi-point VISAR experiment, MW-V5, are shown in Figure 5.3. In this illustration, both signals from the dual-delay interferometers are plotted to illustrate the concept, and are used to verify that the probe located 0 mm (at the axis of symmetry) in this experiment did not measure the expected high pressure state associated with the Mach stem. The simulations suggest the diameter of the Mach stem in this experiment is extremely small, roughly 1/20 the radius of the inner cylinder, which corresponds to a diameter of 300 μm. Given the tolerance of the probes, the laser spot size, and possible perturbations due to tilt, it is perhaps not surprising that only the incident/reflected shock portion of the Mach reflection is observed. Given the form of the wave and the low velocity, the probes monitoring the aluminum outer cylinder at radii of 7.21 and 5.21 mm appear to have just begun attenuating from the edge release waves. The shock polar analysis plotted along with the VISAR traces indicate that the interface state approximated by the 2.69 mm probe is predicted extremely well. As such, it is assumed the release waves have not reached the inner cylinder and so the three inner probes are unaffected. Using the Mie-Grüneisen EOS to generate an isentrope (Eqn. 2.49) from the shocked state in the outer cylinder and taking the instantaneous slope at this pressure gives a release wave speed of 6.4 km/s. The distance the release has to travel from the outside of the outer cylinder to the interface is 35 mm. Thus, wave effects are not expected to become a problem in the inner cylinder until 5.5 μs, which confirms the

assumption and agrees well with the observed experimental waveforms.

5.1.1.2 Single-Point VISAR

In most of the experiments, a single VISAR probe was used to monitor the center of the copper target as described in section 3.3.2. A summary of the experiments is given in Table 5.1 and the measured waveforms are plotted in Figure 5.4. The time base for the waveforms is scaled by the target thickness for a direct comparison of all the experiments. As shown, this results in a qualitative view of the Mach wave speed-up as the outer cylinder material is changed and the impact stress is increased.

The MW-V2 experiment was conducted in order to experimentally verify that the measured configuration in MW-V1 was in the steady state. To do so, the length to diameter ratio of the inner cylinder was extended from 3.5 (MW-V1) to 4.4 (MW-V2). The impact configuration resulted in nearly identical shock speeds, but, as shown in Figure 5.4, the resulting free surface particle velocity is 3.34 km/s is now within 1.5 % of the predicted value from the shock polar analysis. The free surface velocity of 3.10 km/s, measured in MW-V1, corresponds to a shock speed on the known Hugoniot of 6.25 km/s, which is lower than the predicted value by 2%. Thus, it can be assumed that the Mach stem in MW-V1 had only reached approximately 98% of its steady state velocity at the point of the measurement and, as such, larger uncertainties are attributed to this measurement. A final interesting feature of the MW-V2 experiment is its lack of an elastic precursor. While this is inconsistent with the simulations, the longitudinal elastic wave speed predicted in the simulations, as shown in Figure 5.1, seems to be too high. The expected longitudinal wave speed of 6.35 km/s is very close to the wave speeds of both of these Mach reflections and gives further evidence that the speed of MW-V1 was slightly low, while MW-V2 attained the full steady state. As expected, the other two experiments conducted with an aluminum outer cylinder, which were at even higher pressures, also contain no evidence of a precursor.

The rest of the shots were conducted under a weak confinement regime using a molybdenum outer cylinder. Molybdenum has a similar longitudinal elastic wave speed (when compared to aluminum) of 6.25 km/s, but the slower shock response results in Mach reflection speeds well below this. As a result, a precursor is consistently measured which is on the order of 0.13 km/s, and arrives at approximately the same relative time while the shock speed shows significant speed up with increasing impact stresses.

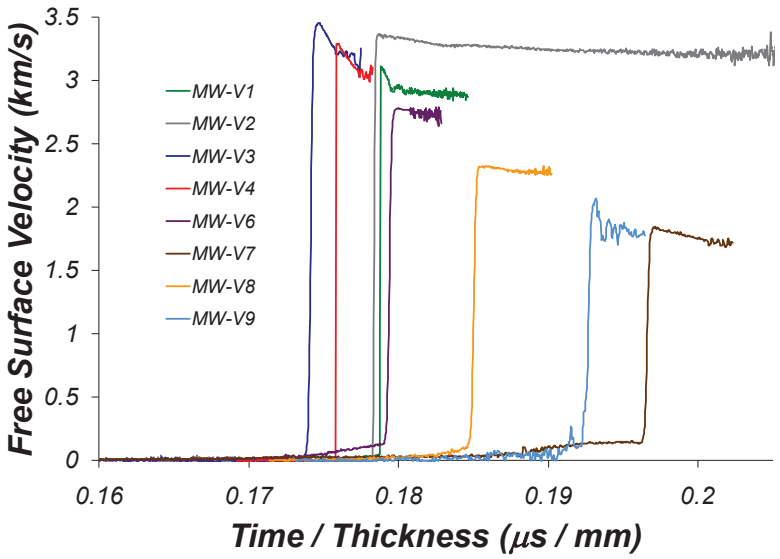

Figure 5.4: Free surface velocity profiles measured at the center of a copper inner cylinder in the Mach lens configuration. Time from impact is scaled by the target thickness to make a direct comparison of the profiles.

5.1.1.3 Hugoniot States

The true validation in these Mach lens experiments is the ability to calculate the shocked state behind the Mach stem. The particle velocity can be estimated by taking half of the free surface velocity and the entire configuration is assumed to be steady, hence the shock velocity can be calculated through previously discussed impedance matching techniques as long as the impactor and outer cylinder are well characterized materials. Typically, the measured shock and particle velocities are used in conjunction with the quiescent shock jump conditions to calculate the stress and density, even in the event of a small elastic precursor. Since most of the community is consistent in this regard, this does not present a problem. All of the strong confinement experiments (with aluminum outer cylinders), for example, seem to fall in this regime, and so the calculated shock and measured particle velocities immediately represent the Hugoniot. The weak confinement experiments (with molybdenum outer cylinders), on the other hand, contain much more significant strength effects, which can be seen in the precursor behavior prior to the arrival of the shock, which was also discussed in section 4.2.2. In the MW-V6 experiment, for example, the precursor magnitude is about 7% of the peak particle velocity which represents a significant effect for precise EOS measurements. Since the precursor introduces a small amount of deformation prior to the shock, the Hugoniot state can be calculated by using the Lagrangian jump conditions for a shock propagating into a non-quiescent material (Eqns. 2.37 and 2.38), giving

$$\sigma_x = \rho_0 U_s \left(u_p - u_p^*\right) + \sigma_x^*, \tag{5.1}$$

$$\rho = \frac{\rho_0 \rho^* U_s}{\rho_0 U_s + \rho^* \left(u_p^* - u_p\right)}, \tag{5.2}$$

where σ_x and ρ are the axial stress and material density, respectively. ρ_0 is the initial density, the asterisks indicate the material state ahead of the shock, and the rest of the properties refer to the shocked state. Unfortunately, accurately calculating the state ahead of the shock is extremely difficult. As suggested by the simulations, the precursor often contains multiple reflections and results in a state of multi-axial state of stress and strain. It can be assumed, given the multiple reflections and the relatively low strength of copper compared to the high strength of molybdenum, that the deformation is plastic. Given the low magnitude of the precursor, however, it is expected that the pressure dependence of the bulk modulus in this state is negligible, and so the deformation can be characterized by the initial bulk wave speed, C_0. Since the precursor particle velocity can be measured experimentally, the stress and density ahead of the shock can be written (Eqns. 2.42 and 2.43) as

$$\sigma_x^* = \rho_0 C_0 u_p^*, \tag{5.3}$$

$$\rho^* = \frac{\rho_0 C_0}{C_0 - u_p^*}. \tag{5.4}$$

The stress and density may now be calculated through Eqns. 5.1 and 5.2 giving the results seen in Table 5.1. Of course, in the event that the precursor is over-driven, the analysis once again reduces to the solution of the typical quiescent jump conditions to solve for the shocked state. The calculated Hugoniot states are shown in Figure 5.5 along with data obtained in the literature [62]. The error bars were obtained using the uncertainty analysis discussed in Appendix A, where the nominal errors are 2.5% in stress and 0.7% in density. As shown, the measured Hugoniot states are in excellent agreement with the data obtained from normal plate impact experiments. Further, the experimental errors do not seem unreasonable when compared to extremely precise EOS work [69] where errors of approximately 0.7% in stress and 0.2% in density are estimated. The largest source of error is the free surface approximation where the in situ particle velocity is taken to be half of the free surface velocity. In plate impact experiments this problem is avoided altogether by using either symmetric impact experiments or an impedance matched window to get a true measure of the in situ velocity. In the Mach lens configuration, however, symmetric impact becomes meaningless and the use of a window presents a variety of challenges as it will disrupt the steady state nature of the Mach wave propagation. Thus, given these experimental challenges, the free surface approximation is thought to be the best way to estimate the Hugoniot state. This approximation is equivalent to allowing the material to release along the principle Hugoniot rather than the isentrope, so a

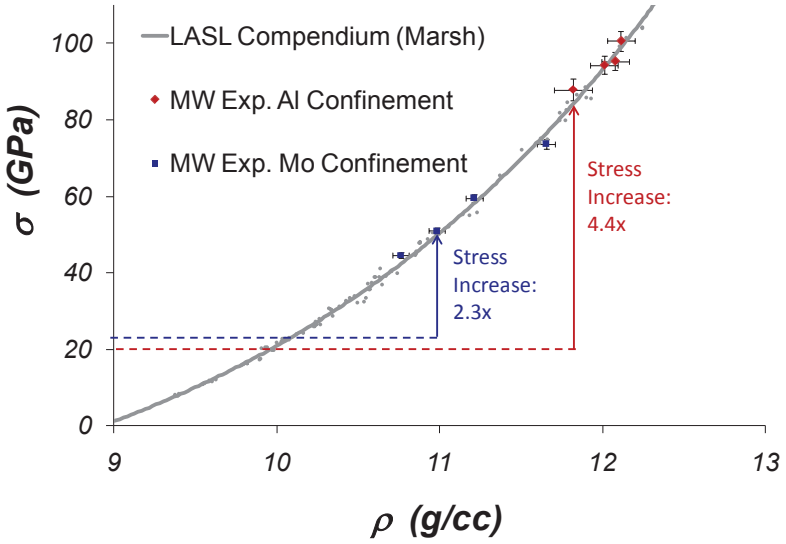

Figure 5.5: Calculated Hugoniot states for copper compared to data in the literature [62]. Representative points from each confinement illustrate the pressure increase from the equivalent plate impact experiment.

comparison of the velocities obtained with each method gives an estimate of the error associated with this approximation. The differences obtained are 0.65%, 1.8%, and 3.0% for shock stresses of 50, 100, and 150 GPa, respectively. Thus, while these errors are relatively small for the range of pressures examined in these experiments, care would have to be taken when extending the technique to ultra-high pressures. At 300 GPa, for example, the error is up to nearly 7%, which is probably not good enough for EOS measurements.

The results shown in Figure 5.5 also contain two examples of the gain in pressure using the Mach lens configuration when compared to the equivalent plate impact experiment. The gain is defined as the stress generated when the flyer impacts the copper inner cylinder in a conventional 1-D configuration. In the MW-V1 experiment, for example, the stress is estimated to be 88 GPa . The equivalent plate impact experiment, an aluminum flyer impacting copper at 1.558 km/s results in only 20 GPa, a multiplication in stress of 4.4 times. An alternative way to view this increase would be to determine the impact velocity required in this plate impact configuration to generate the pressure seen in the Mach lens configuration. In this example, the aluminum flyer would need to impact copper at 4.9 km/s to generate a stress of 88 GPa, illustrating the use of the Mach lens to generate pressures well above the velocity range accessible to the gun. The equivalent plate impact pressures and required impact velocities for the rest of the experiments are given in Table 5.2. As shown, the Mach lens dramatically extends the range of pressures that can be accessed by a given impact velocity, which, as discussed in section 2.2.5, is one of the primary goals of this dissertation. Also given in Table 5.2 are two theoretical results for the maximum copper impactor velocity of 2 km/s on each configuration. These theoretical results were presented in Figure 3.9,

Table 5.2: Summary of Mach lens gains on a copper target.

Exp. No.	σ - Mach Lens (GPa)	σ - Plate Impact (GPa)	Pressure Gain	Plate Impact Velocity (km/s)
MW-V1	87.91	19.8	4.4	4.9
MW-V2	95.35	24.3	3.9	3.3
MW-V3	100.63	31.1	3.2	3.5
MW-V4	94.32	28.7	3.3	3.3
MW-V6	73.72	42.9	1.7	2.8
MW-V7	44.63	18.1	2.5	3.0
MW-V8	59.61	28.8	2.1	2.4
MW-V9	50.99	22.0	2.3	2.1
Cu/Al/Cu at 2.0 km/s[a]	139.2	48.4	2.9	4.3
Cu/Mo/Cu at 2.0 km/s[a]	84.6	48.4	1.7	3.1

[a] Impactor / outer cylinder / inner cylinder (theoretical results)

which shows the extension of the copper Hugoniot from a symmetric plate impact experiment, which results in a maximum particle velocity of 1 km/s and a pressure of 48 GPa. The slower molybdenum confinement extends the pressure to 85 GPa while the faster aluminum confinement allows for pressures of nearly 140 GPa to be accessed. Thus, for the systems studied here, the Mach lens assembly can be said to more than double the capabilities of a standard powder gun in terms of the equivalent impact velocities that can be reached.

5.1.2 ORVIS Experiments

Two experiments were conducted with the ORVIS diagnostic described in Section 3.2.3 in an attempt to obtain free surface velocity information with a high degree of resolution in both space and time. The shot details are summarized in Table 5.1. The first shot, MW-O1 (strong confinement) imaged a line off the center of a diamond turned rear target surface. The resulting streak camera image, shown in Figure 5.6(a), demonstrates many of the features expected in these experiments. The wave arrivals at the rear surface create a clear representation of the initial arrival of the Mach wave configuration including the elastic precursors, Mach wave, and some evidence of the reflected shock. In Figure 5.6(b) the precursor and Mach reflection have been digitized, scaled by the steady state Mach wave velocity, and plotted along with profiles of the corresponding numerical simulation and

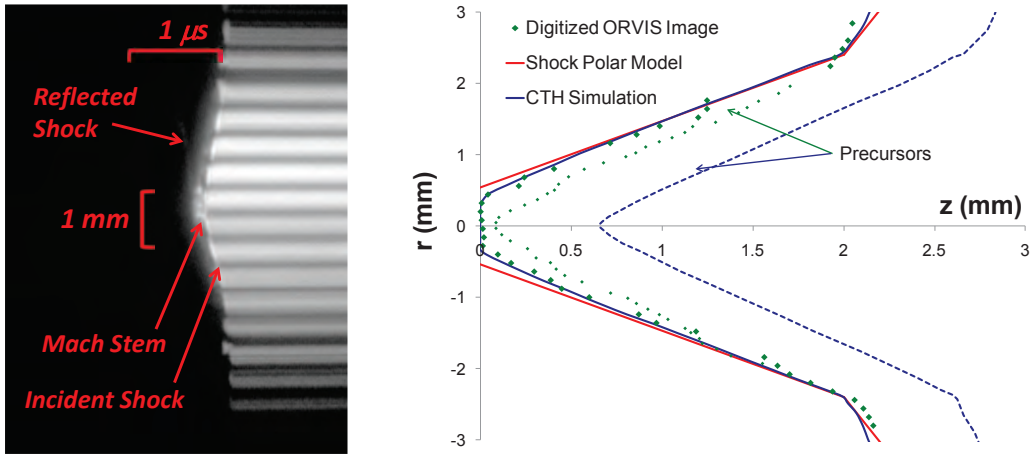

(a) (b)

Figure 5.6: Experimental results from MW-O1, aluminum/copper target. The ORVIS streak camera image in (a) is digitized to produce the Mach configuration in (b). The experimental results in (b) are overlaid with the corresponding numerical simulation and shock polar analysis.

shock polar analysis. As shown, the simulation seems to do an excellent job of calculating the Mach wave profile and slope of the precursor waves, but the elastic precursor velocity is too high. The high elastic wave speed was also observed in the multi-point VISAR experiment so this is not unexpected. Unfortunately, only the wave profiles were measured, as the dramatic loss of interferometer contrast after the arrival of the Mach reflection makes it impossible to extract the necessary time resolved particle velocity information (spatially resolved along a line).

In an attempt to remedy the loss of light in the previous experiment, the second shot, MW-O2 (weak confinement), utilized a sandblasted diffuse rear surface. As with the VISAR measurement, it is speculated that the shock arrival would turn a specular rear surface diffuse, so a diffuse surface would maintain contrast longer. As seen in the ORVIS image in Figure 5.7(a), the diffuse surface creates much more scatter in the initial fringes, but the overall features expected from the shock reflection are still captured. In this case, not only are the three shocks composing the Mach reflection evident but the Mach stem is much more pronounced and has a measurable curvature. The digitized image in 5.7(b) illustrates the predictive capabilities of both the simulations and the model. Once again, however, particle velocity information cannot be obtained due to the dramatic loss of contrast. As mentioned in Chapter 3 the collimating collection lens is located outside of the target chamber, approximately 1 m from the target. Thus, the reflected light has a relatively large distance to travel and slight perturbations in the target surface can cause extreme loss of the collected light intensity. A possible solution would be to use a disposable short focal length collection lens that is close to the target. Since the reflected light would have a much shorter distance to diffuse contrast might be obtained after the arrival in the shock resulting in the desired full field particle velocity.

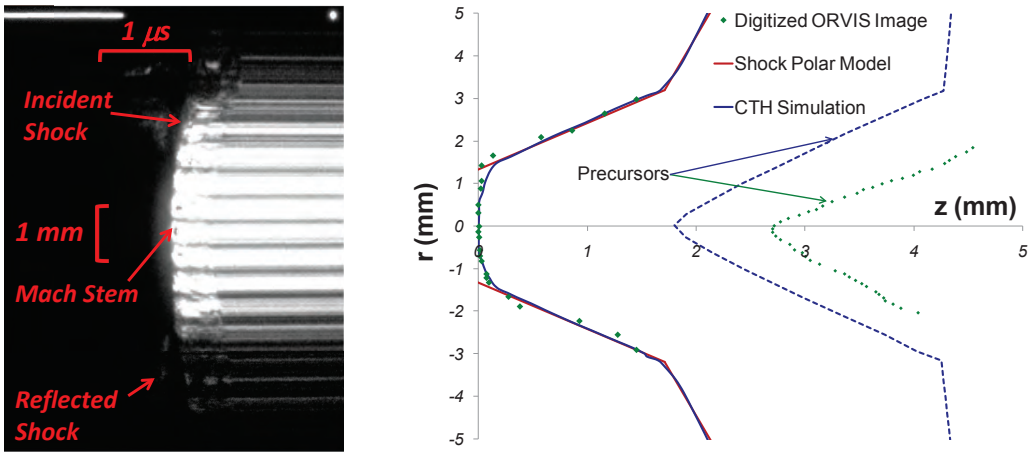

(a) (b)

Figure 5.7: Experimental results from MW-O2, molybdenum/copper target. The ORVIS streak camera image in (a) is digitized to produce the Mach configuration in (b). The experimental results in (b) are overlaid with the corresponding numerical simulation and shock polar analysis.

The reason for conducting the ORVIS experiments was, in addition to characterizing the spatial features of the profile, to make multiple Hugoniot measurements based on a single experiment. An interesting aspect of this experimental configuration is the inherent pressure gradient in the Mach reflection. Examining a shock polar such as in Figure 4.3(a) or Figure 4.4(b), for example, illustrates the range of pressures involved with the entire reflection. At the center of the target, the symmetry of the problem forces the oblique shock to be normal, so the peak pressure ($\theta = 0$) is achieved. A second known state is the lower bound on the pressure and is achieved at the interface between the two materials, at the point where the two shock polars intersect. Theoretically, then, the rest of the reflection produces continuous states between these two bounds, where the pressure at any point is directly related to the angle of the reflection through the shock polar equations. If, in an experiment, it was possible to measure the angle and peak particle velocity at each point along the reflection, it should be possible to obtain multiple Hugoniot points over a wide range of pressures in a single shot. This was the original intent of the ORVIS experiments, but quality full field particle velocity information has yet to be collected.

As an illustration of the idea, however, a synthetic ORVIS data set was produced from the numerical simulation for MW-V1. Given the predictive capabilities of the simulation, illustrated in Figure 5.1, these traces should be a reasonable approximation to the experiment. A coarse grating, 132 μm, was used as the spacing between measured points and was chosen as an extremely conservative estimate for an actual ORVIS measurement. The resulting synthetic data, shown in Figure 5.8(a), illustrates the free surface velocities obtained from the cylinder interface to the center of the target. Figure 5.8(b) illustrates two neighboring velocity traces along an oblique shock of angle,

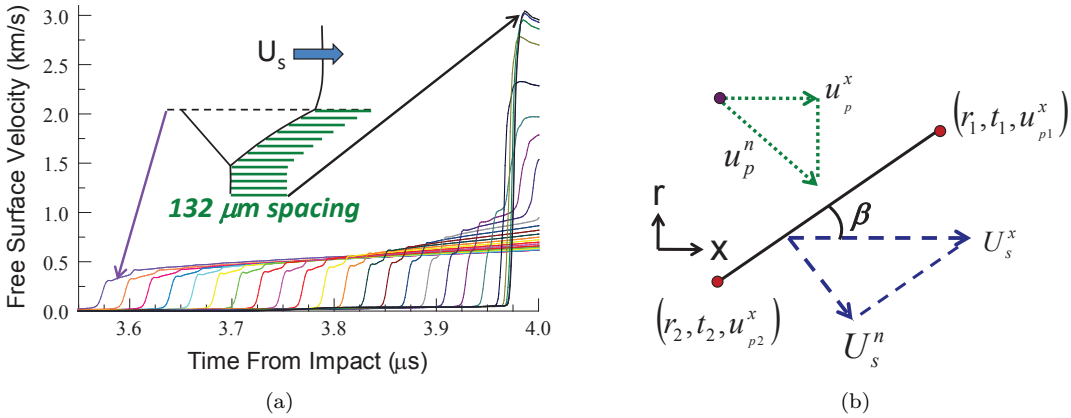

Figure 5.8: The synthetic ORVIS data set in (a) is taken from the MW-V1 numerical simulation. The components of the particle velocity and wave speed can be determined from a pair of velocity traces as illustrated in (b).

β. The information obtained from the ORVIS at each point is the radius, r, shock arrival time, t, and the peak axial component of the free surface particle velocity u_p^x . The instantaneous shock angle can be approximated through simple geometry by examining the position of each neighboring trace in relation to the relative lag between each arrival position as

$$\beta = tan^{-1}\left[\frac{r_2 - r_1}{U_s^x\,(t_2 - t_1)}\right], \tag{5.5}$$

where U_s^x is the apparent wave speed in the axial direction, which, in the steady state, is equal to the known shock velocity in the outer cylinder. Given the wave angle, the normal average in situ velocity and shock velocity can then be calculated as

$$U_s^n = U_s^x sin\beta, \tag{5.6}$$

$$u_p^n = \frac{u_{p1}^x + u_{p2}^x}{4sin\beta}, \tag{5.7}$$

where the extra factor of 2 in Eqn. 5.7 comes the usual free surface approximation. Equations 5.1 and 5.2 can now be used in conjunction with the appropriate component of the precursor velocity (if necessary) to calculate an average Hugoniot state for each pair of profiles. Working through this algorithm for the synthetic CTH simulation data set gives the Hugoniot points shown in Figure 5.9. Since the numerical simulation uses the copper Hugoniot as an input, the calculated points should lie directly on this curve. The scatter, then, gives an idea of the types of systematic errors associated with choosing the shock arrival times and particle velocities. The shock arrival times, in particular, are expected to contain some uncertainty due to the numerical viscosity in the simulation producing

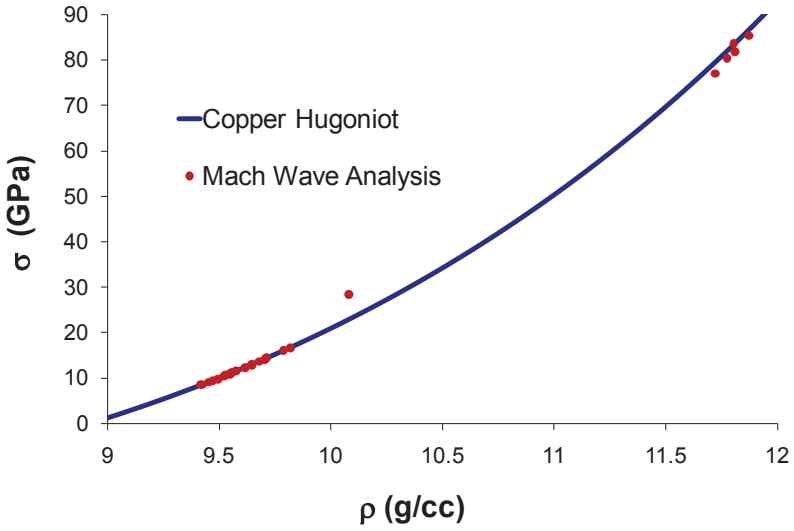

Figure 5.9: A calculation of multiple Hugoniot points using the synthetic data set shown in Figure 5.8(a) is compared to the copper Hugoniot used as input in the CTH simulations.

longer rise times. The experiments produce much sharper shocks and should provide even better results when working within this framework. A final remark will be made about the stray Hugoniot point located between the two distinct pressure regimes associated with the incident and Mach stem. This point was calculated using two profiles representing the transition between the two regimes, and, as shown in Figure 4.1, this transition is expected to be relatively sharp. As such, the coarse spacing of the selected traces was not enough to resolve the transition, producing an erroneous data point. The experiments should have better resolution, and proper selection of the outer material, as shown in Figure 4.4 can produce much more gradual transitions.

A further check of the methodology can be made by examining the multi-point VISAR experiments discussed previously and shown in Figures 5.1 and 5.3. These experiments can be viewed as an extremely coarse full field measurement and as shown in Figure 5.2, there does not appear to be a dramatic change in the incident shock strength between the probes monitoring the 2.69 mm and 1.35 mm locations. In MW-V1, for example, the shock arrival times are measured to be 3.627 and 3.825 μs while the initial particle velocities are given by 0.46 and 0.63 km/s, respectively. Equations 5.6 and 5.7 result in shock and particle velocities of 4.642 and 0.374 km/s, respectively. Similarly, the analysis can be applied to the three inner cylinder probes in MW-V2. As shown in Figure 5.10 the calculated stress and density states are in line with the majority of the lower pressure points calculated in Figure 5.9 and agree surprisingly well with the copper Hugoniot. This is further validation that it should be possible, with a good experimental ORVIS data set, to calculate the entire Hugoniot between the interface and Mach stem pressures in a single experiment.

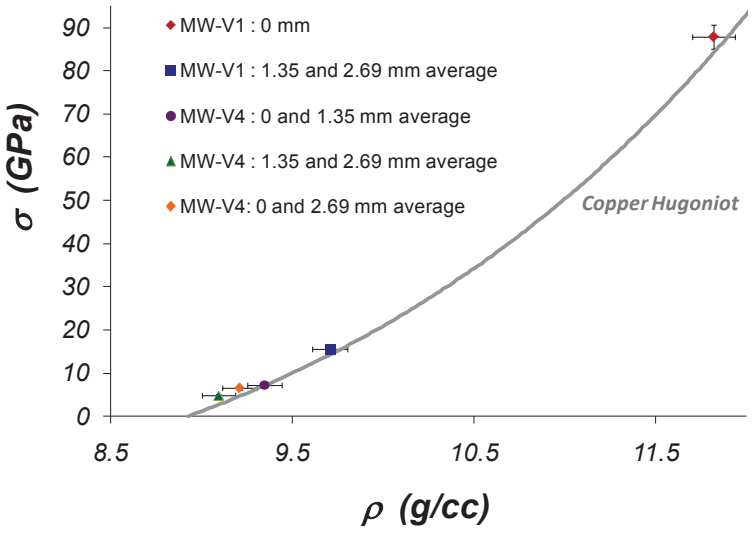

Figure 5.10: Two measured Hugoniot points from the MW-V1 experiment compared to the copper Hugoniot given in Table 4.1.

5.2 Iron Experiments

5.2.1 Plate Impact Shock Response

The velocity profile for an idealized material exhibiting a two-wave structure due to a phase transition is given in Figure 2.23. This structure was quantified in iron using a simple plate impact experiment in which a 4.8 mm thick steel flyer impacted a 6.2 mm thick steel target at 1.256 km/s. The diameter of the flyer and the target were 33.91 and 38.07 mm, respectively. Low carbon 1006 steel was used as a substitute for iron (only in this experiment) due to time and cost restrictions in obtaining pure iron and is not expected to have a significant impact on the bulk material properties. The VISAR profile obtained from the center of the rear free surface of the target is shown in Figure 5.11. Based on the time of arrival and the thickness of the target, the longitudinal elastic wave speed and first shock velocity are 6.25 km/s and 5.02 km/s, respectively, which are in line with what has been reported previously in the literature [14]. Similarly, the free surface particle velocity of the first phase (bcc, α), is measured to be 0.61 km/s, and the resulting stress of 12.25 GPa is also fairly consistent with the values previously reported [14]. The arrival of the second shock gives a velocity of 4.42 km/s and a free surface velocity of 1.19 km/s. Applying the two-wave analysis discussed in Section 5.1.1.3, a peak stress of 22.7 GPa is obtained after the second shock, completing the picture of the phase transition as it relates to Figure 2.23. An interesting feature observed in this waveform is what appears to be a third shock. This has also been observed in previous experiments [14] and is thought to be the result of the second shock reflecting off of the phase boundary.

A one dimensional numerical simulation with the same experimental parameters is also given in

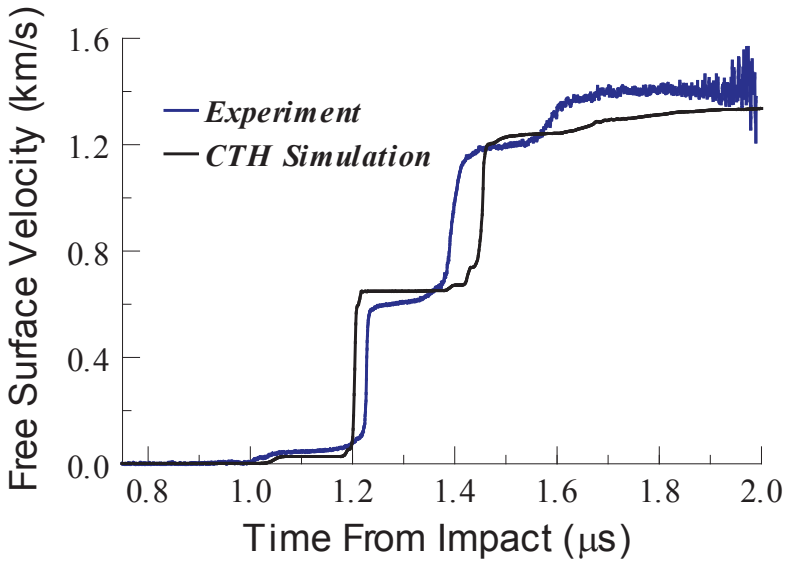

Figure 5.11: Experimental and simulated wave profiles for a symmetric iron (1006 steel) impact at 1.256 km/s.

Figure 5.11 that utilizes the multiphase iron EOS discussed in Chapter 4. As shown, the simulation is in reasonable agreement with the experiment except the phase transition is enforced to take place at 13 GPa, resulting in a slightly higher particle velocity and wave speed. This disagreement is thought to be due to the use of a mild steel rather than pure iron. Overall, however, it is expected that the multi-phase EOS is sufficient to capture the effects of this polymorphic phase transition in the Mach lens configuration.

5.2.2 Mach Lens Experiments

All of the experiments conducted on iron were performed using a single-point VISAR and dual-delay interferometers. The shot configurations and results are given in Table 5.3. The measured velocity

Table 5.3: Summary of Mach lens experiments on iron.

Exp. No.	Materials[a]	Thickness[b]	Diameter[c]	u_I	U_s^{outer}	u_{peak}	σ	ρ
		(mm)	(mm)	(km/s)	(km/s)	(km/s)	(GPa)	(g/cc)
MW-I1	Cu / Mo / Fe	6.817 / 14.265	38.33 / 3.216	1.190	5.762	0.55	-	-
MW-I2	Cu / Mo / Fe	6.815 / 14.242	38.15 / 3.218	1.310	5.825	2.40	54.1	9.943

[a] Impactor / outer cylinder / inner cylinder

[b] Impactor / target

[c] Outer cylinder / inner cylinder

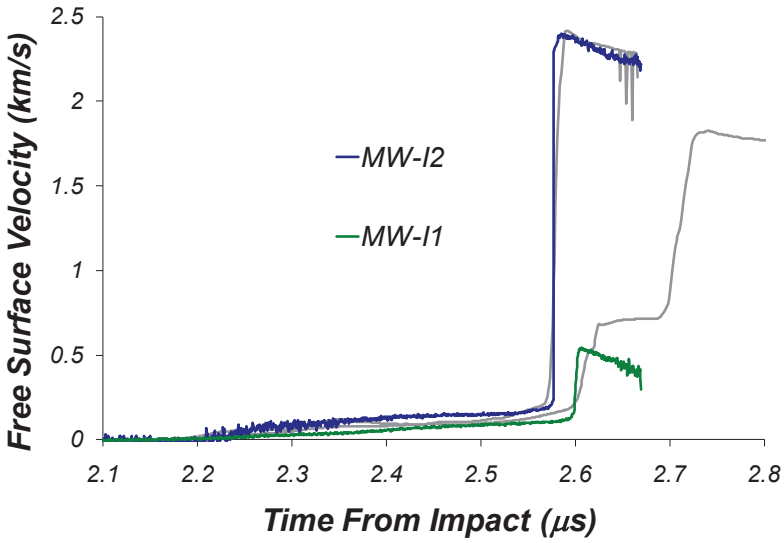

Figure 5.12: Measured free surface velocity profiles and the corresponding simulated wave profiles (given in gray) for the iron experiments.

profiles are plotted in Figure 5.12 along with the free surface tracers (at the center of the targets) from the corresponding numerical simulations shown in Figure 4.5. The numerical simulations agree with the measurements made in the experiments. In MW-I2, the measured material response is very similar to what was observed previously in the copper experiments with weak confinement. The precursor increases the velocity to just over 0.2 km/s before the shock drives the velocity up to the expected peak Hugoniot state. The non-quiescent shock analysis discussed previously results in the Hugoniot point given in Figure 5.13. As expected by the excellent agreement with the simulated profile, the measured shocked state falls right in line with measurements in the literature [62]. Further, the (ϵ phase) shock polar analysis predicts a free surface velocity of 2.49 km/s, which agrees well with the measured 2.40 km/s considering the presence of the precursor. Thus, it appears as though the measured profile contains no evidence of the phase transition and represents a typical Mach lens experiment. In this case, the the pressure gain of the system is 2, while the equivalent plate impact velocity is 2.3 km/s .

The MW-I1 experiment results in a dramatically different free surface velocity profile considering there is only a 1% decrease in the outer shock velocity from MW-I2. The peak free surface velocity, as verified by the dual-delay interferometers, is only 0.544 km/s. This is consistent with the first ($\alpha - \epsilon$ phase transition) shock seen in the simulations. Given an expected (normal) phase transition shock speed of 5.07 km/s [14] and the steady state axial wave speeds yields, through Eqn. 5.6, an oblique shock angle of 60.5°. Given a normal free surface phase transition velocity of 0.64 km/s [14], the expected axial component is 0.556 km/s, which is within 2.2% of the measured value. Considering the presence of the precursor this appears to be reasonable, and it is expected that measured profile

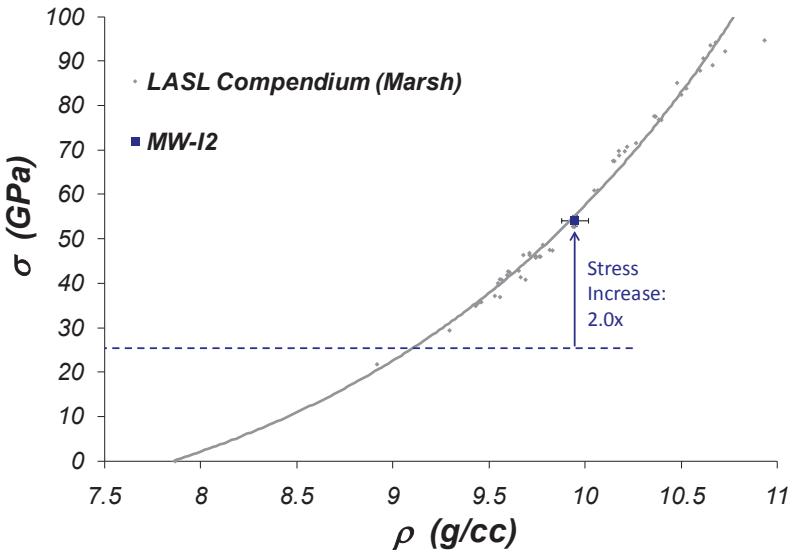

Figure 5.13: Shocked state measured in MW-I2 compared with iron Hugoniot data in the literature [62].

is indeed capturing the phase transition and then loses contrast prior to the arrival of the trailing Mach reflection. Given multiple VISAR points, as illustrated in the MW-V1 experiment, it should be possible to calculate the properties of a phase transition without any *a priori* knowledge.

Chapter 6

Summary and Future Work

6.1 Summary

In this dissertation, the feasibility of using a simple composite target to generate a steady Mach reflection and make high pressure Hugoniot measurements in solids is examined. The experimental configuration uses the planar impact between a homogeneous flyer plate and a target consisting of two concentric cylinders. When the shock speed in the well characterized outer cylinder exceeds that of the inner cylinder, converging shock waves and a subsequent steady Mach reflection results in a concentrated pressure state in the center of the target. This high pressure state provides a significant increase in shock strength over conventional one dimensional plane shock wave loading. In the steady state, the Mach reflection must be traveling at the same velocity as the far field shock in the outer cylinder, so an experiment only requires the measurement of one other property of the shock wave to calculate a point on the Hugoniot. In the experiments presented, a VISAR measurement of the free surface was found to provide the necessary resolution to estimate this shocked state. Additionally, the incident shock portion of the Mach reflection provides a continuous pressure gradient in the inner material between the interface with the outer cylinder and the Mach stem. One application of this feature is the ability to estimate large portions of the Hugoniot using a single full field measurement. Another may be the ability to detect phase transitions, which are traditionally difficult to measure with a plane shock. The main drawbacks of this technique the inability to use a window unless it is very well impedance matched. Thus, determination of the Hugoniot is generally restricted to more error prone free surface velocity measurements.

Chapter 2 summarizes the concepts required to understand the behavior of reflected shocks in both gases and solids. Traditionally, shock reflection problems in gas dynamics can be treated by solving the oblique shock relations for a perfect gas. Graphical solutions using shock polars often provide an intuitive view of the problem, particularly when regular reflection solutions are no longer possible. In the event of an irregular reflection, a Mach reflection can develop in which a three-shock configuration forms a viable solution. These types of reflection problems, however, are not unique to

the field of gas dynamics. It has long been recognized that shock waves can also be used to study the properties of solids at extreme temperatures and pressures. Often, shock loading results in pressures that are well in excess of the material shear strength and, hence, the delineating factor between fluids and solids is often ignored under these conditions. The treatment of shock compressed solids, however, is still generally approached from a solid mechanics perspective resulting in a Lagrangian treatment of the problem. In an effort to solve the shock reflection problems arising in the Mach lens configuration, the well developed analytic techniques used in gas dynamics are extended to the EOS commonly used in solids. The resulting shock polar analysis is shown to be in good agreement with previous researchers who examined the solution of shock reflection problems with both a Lagrangian analysis and numerical techniques. The polar analysis is then extended to solving the steady state Mach reflection problem. This solution illustrates the importance of the confining material in the configuration. In some cases an oblique shock in the outer material provides a sufficient solution to the problem. In other cases, an additional expansion wave is required to form a solution. The former case is referred to as the strong solution, while the latter is deemed the weak solution.

The experimental techniques used to study the Mach lens configuration are discussed in Chapter 3. Two powder gun systems are used to explosively launch projectiles to velocities of 2 km/s into the Mach lens assembly. The primary diagnostic used to monitor the resulting Mach wave is velocity interferometry. The VISAR diagnostic provides a point measurement of the free surface particle velocity with extremely high temporal resolution, while the ORVIS system is used in conjunction with a streak camera to provide high resolution in both space and time. The materials of interest chosen for the validation of the technique are copper and iron. Copper is a well studied material with moderate shock speeds and an impedance that can be easily bracketed by other common materials. Iron was selected as ideal phase transforming material because the shock properties are similar to copper and the polymorphic phase transition has been well characterized. Aluminum is an excellent material for use as an outer cylinder because of the high wave speed and low impedance, which will result in a strong confinement solution and high Mach reflection pressures. Molybdenum was chosen as a second confining material because it also results in relatively high shock speeds, but also provides an example of a weak confinement solution. For these material combinations, the Mach lens target must then be designed such that the length allows for the steady solution to be reached while avoiding any influence of the edge release wave on the experiment. Thus, the inner cylinder must large enough to make useful measurements, but small enough to satisfy the previous criteria. It was found that a target length to inner cylinder diameter (L/D) ratio of 2.5 to 4.5 (depending on the materials and loading conditions) is sufficient to satisfy these conditions. For the systems discussed in this thesis an L/D of 5 is suggested to provide a conservative rule-of-thumb for design.

Further insights into the reflections produced by the Mach lens configuration were obtained through the use of the numerical simulations discussed in Chapter 4. The CTH hydrocode is used

in conjunction with a Mie-Grüneisen EOS to model the hydrodynamic response of the system. The deviatoric stresses are accounted for through the rate-dependent Steinburg-Guinan-Lund strength model. The simulations are shown to do a reasonable job at not only predicting the wave profiles but also the geometric features of the reflection, specifically the length and curvature of the Mach stem. The simulations are shown to be in good agreement with the analytical analysis given by the shock polars. In particular, the different behaviors of the strong and weak confinement cases suggest the correct physics is captured in both the simulations and the model. Further, the simulations can be extended to view the complex reflection phenomena involved when the inner material experiences a phase transition. It appears the Mach lens configuration provides a greater sensitivity to phase transitions than traditional one dimensional experiments. This sensitivity may provide the means to detect phase transitions that are often difficult or impossible to measure experimentally using more conventional approaches.

The experimental validation of the technique is presented in Chapter 5. A key concept in this technique is that the speed of the Mach wave is essentially obtained for free. If the Mach reflection is in the steady state regime, it must be traveling at the same axial speed as the far field shock in the outer cylinder. Thus, a measurement of the projectile velocity along with the known Hugoniots for the impactor and outer cylinder materials allows for the calculation of the shock speed via impedance matching. Since the shock speed is known, the experiments require only a single measurement of another parameter of the shock wave. While it may be possible to use in situ gauges to measure the particle velocity or stress, or x-rays to estimate the density, non-invasive optical techniques were chosen as the most versatile and accurate method of characterizing the Hugoniot state. Specifically, the VISAR and ORVIS techniques were used as they have a history of providing high quality data in shock compression experiments. Multi-point VISAR experiments are used to characterize the free surface velocity of the copper inner cylinder at various radii. These experimental measurements are shown to be in excellent agreement with both numerical simulations and the analytic shock polar model. Further experiments were conducted using a single VISAR measurement at the center of the rear surface to calculate high pressure Hugoniot states. The symmetry of the configuration forces the Mach stem to be normal at the center of the cylinder, so the VISAR measurement is a direct measure of the free surface velocity associated with a plane wave traveling at the shock speed of the outer cylinder. Using a free surface approximation, the particle velocity can be estimated and a standard Lagrangian analysis can be used to calculate the stress and density associated with the shock. Initial experiments show excellent agreement between the measured shocked state and Hugoniot data available in the literature. The value of the Mach wave configuration can be further extended to making multiple Hugoniot measurements. Since the incident shock of the reflection must provide a continuous pressure gradient connecting the interface and Mach stem pressures, a full field measurement of the particle velocities associated with the entire reflection provides enough

information to characterize the entire Hugoniot between these pressures. In an attempt to verify this concept, the ORVIS diagnostic was used to characterize the free surface velocity of a line across the center of the target. Unfortunately, while the diagnostic captures the arrival of the Mach reflection well, the system is unable to maintain contrast through the shock and obtain the necessary particle velocity information. Experiments were also performed using an iron cylinder where the existence of the expected $\alpha - \epsilon$ phase transition is verified, illustrating the phase transition detecting capabilities of the system.

6.2 Future Work

6.2.1 Measuring the Hugoniot in a Single Experiment

The framework for measuring a large portion of the Hugoniot curve in a single experiment was laid out in Section 5.1.2. Unfortunately, the ORVIS diagnostic did not work as intended and particle velocity information was not obtained. However, as illustrated in the VISAR experiments it is possible to make velocity measurements, so modifications to the ORVIS system could solve this issue. Typically, ORVIS has been shown to work very well with a specular surface viewed through a window [80]. Unfortunately, a window could only be used in the case of a perfect impedance match, which is generally not possible with copper. As suggested in Section 5.1.2, however, the use of a collection lens very close to the target might also solve this problem.

It is also desirable to have small gradients in the curvature of the wavefront between the Mach stem and incident shock regimes. As shown in Chapter 4, one way to control the shape of the Mach reflection is to vary the outer cylinder. Strong confinement using an aluminum cylinder (Figure 4.3) produces a very distinct Mach reflection where, as shown in Figure 5.9, it is difficult to measure the states between the Mach stem and incident shock. The weak confinement using molybdenum, on the other hand, produces a much more gradual transition. As another example of applying the methodology to a synthetic CTH data set, the simulation of the MW-O2 experiment, shown in Figure 5.7(b), is used to produce free surface velocity profiles along the center of the inner cylinder with a radial spacing of 98 μm . As described in Section 5.1.2 this is not an unreasonable resolution to expect in an ORVIS experiments. The velocity profiles along with the Hugoniot points obtained from the traces with Eqns. 5.1-5.7 are shown in Figure 6.1. As illustrated in Figure 6.1(b), the resulting calculated shocked states not only agree well with the input Hugoniot, but also capture a large range of the pressures. It is not unreasonable to believe a single high quality ORVIS experiment using this configuration could result in the measurement of the copper Hugoniot from 10-60 GPa. Over 70 individual experiments were conducted in the literature to accomplish this same task [62].

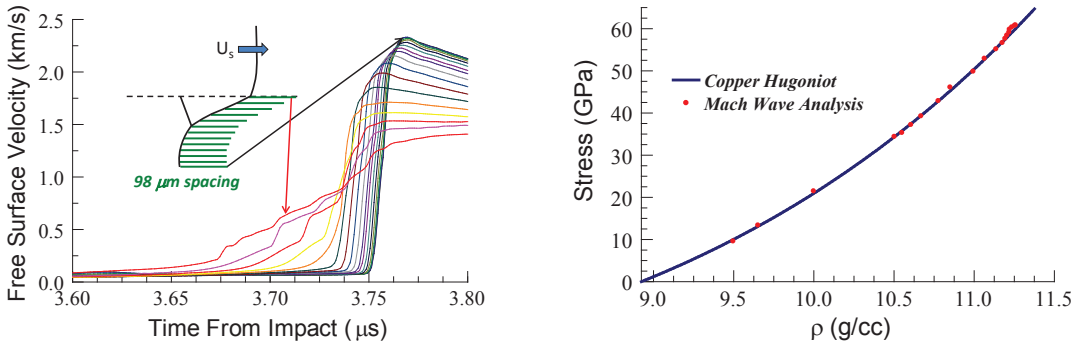

(a) (b)

Figure 6.1: The synthetic ORVIS data set in (a) is taken from the CTH simulation of MW-O2. The Hugoniot points shown in (b) are calculated from neighboring pairs of the free surface velocity profiles.

6.2.2 Extension to Alternative Loading Methods and Higher Pressures

The validation of the Mach lens technique in this thesis was performed using mechanical loading driven by an explosively launched projectile. There is nothing in the physics, however, that restricts the technique to this type of loading. Given the simplicity of the composite target, it should be straightforward to use the methodology to extend the pressure ranges that can be accessed in other experimental systems. The only requirement of the system is that a plane shock is introduced at the front of the target. Thus, the Mach lens target can easily be implemented with explosively driven devices such as plane-wave generators or accelerated flyer plates [65], two-stage gun systems [34], magnetic loading [28, 57], or laser shock loading [71].

As an immediate and most accessible example, consider extending the copper Hugoniot to pressures beyond the current state of the art. Available data in the literature provides measurements up to 330 GPa [66, 62] using a two-stage gun and plate impact techniques. The two-stage gun at the STAR facility at the Sandia National Laboratories is capable of launching a 15 g projectile to velocities of ~ 6 km/s [8]. The diameter of the flyer is 27 mm, so launching a 3 mm thick copper flyer to this velocity is not unreasonable. As discussed in Section 3.3.1, beryllium is an ideal choice for obtaining high gains in the system and was selected as the outer material. A copper inner cylinder diameter of 3.2 mm was selected with an L/D of 5 to give a target length of 15 mm. The results of the CTH simulation with this configuration along with the corresponding shock polar analysis are given in Figure 6.2. The shock polar analysis uses the copper Hugoniot shown in Table 4.1, which must be extrapolated to the higher pressures examined in this example. The beryllium Hugoniot is given by $\rho_0 = 1.850$ g/cc , $c_0 = 7.92$ km/s, $s = 1.124$, and γ_0=1.19 [62]. The CTH simulation utilized the built-in SESAME tabular form of the EOS for all of the materials [54]. These tables are based largely on theoretical quantum mechanics calculations and are generally in good agreement

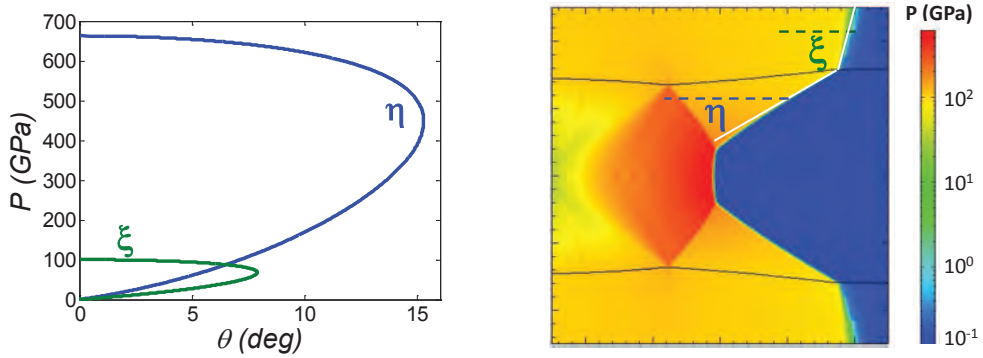

(a) (b)

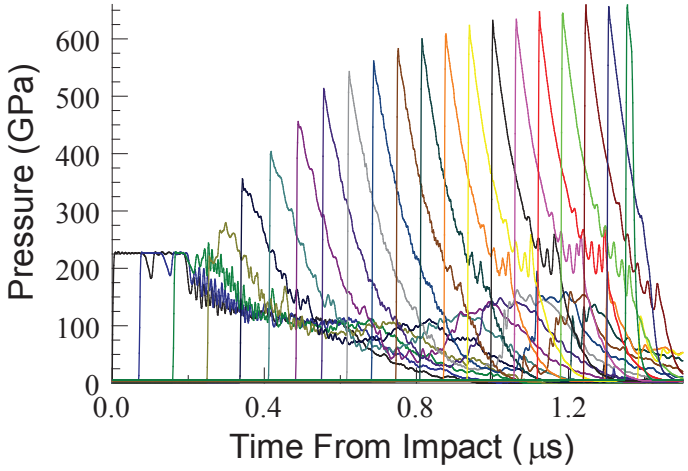

(c)

Figure 6.2: CTH simulation of copper impacting a beryllium/copper Mach lens at 6 km/s. The shock polar analysis in (a) produces the angles overlaid with the simulated pressure contours in (b). The pressure profile of 20 equally spaced points (in the longitudinal direction) along the centerline of the copper inner cylinder is given in (c).

with the experimental Hugoniot where available. Therefore, the simulation is expected to capture much of the physics even though experimental data does not currently exist in the high pressures associated with the Mach stem.

As shown in Figure 6.2, the results of the simulation agree extremely well with what is predicted from the shock polar analysis. Not only do the predicted angles in Figure 6.2(b) match, but the steady state peak pressure from the simulation, shown in Figure 6.2(c), is also in line with what is obtained by simply extrapolating the Hugoniots used to generate the shock polars (Figure 6.2(a)). The peak pressure in the simulations is 654 GPa which is within 2% of the shock polar calculated 663 GPa. A comparison with the equivalent plate impact pressure (symmetric copper impact at 6 km/s) of pressure 225 GPa shows a multiplication in pressure of nearly 3 times. Thus, it appears the techniques developed in this dissertation scale well to extreme impact velocities and can dramatically

increase the capabilities of the classic tools currently used in shock compression experiments.

6.2.3 Combined Pressure-Shear Measurements Using Oblique Shocks

The oblique plate impact experiment is a method used to generate combined pressure and shear waves in a well controlled plane shock wave experiment [1]. A cartoon of the experimental configuration is shown in Figure 6.3(a). In these experiments, a slotted gun barrel is used to orient an inclined impactor such that it impacts a target at a matching angle of obliquity. The inclination of the plates relative to the direction of motion of the projectile results in both pressure and shear waves in the target. Of particular interest in these experiments is evaluating the strength of the material in the shocked state. The longitudinal shock will drive the material to the appropriate Hugoniot state, while the transverse wave can be used to infer the properties of the yield surface at the shocked pressure. In practice, the properties of the waves are most often examined using techniques that can extract both transverse and longitudinal particle motion. Initial experiments were conducted using normal and transverse displacement interferometry techniques [1, 56]. More recent work has been conducted using VISAR at inclined angles to the interface to infer the necessary time resolved normal and shear particle velocities [29, 6]. The longitudinal and shear stresses, σ and τ, respectively, are given by

$$\sigma = \rho_0 C_l^p u_p^l, \tag{6.1}$$

$$\tau = \rho_h C_s^p u_p^s, \tag{6.2}$$

where ρ_h is the density due to the compression of the longitudinal shock, C_l^p and C_s^p are the longitudinal and shear plastic wave speeds, and u_p^l and u_p^s are the corresponding longitudinal and shear particle velocities, respectively.

The oblique shock analysis presented in Section 2.2.4 illustrates a consistent and accurate method of characterizing the reflection angles arising from the interaction of a plane shock wave with an inclined interface. Thus, if the transmitted shock angle between two inclined materials can be predicted, the experiment can be constructed to measure the resulting transverse and longitudinal particle motion. An idea of a possible experimental setup is illustrated in Figure 6.3(b). In this configuration, aluminum was chosen as the material of interest because most of the pressure-shear experimental work in the literature involves measurements on this material [1, 56, 6]. Beryllium was chosen as the driver material, and, as shown, a symmetric impact is used to create a plane shock in the driver material. When the plane shock encounters the inclined interface between the beryllium and aluminum, reflected and transmitted oblique shocks are generated that can be described by the analysis presented in Section 2.2.4. Based on this analysis, the rear surface of the target can be

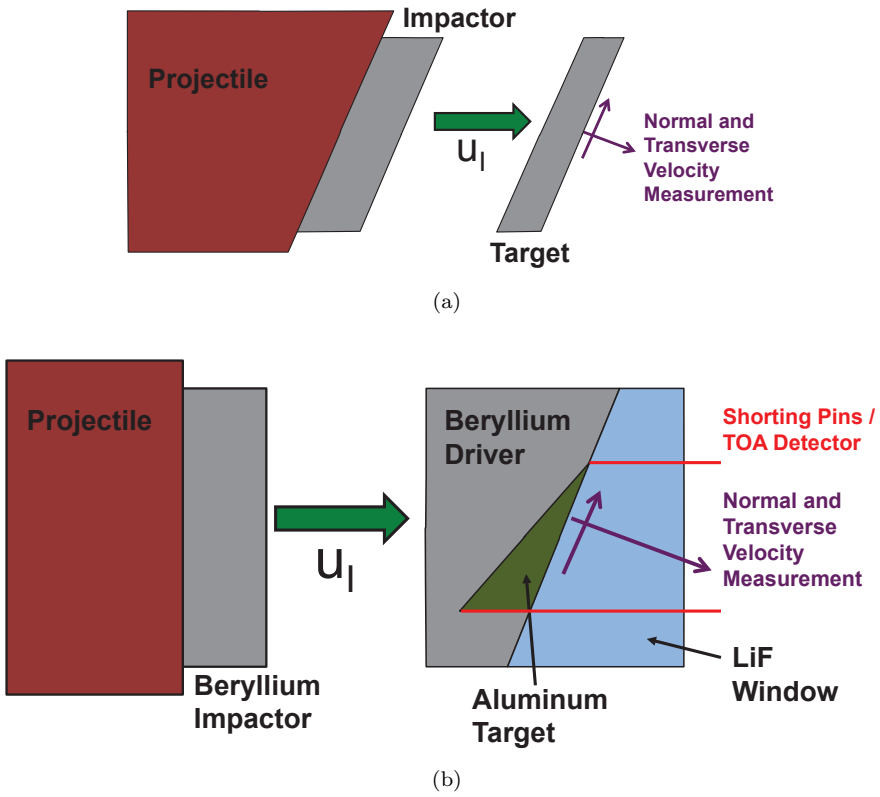

Figure 6.3: Pressure-shear wave generation using (a) conventional oblique impact configuration and (b) a possible oblique shock wave experiment.

designed to match the angle of the transmitted shock ensuring any longitudinal and shear particle velocity measurements are not corrupted by the transmitted shock interacting with an inclined interface. In this particular example, a lithium-fluoride window is used to back the aluminum. Lithium-fluoride is very well impedance matched to aluminum, so any reflections at this interface should be negligible. As a result, VISAR can be used to view through the window and monitor the in situ particle velocities at this interface. Shorting pins or some other form of time of arrival detector can be used to monitor the oblique shock arrival at set points along the aluminum/beryllium interface. These arrival times, in conjunction with the velocity interferometry measurements, can then be used to infer the transit time of the shear and longitudinal waves through that particular thickness of the aluminum target so that Eqns. 6.1 and 6.2 can be used to infer the strength of the aluminum.

A CTH simulation was constructed using the setup shown in Figure 6.3(b). In this example, the impact velocity is 1 km/s , the angle of inclination at the beryllium/aluminum interface is 10°, and the equations of state implemented are the same as those discussed in Section 6.2.2. A 2-D rectangular geometry was used with a mesh size containing ~ 100 cells across the length of the

aluminum target. The resulting transmitted and reflected shock angles, determined by the shock polar analysis shown in Figure 6.4(a), are 7.05 and 9.36°, respectively. Using these angles, the CTH simulation was oriented such that transmitted shock would only contain longitudinal components of velocity (in the simulation's coordinate system). In other words, the simulation was rotated such that the tracer particle would correspond to what a normal and shear interferometry system would measure. The pressure contours from the simulation are plotted in Figure 6.4(b) and, as shown, the transmitted shock angle is predicted extremely well. A tracer particle at the center of aluminum/window interface produces the longitudinal and shear velocities shown in Figure 6.4(c). These profiles are shifted in time such that t=0 corresponds to the interface shock arrival at the height of the tracer location. The average arrival times of the waves (shown as the vertical dotted lines in Figure 6.4(c)) are 0.173 μs and 0.340 μs. These waves travel a distance of 1.048 mm at this height, so the arrival times correspond to longitudinal and shear wave speeds of 6.058 and 3.082 km/s. The shock velocity based on the polar analysis is 6.0 km/s and the ultrasonic shear wave speed of 6061-T6 aluminum is 3.14 km/s, so these results are in good agreement with expected values. The peak longitudinal and transverse velocities are shown as the horizontal dashed lines in Figure 6.4(c) and correspond to 0.484 and 0.024 km/s, respectively. Application of Eqns. 6.1 and 6.2 result in a calculated longitudinal stress of 7.93 GPa and a peak shear stress of 0.22 GPa. Examining a tracer inside of the aluminum target results in the stress profiles shown in Figure 6.4(d). The average shocked stresses of these profiles (σ_x and σ_y) are 7.90 and 7.47 GPa. Assuming a Tresca yield criteria ($\sigma_x - \sigma_y = 2\tau$) the shear stress in the Hugoniot state predicted by the simulation is 0.215 GPa, which agrees extremely well with the value inferred through "measurements" of the longitudinal and transverse velocities. Thus, ignoring the experimental difficulties associated with glue bonds, friction, and errors due to tilt (both at the impact and measurement faces) the technique seems viable and could provide a method for evaluating strength at the very high pressures of interest to the shock physics community.

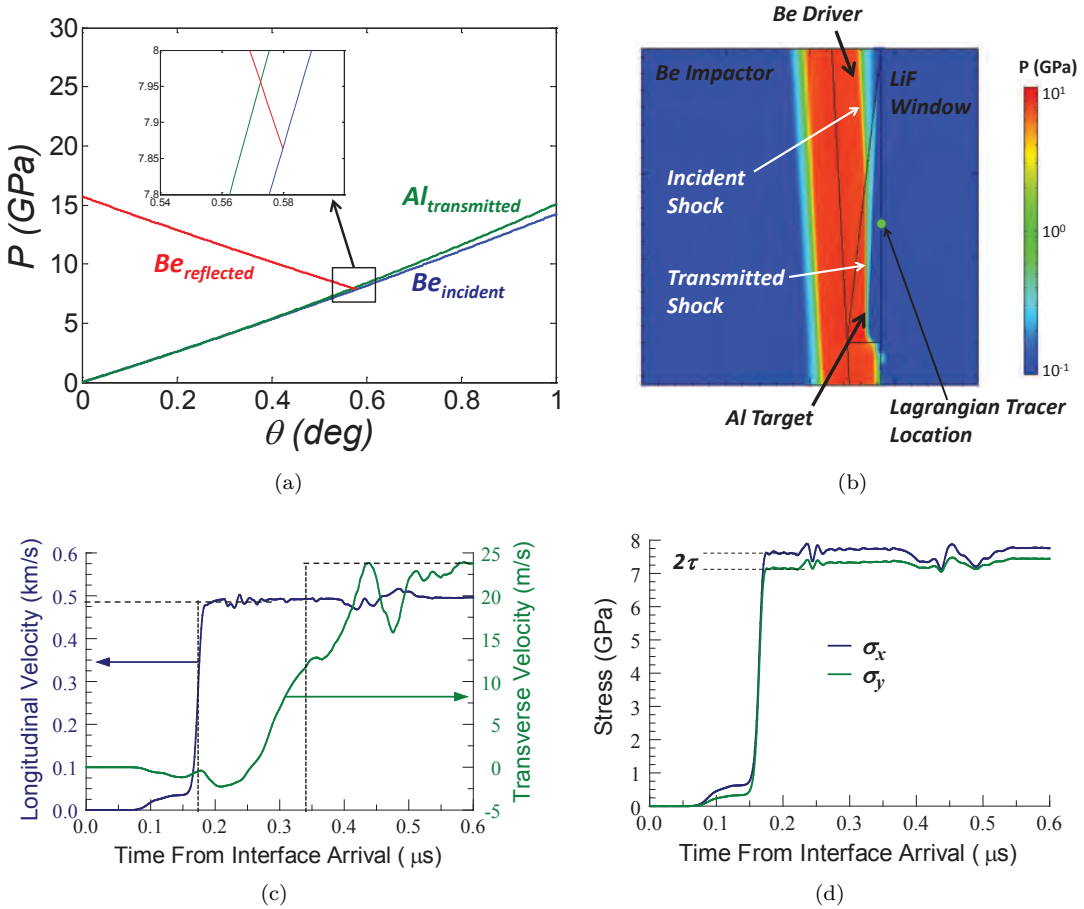

Figure 6.4: Theoretical pressure-shear configuration using beryllium to transmit an oblique shock wave into aluminum using a 10° angle of inclination. The initial shock is generated with a symmetric impact at 1 km/s and a lithium-fluoride window is used to monitor the in situ particle motion in the aluminum. The shock polar analysis in (a) is in good agreement with a plot of the simulated pressure contours in (b). Tracer particles are used to monitor the longitudinal and transverse particle velocities in (c) for comparison with the strength calculated by the simulated stresses shown in (d).

Appendix A

Uncertainty Quantification

The propagation of uncertainty of a measured quantity into inferred values can be estimated through the root-sum-squared uncertainty analysis. For the general case where an experimental result, R , is represented by a function, f, of x_N measured quantities

$$R = f\left(x_1, x_2, ..., x_N\right), \tag{A.1}$$

and the uncertainty in each measured parameter is given by δ_i such that

$$x_i = x_{measured,i} \pm \delta_i, \tag{A.2}$$

the uncertainty in R may be calculated as [32]

$$\delta_R^2 = \left(\frac{\partial f}{\partial x_1}\delta_1\right)^2 + \left(\frac{\partial f}{\partial x_2}\delta_2\right)^2 + ... + \left(\frac{\partial f}{\partial x_N}\delta_N\right)^2. \tag{A.3}$$

For relatively simple data reduction processes it is possible to calculate these derivatives analytically, and the uncertainty can be calculated directly, as will be demonstrated in the subsequent sections. For even modestly more complicated processes, such as that described in Eqn. 2.38, it becomes much more useful to use a perturbation method to estimate the error. From the fundamental theorem of calculus and for small uncertainties, the perturbation in the data due the measured quantity may be estimated by

$$\frac{\partial f}{\partial x_i}\delta_i = \lim_{\delta_i \to 0}\left[\frac{f\left(x_i + \delta_i\right) - f\left(x_i\right)}{\delta_i}\right]\delta_i \approx \left[f\left(x_i + \delta_i\right) - f\left(x_i\right)\right] = D_i. \tag{A.4}$$

Thus, to first order, Eqn. A.3 , may be approximated by

$$\delta_R^2 \approx D_1^2 + D_2^2 + ... + D_N^2. \tag{A.5}$$

A.1 Impedance Matching

Since the velocity of the steady Mach wave is calculated from the impact velocity and the known Hugoniots of the impactor and outer cylinder materials, the uncertainty in this velocity calculation depends on the precision of the respective data sets. Assuming a linear approximation (Eqn. 2.45) to the Hugoniot, the shock velocity can be calculated through Eqns. 2.46 and 2.45 showing

$$U_s = f\left(u_I, C_o^A, s^A, C_0^B, s^B\right), \tag{A.6}$$

and through Eqn. A.5

$$\begin{aligned}\delta_{U_s}^2 = &\left[f\left(u_I + \delta_{u_I}, C_o^A, s^A, C_0^B, s^B\right) - U_s\right]^2 + \left[f\left(u_I, C_o^A + \delta_{C_0^A}, s^A, C_0^B, s^B\right) - U_s\right]^2 + ... \\ &+ \left[f\left(u_I, C_o^A, s^A, C_0^B, s^B + \delta_{s^B}\right) - U_s\right]^2.\end{aligned} \tag{A.7}$$

The impactor velocity is measured by monitoring the time it takes the projectile to interrupt two light diodes of known separation

$$u_I = \frac{\Delta x}{\triangle t}. \tag{A.8}$$

Eqn. A.3 can be evaluated directly to show

$$\left(\frac{\delta u_I}{u_I}\right)^2 = \left(\frac{\delta \triangle x}{\triangle x}\right)^2 + \left(\frac{\delta \triangle t}{\triangle t}\right)^2. \tag{A.9}$$

The gap distance is estimated to be within $\pm 0.25\ mm$ and the time resolution to $\pm 0.05\ \mu s$, meaning errors in the velocity measurement are generally within 1% . To find the uncertainties associated with the Hugoniot data, a regression analysis can be performed. The best fit for the data is taken to be the line that minimizes the sum of the squared residuals, denoted Λ , and may be formulated as

$$\min_{C_0, s} \sum_{i=1}^{N} \left(U_{s_i} - C_0 - s u_{p_i}\right)^2 = \min_{c_0, s} \Lambda. \tag{A.10}$$

The solution to this least squares problem can be found by taking the appropriate derivatives

$$\frac{\partial \Lambda}{\partial C_0} = -2\left(\sum_{i=1}^{N} U_{s_i} - N C_0 - s \sum_{i=1}^{N} u_{p_i}\right) = 0, \tag{A.11}$$

$$\frac{\partial \Lambda}{\partial s} = -2\left(\sum_{i=1}^{N} u_{p_i} U_{s_i} - C_0 \sum_{i=1}^{N} u_{p_i} - s \sum_{i=1}^{N} u_{p_i}^2\right) = 0, \tag{A.12}$$

and solving for c_0 and s , giving

$$C_0 = \frac{\sum_{i=1}^{N} u_{p_i}^2 \sum_{i=1}^{N} U_{s_i} - \sum_{i=1}^{N} u_{p_i} \sum_{i=1}^{N} U_{s_i} u_{p_i}}{N \sum_{i=1}^{N} u_{p_i}^2 - \left(\sum_{i=1}^{N} u_{p_i}\right)^2}, \tag{A.13}$$

$$s = \frac{N \sum U_{s_i} u_{p_i} - \sum_{i=1}^{N} U_{s_i} \sum_{i=1}^{N} u_{p_i}}{N \sum_{i=1}^{N} u_{p_i}^2 - \left(\sum_{i=1}^{N} u_{p_i}\right)^2}. \tag{A.14}$$

The standard error of this regression is given by the definition of the standard deviation, denoted S, as

$$S_{U_s} = \left[\frac{\sum_{i=1}^{N} \left(U_{s_i} - C_0 - s u_{p_i}\right)^2}{N-2}\right]^{\frac{1}{2}}, \tag{A.15}$$

where the extra subtracted factor of 2 arises because two degrees of freedom were lost from the data set once the fit constants c_0 and s were determined. Finally, assuming the variance in u_p is negligible, the standard deviations of c_0 and s can be determined by taking the variance of Eqns. A.13 and A.14 and simplifying to show

$$S_s = \frac{S_{U_s}}{\sqrt{\sum_{i=1}^{N} \left(u_{p_i} - \bar{u}_{p_i}\right)^2}}, \tag{A.16}$$

$$S_{C_0} = S_s \sqrt{\frac{\sum_{i=1}^{N} u_{p_i}^2}{N}}, \tag{A.17}$$

where $\bar{u}_{p_i}$ is the mean of the particle velocity data set. The analysis was performed on the materials of interest, the results of which are shown in Table A.1. The reported uncertainties are taken to be twice the standard deviations calculated in Eqns. A.16 and A.17, giving a 95% confidence interval. The parameters in Table A.1 can now be used in conjunction with the measured projectile velocity to estimate the uncertainty in the calculated shock velocity based on the linear perturbation shown in Eqn. A.7.

A.2 VISAR Velocity Precision

A.2.1 Free Surface Measurement

Typically, the VISAR fringe-velocity relation, Eqn. 3.17, is written as

$$u\left(t - \frac{\tau}{2}\right) = KF\left(t\right), \tag{A.18}$$

Table A.1: Parameters obtained from the linear regression analysis on Hugoniot data in the literature [62]. Uncertainties in the empirical coefficients are 2 standard deviations, and 0.2% is estimated to be the uncertainty in the density.

Material	ρ_0 (g/cm^3)	C_0 (km/s)	s
Copper	8.924 ± 0.018	3.912 ± 0.044	1.508 ± 0.013
6061-T6 Aluminum	2.703 ± 0.005	5.332 ± 0.047	1.344 ± 0.021
Molybdenum	10.208 ± 0.020	5.137 ± 0.063	1.22 ± 0.021
Iron	7.856 ± 0.016	3.745 ± 0.085	1.676 ± 0.023

where K is a constant containing information about the wavelength of laser light, interferometer delay, and any dispersion corrections for a given VISAR system. The uncertainty in velocity can easily be determined with Eqn. A.3 as

$$\left(\frac{\delta u}{u}\right)^2 = \left(\frac{K}{u}\delta F\right)^2 + \left(\frac{\delta K}{K}\right)^2. \tag{A.19}$$

For a VISAR calibrated with white light interferometry, the time delay is generally known to within 0.1% and accounting for uncertainties in dispersion, $\frac{\delta K}{K}$ will be to be taken to be on the order of 0.005 [37]. The limit on the resolution of a fringe can be calculated by considering a VISAR with perfect quadrature. For an 8-bit acquisition, 1 part in 256 can be resolved, and over a perfect circle,

$$\delta F \geq \frac{1}{2\pi \cdot 256} \approx 0.0006. \tag{A.20}$$

In practice, however, uncertainties in the polarization put δF on the order of 0.01 [37]. Thus, for $K \approx u$, the uncertainty in the measurement is on the order of the fringe uncertainty, about 1%. If the fringe constant is much larger than the velocity, the uncertainty in the measurement increases significantly, but eliminates fringe ambiguity. On the other hand, decreasing the fringe constant results in a more precise measurement at the cost of having to add fringes to the shock jump. This reiterates the importance of using the dual-delay VISAR setup, as fringe ambiguities can be resolved with the large contrast system, while optimum velocity resolution is obtained in the small contrast interferometer.

A.2.2 Particle Velocity Approximation

The analysis in the experiments makes use of the free surface approximation, in which the in situ particle velocity is taken to be half of the measured free surface velocity. Clearly, the nonlinear nature of the wave propagation means this approximation is, strictly speaking, incorrect, and hence a systematic error has been introduced into the analysis. To evaluate the error introduced by this

approximation, a better estimate to the in situ particle velocity can be calculated using the Mie-Grüneisen EOS. As discussed previously, the traction-free boundary condition at the free surface necessitates the need for an isentropic release wave to propagate back into the previously shocked material, bringing the stress to 0. This is represented thermodynamically in Figure 2.8 where the isentrope centered on the shock stated is generated with Eqn. 2.57. The particle velocity corresponding to $\sigma = 0$ is the free surface velocity measured by the VISAR. Thus, iteration of the selected shock state until the appropriate free surface velocity is obtained yields the actual in situ velocity and gives an estimate to the systematic error, δu_p^s. The total uncertainty is the sum of the experimental and systematic errors and may be written as

$$u_p = \frac{1}{2}\left(u_{fs} \pm \delta u_{fs}\right) \pm \delta u_p^s. \tag{A.21}$$

For copper, at the stresses examined in these experiments, these errors are relatively small. For the parameters given in Table A.1 $\frac{\delta u_p^s}{u_p}$ is 0.65%, 1.8%, and 3.0% for shock stresses of 50, 100, and 150 GPa , respectively.

A.3 Experimental Uncertainties

The two primary measurements made in these experiments for the calculation of the Hugoniot state are the impactor velocity and the peak particle velocity measured by the VISAR. The speed of the Mach wave is calculated through impedance matching and as illustrated in Section A.1, the error associated with this calculation can be estimated through the uncertainty in the impact velocity and a quantification of how good the Hugoniot data used to characterize the impactor and outer material is. Similarly, the uncertainty in the measured particle velocity is given by Eqn. A.21. The propagation of these uncertainties into the calculated stress and density can be estimated by applying the linear linear perturbation (Eqn. A.5) to Eqns. 5.1 and 5.2. The uncertainties calculated for the experiments using this methodology are shown in Table A.2.

Table A.2: Summary of uncertainties calculated in the Mach lens experiments

Exp. No.	u_I (km/s)	U_s^{outer} (km/s)	u_{peak} (km/s)	σ (GPa)	ρ (g/cc)
MW-V1	1.558±0.010	6.379±0.180	3.10±0.05	87.91±2.85	11.818±0.124
MW-V2	1.140±0.007	6.398±0.052	3.34±0.05	95.35±1.72	12.076±0.085
MW-V3	1.401±0.009	6.546±0.095	3.44±0.08	100.63±2.01	12.112±0.092
MW-V4	1.310±0.008	6.414±0.093	3.28±0.08	94.32±1.87	12.009±0.088
MW-V6	1.826±0.012	6.057±0.066	2.77±0.04	73.72±1.35	11.652±0.070
MW-V7	1.446±0.009	5.568±0.063	1.84±0.02	44.63±0.65	10.757±0.041
MW-V8	1.314±0.008	5.782±0.064	2.33±0.03	59.61±0.94	11.210±0.053
MW-V9	1.043±0.007	5.641±0.063	2.06±0.02	50.99±0.82	10.982±0.048
MW-I2	1.310±0.008	5.825±0.064	2.40±0.03	54.10±1.21	9.943±0.068

Bibliography

[1] A.S. Abou-Sayed, R.J. Clifton, and L. Hermann. The Oblique-plate Impact Experiment. *Experimental Mechanics*, 16(4), 1976.

[2] G.A. Adadurov, A.N. Dremin, and G.I. Kanel. Mach reflection parameters for plexiglass cylinders. *ZPMTF*, 10(2):126–128, 1969.

[3] G.A. Adadurov, A.N. Dremin, G.I. Kanel, and S.V. Pershin. Determination of the shock wave parameters in materals preserved in cylindrical bombs. *FGV*, 3(2):281–285, 1967.

[4] T.J. Ahrens, K.G. Holland, and G.Q. Chen. Shock Temperatures and the Melting Point of Iron. In S.C. Schmidt, J.W. Forbes, and D.P. Dandekar, editors, *Shock Compression of Condensed Matter*, pages 133–136. AIP Press, Amherst, MA, USA, 1997.

[5] J.B. Aidun and Y.M. Gupta. Analysis of Lagrangian gauge measurements of simple and nonsimple plane waves. *J. Appl. Phys.*, 69(10):6998–7014, 1991.

[6] C.S. Alexander, J.R. Asay, and T.A. Haill. Magnetically applied pressure-shear: A new method for direct measurement of strength at high pressure. *J. Appl. Phys.*, 108(126101), 2010.

[7] L.V. Al'tshuler, S.B. Kormer, A.A. Bakanov, A.P. Petrunin, and A.A. Funtikov, A.I. Gubkin. Irregular conditions of oblique collision of shock waves in solid bodies. *Sov. Phys. JETP*, 14(986), 1962.

[8] J.R. Asay. The Sandia National Laboratories Shock Thermodynamics Applied Research (STAR) Facility. Technical Report SAND81-1901, 1981.

[9] T.D. Aslam and J.B. Bdzil. Numerical and theoretical investigations on detonation-inert confinement interactions, 2002.

[10] J.W. Banks, W.D. Henshaw, D.W. Schwendeman, and A.K. Kapila. A study of detonation propagation and diffraction with compliant confinement. *Combustion Theory and Modeling*, 12(4):769–808, 2008.

[11] L.M. Barker. Alpha-phase Hugoniot of iron. *J. Appl. Phys.*, 46(6):2544–2547, 1975.

[12] L.M. Barker and R.E. Hollenbach. Shock-wave studies of PMMA, Fused Silica, and Sapphire. *J. Appl. Phys.*, 41(10):4208–4225, 1970.

[13] L.M. Barker and R.E. Hollenbach. Laser inteferometer for measuring high velocities of any reflecting surface. *J. Appl. Phys.*, 43(11):4669–4675, 1972.

[14] L.M. Barker and R.E. Hollenbach. Shock wave study of the alpha-epsilon phase transition in iron. *J. Appl. Phys.*, 45(11):4872–4887, 1974.

[15] L.M. Barker and K.W. Schuler. Correction to the velocity-per-fringe relationship for the VISAR interferometer. *J. Appl. Phys.*, 45(8):3692–3693, 1974.

[16] G. Ben-Dor. *Shock Wave Reflection Phenomena*. Springer-Verlag, New York, 1992.

[17] D. Bernstein and D. D. Keough. Piezoresistivity of Manganin. *J. Appl. Phys.*, 35(5):1471–1474, 1964.

[18] G. Birkhoff and J.M. Walsh. Conical, axially symmetric flows. In *Jubile Scientifique: Memoires sur la Mecanique des Fluides*. 1954.

[19] W. Bleakney and A.H. Taub. Interaction of Shock Waves. *Rev. Mod. Phys.*, 21(4), 1949.

[20] D.D. Bloomquist and S.A. Sheffield. ORVIS, Optically Recording Velocity Interferometer System, Theory of Operation and Data Reduction Techniques. *Sandia Report, SAND82-2918*, 1982.

[21] G.M.B. Bouricius and S.F. Clifford. An optical interferometer using polarization coding to obtain quadrature phase components. *Rev. Sci. Intrum.*, 41(12):1800–1803, 1970.

[22] J.L. Brown, G. Ravichandran, W.D. Reinhart, and W.M. Trott. High pressure Hugoniot measurements using converging shocks. *J. Appl. Phys.*, 109(093520), 2011.

[23] J.M. Brown and R.G. McQueen. The equation of state for iron and the earth's core. In S. Akimoto and H. Manghnani, editors, *High Pressure Research in Geophysics*, volume 12, pages 611–623. Center for Academic Publications, Tokyo, 1982.

[24] J.M. Brown and R.G. McQueen. Phase Transition, Gruneisen Parameter, and Elasticity for Shocked Iron Between 77 GPa and 400 GPa. *Journal of Geophysical Research*, 91(B7):7485–7494, 1986.

[25] L.C. Chhabildas. Survey of Diagnostic Tools Used in Hypervelocity Impact Studies. *Int. J. Impact Eng.*, 5:205–220, 1987.

[26] L.C. Chhabildas and J.R. Asay. Dynamic yield strength and spall strength measurements under quasi-isentropic loading. In M.A. Meyers, L.E. Murr, and K.P Staudhammer, editors, *Shock Wave and High-Strain-Rate Phenomena in Materials*. Marcel Dekker Inc., N.Y., 1992.

[27] L.C. Chhabildas, J.E. Dunn, W.D. Reinhart, and J.M. Miller. An impact technique to accelerate flier plates to velocities over 12 km/s. *Int. J. Impact Engng.*, 14:121–132, 1993.

[28] L.C. Chhabildas and M.D. Knudsen. Techniques to Launch Projectile Plates to Very High Velocities. In L.C. Chhabildas, L. Davison, and Y. Horie, editors, *High-Pressure Shock Compression of Solids VIII*. Springer-Verlag, Berlin, 2005.

[29] L.C. Chhabildas, H.J. Sutherland, and J.R. Asay. A velocity interferometer technique to determine shear-wave particle velocity in shock-loaded solids. *J. Appl. Phys.*, 50(8), 1979.

[30] R.J. Clifton. Analysis of the Laser Interferometer. *J. Appl. Phys.*, 41(13):5335–5337, 1970.

[31] R.J. Clifton. Plastic Waves: Theory and Experiment. In S. Nemat-Nasser, editor, *Mechanics Today*, volume 1. Pergamon Press Inc., 1972.

[32] H.W. Coleman and W. G. Jr. Steele. *Experimentation and Uncertainty Analysis for Engineers*. John Wiley and Sons, Inc., 2 edition, 1999.

[33] R. Courant and K.O. Friedrichs. *Supersonic Flow and Shock Waves*. Springer-Verlag, New York, 1948.

[34] W.D. Crozier and W. Hume. High-velocity, light-gas gun. *J. Appl. Phys.*, 28(8):892–894, 1957.

[35] L. Davison. *Fundamentals of Shock Wave Propagation in Solids*. Shock Wave and High Pressure Phenomena. Springer-Verlag, Berlin, 2008.

[36] L. Davison and R.A. Graham. Shock Compression of Solids. *Physics Reports*, 55(4):255–379, 1979.

[37] D.H. Dolan. Foundations of VISAR analysis. *Sandia report, SAND2006-1950*, 2006.

[38] G.E. Duvall and G.R. Fowles. Shock Waves. In Bradley R.S., editor, *High Pressure Physics and Chemistry*, volume 2, pages 209–291. Academic Press, New York, 1963.

[39] G.E. Duvall and R.A. Graham. Phase transitions under shock-wave loading. *Rev. Mod. Phys.*, 49(3):523–579, 1977.

[40] K.J. Fleming and O.B. Crump. Portable, Solid State, Fiber Optic Coupled Doppler Interferometer System for Detonation and Shock Diagnostics. Technical report, 1994.

[41] G.R. Fowles and W.M. Isbell. Method for Hugoniot Equation-of-State Measurements at Extreme Pressures. *J. Appl. Phys.*, 36(4):1377–1379, 1964.

[42] R.A. Graham. *Solids Under High-Pressure Shock Compression.* Springer-Verlag, New York, 1993.

[43] R.A. Graham and J.R. Asay. Measurement of Wave Profiles in Shock Loaded Solids. *High Temperatures-High Pressures*, 10:355–390, 1978.

[44] C.A. Hall, J.R. Asay, M.D. Knudson, W.A. Stygar, R.B. Spielman, T.D. Pointon, D.B. Reisman, A. Toor, and R.C. Cauble. Experimental configuration for isentropic compression of solids using pulsed magnetic loading. *Rev. Sci. Instrum.*, 72(9), 2001.

[45] C.A. Hall, M.D. Knudsen, J.R. Asay, R. Lemke, and B. Oliver. High velocity flyer plate launch capability on the Sandia Z accelerator. *Int. J. Impact Engng.*, 26:275–287, 2000.

[46] D.B. Hayes, R.S. Hixson, and R.G. McQueen. High Pressure Elastic Properties, Solid-Liquid Phase Boundary and Liquid Equation of State from Release Wave Measurements in Shock-Loaded Copper. In M.D. Furnish, L.C. Chhabildas, and R.S. Hixson, editors, *Shock Waves in Condensed Matter*, page 483. Elsevier Science, New York, 1999.

[47] W.F. Hemsing. Velocity sensing interferometer (VISAR) modification. *Rev. Sci. Intrum.*, 50(1):73–78, 1979.

[48] E.S. Hertel, R.L. Bell, M.G. Elrick, A.V. Farnsworth, G.I. Kerley, J.M. Mcglaun, S.V. Petney, S.A. Silling, P.A. Taylor, and L. Yarrington. CTH: A Software Family for Multi-Dimensional Shock Physics Analysis. In R. Brun and L.D. Dumitresce, editors, *Proceedings of the 19th International Symposium on Shock Waves, VI*, pages 377–382, Marseille, France, 1993.

[49] R.L. Hilliard and G.G Shepherd. Wide-Angle Michelson Interferometer for Measuring Doppler Line Widths. *J. Opt. Soc. Amer.*, 56(3):362–369, 1966.

[50] H. Hornung. Regular and Mach Reflection of Shock Waves. *Ann. Rev. Fluid Mech.*, 18:33–58, 1986.

[51] H. Hornung. Deriving Features of Reacting Hypersonic Flow from Gradients at a Curved Shock. *AIAA*, 48(2):287, 2010.

[52] G.R. Johnson. Dynamic Analysis of a Torsion Test Specimen Including Heat-Conduction and Plastic Flow. *ASME J. Eng. Mat. and Tech.*, (103), 1981.

[53] O.E. Jones, F.W. Neilson, and W.B. Benedick. Dynamic Yield Behavior of Explosively Loaded Metals Determined by a Quartz Transducer Technique. *J. Appl. Phys.*, 33(11):3224–3232, 1962.

[54] G.I. Kerley. CTH Reference Manual: The Equation-of-State Package. Technical Report SAND91-0344, Sandia National Laboratories, 1991.

[55] G.I. Kerley. Multiphase Equation of State for Iron. Technical Report SAND93-0227, Sandia National Laboratories, 1993.

[56] K.S. Kim and R.J. Clifton. Pressure-Shear Impact of 6061-T6 Aluminum. *J. Appl. Mech.*, 47:11–16, 1980.

[57] M.D. Knudsen, D.L. Hanson, J.E. Bailey, C.A. Hall, and C. Deeney. Principal Hugoniot, reverberating wave, and mechanical reshock measurements of liquid deuterium to 400 GPa using plate impact techniques. *Phys. Rev. B.*, 69(144209), 2004.

[58] C.H. Konrad and R.L. Moody. Rear surface pin triggering technique. *Sandia report, SAND86-0791*, 1986.

[59] H.W. Liepmann and A. Roshko. *Elements of Gasdynamics*. Dover Publications, 1957.

[60] J. Lipkin and J.R. Asay. Reshock and release of shock-compressed 6061-T6 aluminum. *J. Appl. Phys.*, 48(1):182–189, 1976.

[61] E. Loomis and D. Swift. Oblique shock waves incident on an interface between two materials for general equations of state. *J. Appl. Phys.*, 103(023518), 2008.

[62] S.P. Marsh. *LASL Shock Hugoniot Data*. University of California Press, Ltd., 1980.

[63] R.G. McQueen, S.P. Marsh, J.W. Taylor, J.N. Fritz, and W.J. Carter. The Equation of State of Solids from Shock Wave Studies. In R. Kinslow, editor, *High Velocity Impact Phenomena*. Academic Press, Inc., 1970.

[64] R. Menikoff and B. Plohr. The Riemann problem for fluid flow of real materials. *Rev. Mod. Phys.*, 61(1):75–130, 1989.

[65] M. A. Meyers. *Dynamic Behavior of Materials*. John Wiley & Sons, Inc., 1994.

[66] A.C. Mitchell and W.J. Nellis. Shock compression of aluminum, copper, and tantalum. *J. Appl. Phys.*, 52(5), 1981.

[67] Y. Mori and K. Nagayama. Observation of shock wave convergence or collision induced by shaping of plane shock front in solids. *SPIE High-Speed Photography and Photonics*, 1801:357–361, 1992.

[68] F. Muller. Mach-Reflection of Detonation Waves in Condensed High Explosives. *Propellants and Explosives*, 3:115–118, 1978.

[69] W.J. Nellis, A.C. Mitchell, and D.A. Young. Equation-of-state measurements for aluminum, copper, and tantalum in the pressure range 80-440 GPa. *J. Appl. Phys.*, 93(1), 2003.

[70] J. Nguyen. New Routes to High Temperatures and Pressures. *Lawrence Livermore National Laboratory Science and Technology Review*, (March), 2007.

[71] D.L. Paisley, S. Luo, S.R. Greenfield, and A.C. Koskelo. Laser-launched flyer plate and confined laser ablation for shock wave loading: Validation and applications. *Rev. Sci. Instrum.*, 79(023902), 2008.

[72] M.H. Rice, R.G. McQueen, and J.M. Walsh. Compression of Solids by Strong Shock Waves. In F. Seitz and D. Turnbull, editors, *Solid State Physics*, volume 6. 1958.

[73] F. Seitz. *Modern Theory of Solids.* McGraw-Hill, New York, 1940.

[74] J.C. Slater. *Introduction to Chemical Physics.* McGraw-Hill, New York, 1939.

[75] D.J. Steinberg, S.G. Cochran, and M.W. Guinan. A constitutive model for metals applicable at high-strain rate. *J. Appl. Phys.*, 51, 1980.

[76] D.J. Steinburg and C.M. Lund. A Constitutive Model for Strain Rates from 10^{-4} to 10^{6} $\sec^{-1}$. *J. Appl. Phys.*, 65(1528), 1989.

[77] O.T. Strand, D.R. Goosman, C. Martinez, and T.L. Whitworth. Compact system for high-speed velocimetry using heterodyne techniques. *Rev. Sci. Intrum.*, 77, 2006.

[78] Y. Syono, T. Goto, and T. Sato. Pressure enhancement by conically convergent shocks in composite cylinders and its application to shock recovery experiments. *J. Appl. Phys.*, 53(11):7131–7135, 1982.

[79] P.A. Taylor. CTH Reference Manual: The Steinberg-Guinan-Lund Viscoplastic Model. Technical report, Sandia National Laboratories, 1992.

[80] W.M. Trott, J.M. Castaneda, J.J. O'Hare, M.R. Baer, L.C. Chhabildas, M.D. Knudsen, J.P. Davis, and J.R. Asay. Dispersive Velocity Measurements in Heterogenous Materials. Technical Report SAND2000-3082, 2000.

[81] T.J. Vogler and L.C. Chhabildas. Strength behavior of materials at high pressures. *Int. J. Impact Eng.*, 33:812–825, 2006.

[82] J. Von Neumann. Oblique reflection of shocks. Technical report, Explosives Research Report No. 12, U.S. Navy Department, 1943.

[83] Q. Williams and E. Knittle. The High-Pressure Melting Curve of Iron: A Technical Discussion. *Journal of Geophysical Research*, 96(B2):2171–2184, 1991.

[84] F.J. Zerilli and R.W. Armstrong. Dislocation-mechanics-based constitutive relations for material dynamics calculations. *J. Appl. Phys.*, 61, 1987.

[85] S. Zhuang. *Shock Wave Propagation in Periodically Layered Composites*. Ph.d. thesis, california institute of technology, 2002.

[86] J.A. Zukas, T. Nicholas, H.F. Swift, L.B. Greszczuk, and D.R. Curran. *Impact Dynamics*. John Wiley and Sons, New York, 1982.